QUANTIFICATION OF CEREBRAL BLOOD FLOW IN MOUSE MODELS OF HEMATOLOGICAL DISEASE

A Dissertation

Presented to the Faculty of the Graduate School

of Cornell University

In Partial Fulfillment of the Requirements for the Degree of

Doctor of Philosophy

by

Thom P. Santisakultarm

August 2012

QUANTIFICATION OF CEREBRAL BLOOD FLOW IN MOUSE MODELS OF HEMATOLOGICAL DISEASE

Thom P. Santisakultarm, Ph. D.

Cornell University 2012

The investigation of cerebral microcirculation is challenging due to the complex three-dimensional structure of the brain and the requirement to maintain subject physiology to ensure an adequate blood supply. We developed an algorithm to capture blood flow dynamics with high temporal and spatial resolution when coupled with two-photon excited fluorescence microscopy imaging. Using these techniques and chronic craniotomy surgical preparations, we focused our attention on myeloproliferative neoplasms and their impacts on cortical circulation. These rheological conditions exhibit an excessive amount of red blood cells, leukocytes, and/or platelets, resulting in abnormal, prothrombotic flow conditions. Although no direct evidence has indicated microvascular flow disruptions in the brain, cognitive dysfunction is reported among myeloproliferative neoplasm patients. Because neurological impairment is linked to cerebral microcirculation problems, we looked for direct confirmation in animal models of the diseases—essential thrombocythemia and polycythemia vera, specifically. We found cerebral microvessels in the subjects to be largely occluded by leukocytes and platelets, which adhered tightly to the endothelium. In the case of essential thrombocythemia, ~20% of the stalled vessels by

platelets remain blocked for over two hours, while the rest of the micro-occlusions resolved and reestablished flow on their own. The adherence of leukocytes and platelets is a result of cellular activation due to enhanced cell-to-cell interactions in the high hematocrit flow regime as well as the triggering of platelet aggregation by injured endothelial cells. We concluded that there is a need for targeted therapy to resolve cerebral microcirculation disruption, and that clinicians should include a careful cognitive evaluation when treating patients with myeloproliferative neoplasms. In future work, we are interested in identifying the mechanism of thrombosis in sickle cell disease where patients are severely anemic but prone to thrombosis, nevertheless.

Two-photon excited fluorescence microscopy also has many other applications. We exercised one by using second harmonic generation imaging to observe collagen fibers in cardiac tissue *in vitro*. In this study, collagen fibers were presented with cyclic anisotropic strain that led to tissue alignment and remodeling. We identified that anisotropy of biaxial strain causes fiber alignment along the principal directions of strain and concluded that strain field anisotropy is an independent regulator of fibroblast cell phenotype, turnover, and reorganization.

BIOGRAPHICAL SKETCH

Puifai was born and raised in Bangkok, Thailand, where she was safely sheltered away from gambling, smoking, and cursing by her dear parents. She wasted no time learning to love most of these activities, in addition to academically excelling in high school, when she arrived in Durango, CO, in 2001 while living with her host parents, Mike and Carol McGuire. She spent the following 2 years in Portland, OR, living with her aunt, Ladda Delaney, and finishing high school with the intention of going to college in the United States to become a neurosurgeon. Not long after she had started college at the Illinois Institute of Technology in Chicago, she began working in a research laboratory. In the lab, she quickly learned that medicine might not have been her true calling because research was definitely more fun. After graduating with a bachelor's of science in biomedical engineering, she came to Cornell University and began studying brain blood flow in myeloproliferative neoplasms and sickle-cell disease using two-photon excited fluorescence microscopy in Prof. Chris Schaffer's laboratory. The following five years have included an enormous amount of time spent learning not only how to become a good scientist, but also how to make the best out of every day, and how to enjoy what life has to offer.

To

Shawn Tan

and

Paula Petrica

ACKNOWLEDGMENTS

I am going to put my money on Claire Paduano, my undergraduate student, as the most influential person during my graduate school days at Cornell. While the definitive answer can only be confirmed many years from now, I am quite sure of it. Claire joined my research subgroup around my second or third year when I was still struggling with performing clean craniotomies and diagnosing what was wrong with the f**king laser. She made me very nervous with her quietness, as I had always surrounded myself with people who talked too much. I didn't know what to do when she didn't say anything. So I talked. I was also nervous because I had never taught anyone a subject as serious as two-photon excited fluorescent microscopy or hemodynamics in the cerebral microcirculation, let alone the fact that I was concurrently learning about these topics myself. Over the years, I saw Claire developed into an independent thinker, a researcher with her own initiative, and a patient and persevering scientist. She has made my role as a mentor immensely fulfilling. She is the reason that I am giving a post-doctoral researcher position at the National Institutes of Health a chance, even when I know I can get better pay doing something else. She is the reason I might give an academic career a shot.

Never before has anyone been able to convince me how short life can be and how to really, really live. Prof. Chris Schaffer has implanted his love of science in me. But most importantly, he made me realize that really cool, smart, and important people are just someone to aspire to: something to work toward, rather than to worship. He

gave me hope that I can be as serious about my professional career as I want, while being as human as I, indeed, am. Chris has taught me to try my best even when failure is inevitable, and along the way, to learn something, to feel good about my best effort, and to enjoy the moment.

To Matt Farrar, you will always be one of the few who believe in my gentle, kind hearted side. Thank you for believing in me, even when the world knows I am a loud, drunk, obnoxious, attention hogging, do-without-thinking, like-to-curse partier. It means a lot.

I think of Shawn Tan and Nate Rosidi as my perfect grad school companions for good times and bad times…respectively. Shawn never failed to amplify my laughter and expand the smile on my face, while Nate always made my whining and b*tching so much more entertaining than it would have been, despite the negative nature of the message. And for that, they both kept me at Cornell for much longer than I thought I would be. That is, until graduation.

For John Nguyen and Paula Petrica, when they graduated and moved away from Ithaca, I was depressed for months. I knew it was time for me to leave because the last two best friends who were very dear to me and would do anything for me had left Cornell. For the better. For all of us.

TABLE OF CONTENTS

LIST OF FIGURES

CHAPTER 2

CHAPTER 3

CHAPTER 4

CHAPTER 5

CHAPTER 6

CHAPTER 7

LIST OF TABLES

CHAPTER 2

CHAPTER 5

CHAPTER 6

LIST OF ABBREVIATIONS

2PEF	two-photon excited fluorescence
ABS	anisotropic biaxial strain
ACTA2	alpha-smooth muscle actin
AV	ascending venule
BMT	bone marrow tranplantation
BrdU	5-Bromo-2′-deoxyuridine
CD11b	cluster of differentiation molecule 11b
CML	chronic myeloid leukemia
ECM	extracellular matrix
ECG	electrocardiogram
Epo	erythropoietin
ET	essential thrombocythemia
FEA	finite element simulations
Hct	hematocrit
Hgb	hemoglobin
INF-a	interferon-alpha

JAK2	janus kinase 2
LED	light-emitting diode
Leu	leukocyte
MPN	myeloproliferative neoplasm
ND	neutral density
PA	penetrating arteriole
PAVIC	porcine aortic valve interstitial cell
PDMS	polydimethylsiloxane
Plt	platelets
PMF	primary myelofibrosis
PSGL-1	P-selectin glycoprotein ligand-1
PV	polycythemia vera
RBC	red blood cell
SHG	second harmonic generation
STAT	signal transducer and activator of transcription
Tdts	terminal deoxynucleotidyl transferase
TGFβ	transforming growth factor-beta
Tpo	thrombopoietin

VIC	valvular interstitial cell
WBC	white blood cell

CHAPTER 1

INTRODUCTION AND ORGANIZATION OF DISSERTATION

INTRODUCTION

Investigation of cerebral microcirculation presents many technical challenges to researchers. First, it requires *in vivo* observation where subjects can maintain a blood flow level comparable to that of physiological conditions of interest. In addition, the technique must have a reasonably high temporal and spatial resolution to determine dynamics and characteristics of the flow. Traditionally, microcirculatory systems of choice were limited to 2-dimensional systems, such as the mesenteric tissues and cremaster muscles, due to limited depth penetration of available imaging modalities. The brain, however, is a complex, 3-dimensional organ. With the introduction of two-photon excited fluorescence microscopy, we are able to observe blood flow in individual cortical microvessels from the surface of the brain to 1-mm beneath. Animals can be observed over hours, days, and weeks when coupled with chronic surgical preparations. The technique has immensely expanded the neurological disorders research field and enhanced the quality of the studies.

In this dissertation, we focus on hematological disorders, specifically myeloproliferative neoplasms, and their impact on cerebral microcirculation. Animal models of myeloproliferative neoplasms are recently available; therefore, prior studies were limited to clinical data. In addition, the brain was overlooked because myeloproliferative neoplasms are regarded as blood disorders, not brain disorders. However, one prominent feature of these disorders is thrombosis and circulation problems. Nevertheless, evidence suggests that patients with myeloproliferative neoplasms present neurological deficits. Because problems with microcirculation in

the brain such as small strokes are known to be associated with cognitive decline, dementia, and Alzheimer's disease, we suspect that alterations in blood rheology would result in abnormal circulation in microvascular networks that can lead to cognitive problems. Therefore, we examine cerebral blood flow in myeloproliferative neoplasms, while accounting for mechanisms that may be common aspects of bad blood flow that lead to neurological disorders.

ORGANIZATION OF DISSERTATION

The work described in this dissertation includes the development of *in vivo*, high spatio-temporal resolution imaging technique to study cerebral hemodynamics in normal and pathological states. The methods were utilized to examine the effects of myeloproliferative neoplasms and sickle cell disease—both hematological disorders—on cortical microcirculation. In addition, we made use of second harmonic generation using two-photon excited fluorescence microscopy to examine collagen rearrangement under cyclic strain. Each chapter can be read independently.

Chapter 2: This chapter introduces readers to non-linear optical imaging method, specifically two-photon excited fluorescence microscopy. It describes fluorescence generation, including second harmonic generation, and a brief overview of microscope setup. Two-photon excited fluorescence microscopy was compared to other microvascular flow measurement techniques, and its application to brain research was discussed.

Chapter 3: This chapter gives a background on myeloproliferative neoplasms. It describes the pathogenesis and genetics of the hematological conditions that alter blood compositions. The mechanisms and rheological impacts, especially thrombosis in microcirculatory systems, clinical outcomes, and current treatments were discussed. Myeloproliferative neoplasms effects on the brain were studied in details later in chapter 5.

Chapter 4: Subtle alterations in cerebral blood flow can impact the health and function of brain cells and are linked to cognitive decline and dementia. To understand hemodynamics in the three-dimensional vascular network of the cerebral cortex, we applied two-photon excited fluorescence microscopy to measure the motion of red blood cells in individual microvessels throughout the vascular hierarchy. We developed an algorithm to resolve cortical blood flow with high temporal and spatial resolution, and found flow pulsatility dependency on cardiac and respiration rhythms even in smallest capillaries and venules

Chapter 5: Myeloproliferative neoplasms are a group of hematological diseases where the bone marrow is overactive, resulting in excess red blood cells, white blood cells, and platelets. These additional cellular components of the blood lead to high viscosity, endothelial activation, and prothrombotic environment. To date, direct visualization of cerebral microcirculatory problem in vivo has not been done because of the lack of animal model and advanced imaging technique. We used two-photon excited fluorescence microscopy to investigate microvascular network and found

occlusions of individual capillaries of MPN mice. These blood flow disruptions are associated with leukocyte and platelet plugs and were negligibly affected by the standard aspirin treatment.

Chapter 6: Sickle cell disease is a genetic disorder where red blood cells become abnormal, rigid, sickle shape upon deoxygenation. Sickling leads to various complications including increased vascular resistance, occlusions of blood vessels, and red blood cell breakage resulting in anemia. In this chapter, we observed transition of red blood cell physiology and flow characteristics in cerebral microvessels of mouse models of sickle cell disease under a variety of oxygen levels.

Chapter 7: Connective tissues in heart valve leaflets have evolved to perform critical biomechanical functions under cyclic loading. These tissues are composed of collagenous fibers, oriented to optimize anisotropic mechanical properties appropriate to their local environment. The organized structure is created and modified by resident fibroblasts in response to mechanical forces in their environment, but the effect of strain direction on matrix remodeling is unclear. In this chapter, we designed a bioreactor system capable of generating and maintaining anisotropic strain on fibroblast in three-dimensional hydrogel. The collagen realignment in response to the stimulus force was verified using second harmonic imaging microscopy.

Chapter 8: This chapter summarizes important findings from previous chapters. It also discusses impacts in the clinical setting and future directions of cerebral microcirculatory research in hematological disorders.

CHAPTER 2

ESSENTIAL THROMBOCYTHEMIA AND POLYCYTHEMIA VERA

Myeloproliferative neoplasms (MPNs) are rheological disorders that result from hyperactivity of the bone marrow, leading to an increase in various cellular components of the blood. There are four types of MPN disorders; polycythemia vera (PV), essential thrombocythemia (ET), primary myelofibrosis (PMF), and chronic myelogenous leukemia (CML) (*1*). An acquired mutation (JAK2) in hematopoietic stem cells is common in the MPNs, and leads to abnormal proliferation of various blood cells. In PV, red blood cells (RBCs), white blood cells (leukocytes), and platelets production is enhanced, leading to excess in the cellular components of the blood. Platelet and leukocyte counts are elevated in ET and CML, respectively. Lastly, PMF usually presents with complete blood counts similar to those of PV or CML, but progresses to thrombocytopenia and anemia over time. All the MPNs are characterized by blood flow and/or coagulation problems, which occur in diminishing order of severity and frequency in PV, ET, PMF, and (rarely) CML. Phlebotomy, cytoreductive therapy, low-dose aspirin, and JAK2 inhibitors are often employed to correct blood counts, reduce hypercoaguability, and restore normal blood flow.

Thrombotic events are common in PV and ET. In fact, stroke, cardiovascular diseases, and deep-vein thrombosis are the main causes of morbidity and mortality in these conditions. Alterations in the blood result in abnormal rheology, including increased whole blood viscosity and resistance, disproportional expansion of cell mass in vascular lumen, and enhanced interactions between platelets, leukocytes, RBCs, and endothelium. Although disturbance in small vascular networks is suspected, no direct studies have focused on microcirculatory systems due to the lack of animal models of

MPNs and advanced tools to visualize blood flow *in vivo*. Meanwhile, evidence of neurological complications in patients with ET and PV indicates a need to understand the impacts of these diseases on cerebral hemodynamics. Therefore, this chapter reviews ET and PV and serves as a basis for our study in Chapter 5 of the impacts of MPNs on cortical blood flow.

JAK2^{V617F} MUTATION AND MYELOPROLIFERATIVE NEOPLASMS

JAK2 is a cytoplasmic tyrosine kinase in the signal transducer and activators of transcription (STAT) signaling pathway in hematopoietic stem cells. The acquired somatic point mutation at codon 617 of the JAK2 gene leads to a valine-to-phenylalanine mutation in this kinase. Although found in patients with all MPNs, JAK2^{V617F} mutation is most common in ET (60% of the cases) and PV (95% of the cases) (*2*). Normally, STAT molecules are phosphorylated by activated JAK2, then translocate to the nucleus, promoting production of blood cells including RBCs, leukocytes, and platelets. The V617F mutation in JAK2 leads to constitutive phosphorylation activity and the recruitment of STAT molecules, leading to unregulated production of blood cells (**Fig. 2.1**) (*3, 4*).

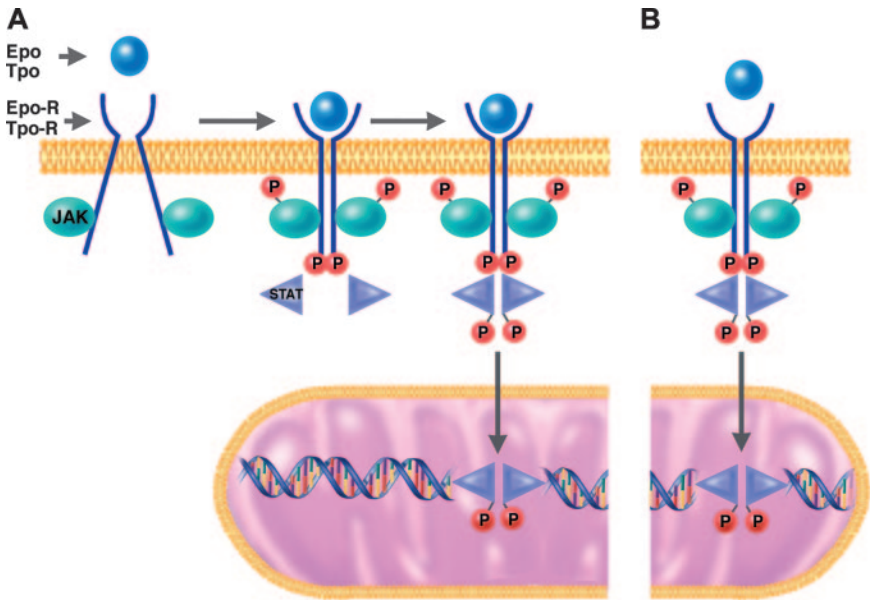

Figure 2.1: JAK/STAT signal transduction pathway in responses to hematopoietic growth factors

Under normal conditions (A), erythroid and megakaryocytic progenitors require binding of erythropoietin (Epo) or thrombopoietin (Tpo) to their respective receptors (Epo-R or Tpo-R) to initiate the intracellular sequence of phosphorylation and activation events, leading to transcriptional activation of growth factor-responsive target genes. In hematopoietic progenitor cells of patients with MPNs who have the $JAK2^{V617F}$ mutation (B), this JAK/STAT signal transduction pathway is constitutively activated in the absence of binding of erythropoietin or thrombopoietin to their respective receptors (*5*).

Additional research is required to answer how a common JAK2 mutation can lead to a variety of MPN phenotypes. In mice, retroviral delivery of mutant $JAK2^{V617F}$ resulted in development of both ET and PV phenotypes. A higher level of mutant JAK2 gene leads to elevated RBC, leukocyte, and platelet counts, whereas a lower level of the gene leads to elevated platelet counts similar to ET (*6*). Likewise, while the $JAK2^{V617F}$ mutation is generally more frequent in human cases of PV, only 60% of ET cases possess the $JAK2^{V617F}$ mutation. Therefore, several hypotheses have been developed to address the variation in phenotypes associated with the mutant JAK2 gene. One theory is gene dosage: 25% of patients with PV carry 2 copies of $JAK2^{V617F}$, compared to mostly heterozygous or wildtype ET patients. Observations in mouse models of MPN are highly consistent with the gene dosage theory. Alternatively, it is possible that additional mutations may be involved in the pathogenesis of these diseases. In this theory, hematopoietic stem cells of myeloid lineage acquire $JAK2^{V617F}$. Since virtually all PV cases carry this mutation, $JAK2^{V617F}$ alone may lead to disease progression. Perhaps, in order for ET or PMF to develop, a secondary mutation must occur in addition to the $JAK2^{V617F}$. This hypothesis seems reasonable, as hematopoietic malignancies often bear more than one mutated gene. Finally, receptor expression may influence the level of $JAK2^{V617F}$ activation. Many receptors, including erythropoietin and thrombopoietin receptors, are expressed during myeloid and erythroid differentiation. The interaction between these receptors and $JAK2^{V617F}$ may influence the expression of the activated phenotype (**Fig. 2.2**) (*7*).

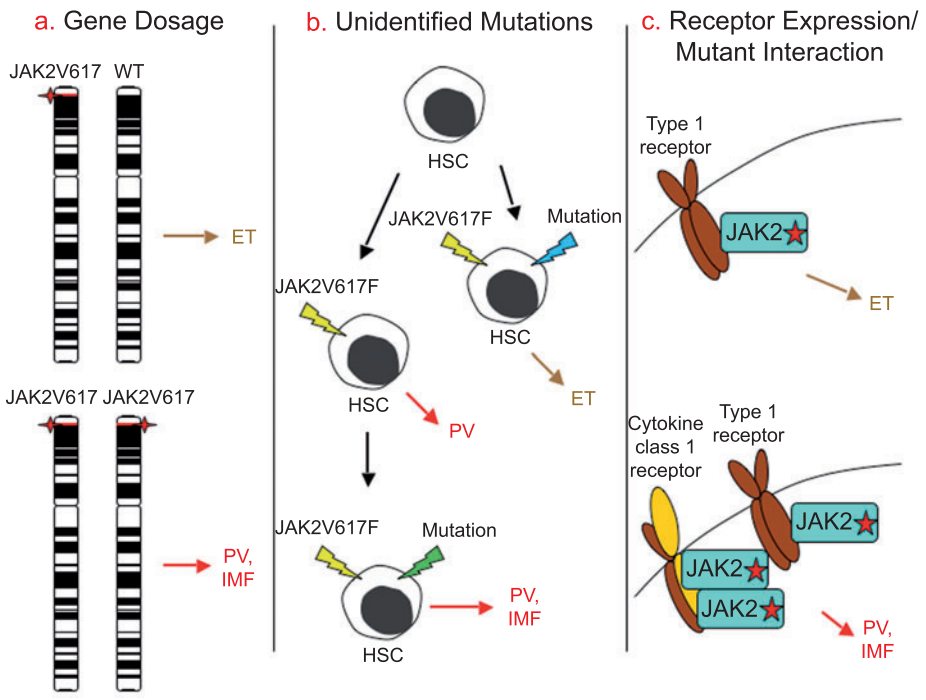

Figure 2.2: Possible causes of phenotype variability exhibited by JAK2^{V617F}
(a) Gene dosage. Heterozygous contribution of JAK2^{V617F} may lead to essential thrombocythemia. Homozygous contribution and a lack of wild-type JAK2 may lead to more severe phenotypes, such as PV and PMF. (b) Unidentified mutations. JAK2^{V617F} or other mutations can lead to essential thrombocythemia. However, JAK2^{V617F} is required for phenotypes such as PV, with secondary mutations needed for the progression to PMF. (c) Specific receptors are expressed on the surface of myeloid cells. The type of receptor may result in higher levels of JAK2^{V617F} activation that influence the phenotype of disease (*8*).

CLINICAL COMPLICATIONS IN ET AND PV

Hemorrhagic and thrombotic complications are the major causes of morbidity and mortality in ET and PV. In general, the use of antiplatelet drugs (e.g. aspirin) in MPNs increases the risk of bleeding. But, counterintuitively, the risk of bleeding is also heightened in cases of extreme thrombocytosis, especially in patients with ET (*9, 10*). The vast number of platelets may sequester von Willebran factors in the blood stream and prevent them from aiding normal adhesion of platelets to wound sites, resulting in abnormal bleeding (*11*).

Coagulation and circulation problems in ET and PV are abundant, leading to a number of secondary clinical conditions with a wide range of severity. Some of the more minor manifestations include fatigue, shortness of breath, dizziness, headache, and pluritus; other major ones are deep vein thrombosis of the lower extremities (*9, 12*), pulmonary embolism, erythromelalgia (*13*), edema, heart attack (*14*), and stroke(*15*). During and after surgical procedures, even when coupled with heparin treatment, arterial and venous thrombotic events frequently develop in MPN patients (*16*)**.** These symptoms are rooted in thrombotic complications due to the abnormal rheology associated with excess RBCs, leukocytes, and/or platelets.

In PV, high hematocrit is the most influential factor governing occurrences of thrombotic events (*17*). The physical consequences of red-cell mass expansion include increased strain on the vessel wall due to hyperviscosity, increased shear stress experienced by blood cells, and vasoconstriction due to nitric oxide scavenging by

RBCs (*18*). The elevated shear stress on the vessel wall leads to endothelial damage and activation in addition to platelets and leukocytes activation, enhancing cell-cell and cell-endothelium interactions (*9, 19*). This environment is highly prothrombotic and is commonly observed in cases of PV with high hematocrit (*17*). Since viscosity increases exponentially as hematocrit increases, it is important to tightly control hematocrit level (**Fig. 2.3**) (*18*). The use of phlebotomy to reduce hematocrit has been shown to restore blood flow in PV patients (*20*). Unfortunately, reduction in RBC mass is only part of the answer. Even among PV patients with same hematocrit level, viscosity varies widely (*21*). In addition, the pathological effects of elevated hematocrit may relate to reduced endothelial surface layer thickness and the consequent alteration in the blood–endothelium interface that further increases flow resistance (*22*). The roles of leukocytes and platelets in abnormal coagulation have also been examined. PV patients with high leukocyte count (above 15 x 10^9/L) had an increased risk for thrombotic events, mainly derived from an increased risk of myocardial infarction (*23*) Platelets did not play a statistically significant role in influencing thrombotic risk, however (*24*) The reason for this is unknown at the present.

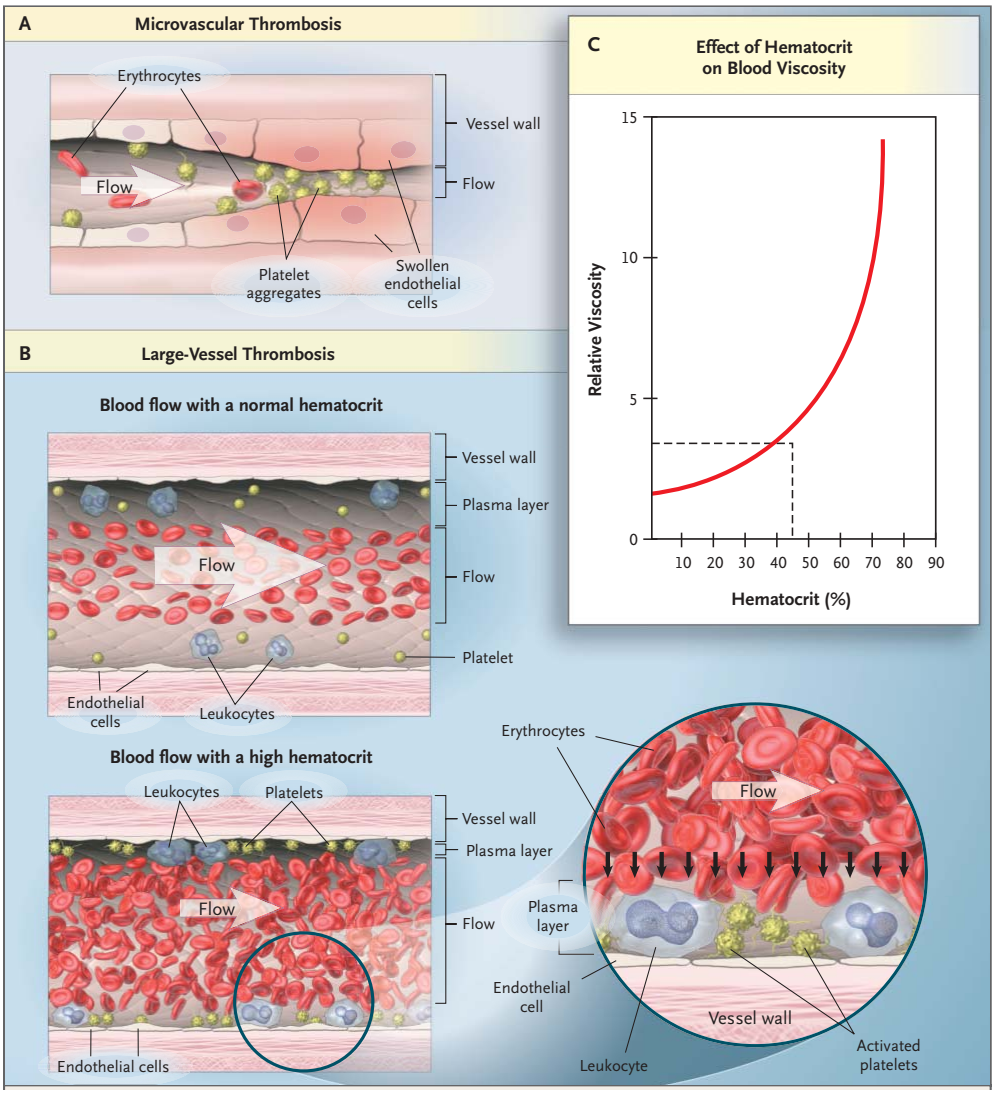

Figure 2.3: Mechanisms of Thrombosis in Polycythemia Vera
Microvascular thrombosis (A) involves the interaction of activated platelets and endothelial cells, which is facilitated by the high shear rate, especially in arterioles. Macrovascular thrombosis (B) takes place in larger vessels where the effects of an elevated red-cell mass on blood flow are most pronounced. With the expansion of red-cell mass, laminar flow is disturbed, vessel-wall strain is increased, and the interactions of platelets and leukocytes with the endothelium, RBCs, and each other are enhanced. Thus, even in a situation in which blood viscosity leads to low shear rates, platelet adhesion and aggregation are facilitated, and thrombin generation is initiated. (C) The relation between the blood viscosity and the hematocrit. The relation between thrombosis and the hematocrit in PV follows a similar curve, underscoring the fact that the expansion of the red-cell mass, rather than abnormal platelets or leukocytes, that dominates the mechanism of coagulopathy associated with this disorder (*18*)

On the other hand, the story of thrombosis in ET is rather confounding. Naturally, platelet and leukocyte counts have been the main target of plentiful studies. Leukocytosis increases thrombotic events and is an independent predictor of leukemic transformation in ET (*25, 26*) The role of platelets, however, was not shown to increase thrombotic risk in ET consistently, except at extremely high levels (above 1500 x 10^9/L) (*9, 10*). Since platelet cytoreduction therapy reduces thrombotic event in high-risk patients, the present school of thought is that thrombocytosis indirectly contributes to the hemostatic complications of ET.

The prothrombotic flow regime in ET and PV is detrimental to adequate microcircular transport of nutrition, waste, and oxygen, which are crucial to maintaining neural health. Low levels of erythropoietin common among PV patients may also contribute to a worsened infarct outcome due to the lack of its neuroprotective properties (*27*). Neurological complications of ET and PV include depression (*28, 29*), mixed movement disorder (*29*), amnesia, headache, and dysphagia (*30*). Stroke and cerebral embolism are also prevalent in both ET (*31*) and PV (*32*), observations which are also consistent with our own, as later described in Chapter 5.

CELLULAR ACTIVATION AND INTERACTIONS

Thrombosis is a result of the complex interplay between activated platelets, leukocytes, and vascular endothelial cells. In MPNs, first, platelets adhere to the damaged endothelium. The adhesion event triggers the activation of these platelets and

the release of activating factors stored in their granules, including membrane ligands and chemokines, which recruit leukocytes as well as additional platelets to the vessel wall. The adherence of leukocytes to the vessel wall is mediated by adherent platelets via P-selectin (*33*) P-selectin, a cell-adhesion molecule, is expressed by activated platelets and primarily mediates initial interactions between platelets and leukocytes via P-selectin glycoprotein ligand-1 (PSGL-1), which is constitutively expressed on leukocyte surfaces (*34*).

Overactivation of leukocytes and platelets in PV and ET has been observed both *in vivo* and *in vitro* (*13*). The leukocytes in ET and PV overexpress CD11b, an antigen mediating adhesion during inflammation. These leukocytes thus have a greater capacity for phagocytosis as well as increased production of reactive oxygen species (*35*). Further, in ET patients with thrombotic events, the expression of CD11b in monocytes and the percentage of platelets expressing P-selectin is increased in comparison to ET patients without thrombotic events. Similarly, CD11b expression is significantly increased in neutrophils when comparing PV patients with and without thrombosis. This suggests that leukocyte activation in MPNs plays an essential role in thrombogenesis. ET patients are also more likely to show increases in E-selectin and circulating microparticles, both of which amplify thrombogenesis (*36, 37*). Further, prothrombin fragment, thrombomodulin, and von Willebrand factor were found to be elevated in both PV and ET. Platelet and leukocyte activation results in an increased percentage of circulating platelet-leukocyte complexes, which is reported to correlate with neutrophil degranulation, stabilization of fibrinogen, and higher extracellular

tissue factor content (*38, 39*). Hence, prothrombotic flow environment is constituted (*37, 40, 41*). And indeed, high leukocyte count correlates to high thrombotic incidence in ET patients (*25, 42*). Our observations of both leukocyte and platelet adhesion to microvasculature and obstruction of blood flow, as described in Chapter 5, is also in agreement with clinical findings.

The $JAK2^{V617F}$ mutation seems to play its prothrombotic role by encouraging P-selectin overexpression. P-selectin was found to be higher in ET patients with the mutation compared to patients with wild-type allele (*38*). Interestingly, the dosage effect of $JAK2^{V617F}$ allelic burden on levels of coagulation players including soluble P-selectin, soluble CD40 ligand, von Willebrand factor, and circulating platelet-leukocyte complexes was observed in $JAK2^{V617F}$ positive ET patients. $JAK2^{V617F}$ also promotes leukocyte overactivation, and therefore also correlates with increased adhesion, endothelial damage, and high coagulation incidence in ET (*25*).

In our study, we found blood brain barrier leakage into the parenchymal tissue, likely due to vascular damage. This is consistent with the severe endothelial damage that has been seen using electron microscopy (*43*). Increased circulating endothelial cells indicating endothelial activation has also been previously detected (*36*). The endothelial dysfunction and enhanced cellular adhesion results in chronic obstructions of the cerebral microcirculation.

The consequence of high thrombotic incidence in the brain is our particular interest. Hyperviscosity, endothelial injury due to leukocyte activation, thrombus formation, and hyperactivated JAK2 are all features characteristic of ET and PV that may contribute, along with other risk factors, to the development and progression of atherothrombosis (*14*). Endothelial dysfunction has been identified to be involved in the pathogenesis of lacunar stroke, especially in those patients with concomitant silent lacunar infarcts and ischemic white matter lesions (*15, 44*). Several studies have also linked inflammatory factors—soluble P-selectin, surface P-selectin expression, and platelet-leukocyte aggregates in blood—to patients with arterial thrombosis, including cerebrovascular events (*45*). Therefore, we focused our study in the brain of MPN mouse models. And we have found direct evidence of small stroke in capillary beds. For this reason, clinical treatments should pay careful attention on cognitive health and function of MPN patients.

MANAGEMENT OF ET AND PV

Current therapy for ET and PV is not curative. The objective is to prevent thrombotic and hemorrhagic events and to minimize splenomegaly. Phlebotomy, targeting a normal physiological hematocrit of ~45%, is the dominant method for correcting excessive RBCs in PV (*46*). Aspirin is also used in both ET and PV to reduce platelet adherence except in cases where the patient is at risk for hemorrhage (*4*). Available cytoreductive therapy includes hydroxyurea, busulfan, anagrelide, and interferon-alpha (INF-α) (**Table 2.1**), the last of which also acts as a myelosuppresant (*4*). Hydroxyurea is the most commonly prescribed as it provides the best

hematological outcome with the least adverse effects. When compared to other available cytoreductive therapies, hydroxyurea is associated with significantly lower risk of arterial thrombosis, major hemorrhage, and myelofibrosis transformation. Its dose is titrated to keep platelets lower than 400 x 10^9 /L and leukocytes higher than 2 x 10^9 /L. For patients who are intolerant or resistant to hydroxyurea, INF-α or busulfan are employed. However, both drugs are less widely used, since their side effects are generally more severe compared to hydroxyurea and their long-term effects are still unknown. Lastly, anagrelide is superior to hydroxyurea in preventing venous thrombosis. There is a notion among physicians that hydroxyurea and anagrelide are leukemogenic. However, hydroxyurea is an effective long-term treatment for sickle-cell disease and does cause leukemia in those patients (*47*). Therefore, this claim is not substantiated.

Risk Groups PV and ET	Management ET	Management PV
Low risk (age < 60 years and no thrombosis history)	Low-dose aspirin	Low-dose aspirin + phlebotomy*
Low risk with extreme thrombocytosis§	Low-dose aspirin‖	Low-dose aspirin‖ + phlebotomy
High risk (age ≥ 60 years or thrombosis history)	Low-dose aspirin + hydroxyurea¶	Low-dose aspirin + phlebotomy + hydroxyurea¶

Table 2.1. Risk Stratification and Risk-adapted Therapy in ET and PV

*In the presence of aspirin therapy, the hematocrit target can range between 38% and 50% and is set at a level that maintain best performance status.

§Extreme thrombocytosis is defined as a platelet count of >1,000 x 10^9/L

‖Clinically significant acquired von Willibrand syndrome should be excluded before the use of aspirin in patients with extreme thrombocytosis

¶In hydroxyurea-intolerant or -resistant patients, INF-α (age <60 years) or busulfan (age >60 years) might be used (*4*)

Because PV is associated with higher thrombotic risk than ET, the possibility that patients who have $JAK2^{V617F}$ may exhibit more severe disease outcome than those who did not was examined. In PV, higher $JAK2^{V617F}$ allele burden is correlated with more advanced myelofibrosis, greater splenomegaly, and higher white blood cell count (*48*). As compared to those with less than 25% mutant allele, patients harboring greater than 75% $JAK2^{V617F}$ allele were at higher relative risk of presenting larger spleen or suffering from pruritus. In these patients, the risk of requiring chemotherapy or developing major cardiovascular events was significantly increased (*49*). In addition, the presence of $JAK2^{V617F}$ in ET cases is associated with more thrombotic complications (*12, 50*). The presence of $JAK2^{V617F}$ may modify thrombotic risk by upregulating P-selectin, thus activating leukocytes and platelets, as well as producing dysfunctional RBCs with enhanced adhesiveness (*19*) Therefore, cytoreductive therapy with myelosuppresant quality may positively affect disease progression and severity. Several JAK2 inhibitors, such as TG101348 and INCB018424, that reduce $JAK2^{V617F}$ allele burden are also being investigated (*46*).

REFERENCE

1. M. Wadleigh, A. Tefferi, Classification and diagnosis of myeloproliferative neoplasms according to the 2008 World Health Organization criteria. *Int J Hematol* **91**, 174 (Mar 27, 2010).
2. G. Wernig *et al.*, Expression of Jak2V617F causes a polycythemia vera-like disease with associated myelofibrosis in a murine bone marrow transplant model. **107**, 4274 (Jun 1, 2006).
3. K. Morgan, D. Gilliland, A Role for JAK2 Mutations in Myeloproliferative Diseases. *Annu Rev Med*, (Oct 5, 2007).
4. A. Tefferi, W. Vainchenker, Myeloproliferative neoplasms: molecular pathophysiology, essential clinical understanding, and treatment strategies. *J Clin Oncol* **29**, 573 (Feb 10, 2011).
5. A. Schafer, Molecular basis of the diagnosis and treatment of polycythemia vera and essential thrombocythemia. *Blood* **107**, 4214 (Jun 1, 2006).
6. R. Tiedt *et al.*, Ratio of mutant JAK2-V617F to wild-type Jak2 determines the MPD phenotypes in transgenic mice. *Blood* **111**, 3931 (Apr 15, 2008).
7. M. Funakoshi-Tago, S. Pelletier, T. Matsuda, E. Parganas, J. N. Ihle, Receptor specific downregulation of cytokine signaling by autophosphorylation in the FERM domain of Jak2. *EMBO J* **25**, 4763 (Oct 18, 2006).
8. K. J. Morgan, D. G. Gilliland, A role for JAK2 mutations in myeloproliferative diseases. *Annu Rev Med* **59**, 213 (Jan 1, 2008).

9. A. Carobbio *et al.*, Risk factors for arterial and venous thrombosis in WHO-defined essential thrombocythemia: an international study of 891 patients. *Blood* **117**, 5857 (Jun 2, 2011).

10. A. Tefferi, Platelet count in essential thrombocythemia: the more the better? *Blood* **112**, 3526 (Oct 15, 2008).

11. U. Budde, P. J. van Genderen, Acquired von Willebrand disease in patients with high platelet counts. *Semin Thromb Hemost* **23**, 425 (Jan 1, 1997).

12. H. Reikvam, R. V. Tiu, Venous thromboembolism in patients with essential thrombocythemia and polycythemia vera. *Leukemia* **26**, 563 (Apr 1, 2012).

13. M. Karakantza *et al.*, Markers of endothelial and in vivo platelet activation in patients with essential thrombocythemia and polycythemia vera. *Int J Hematol* **79**, 253 (Apr 1, 2004).

14. A. Cucuianu *et al.*, Arterial stenosis and atherothrombotic events in polycythemia vera and essential thrombocythemia. *Rom J Intern Med* **44**, 397 (Jan 1, 2006).

15. I. L. H. Knottnerus, H. Ten Cate, J. Lodder, F. Kessels, R. J. van Oostenbrugge, Endothelial dysfunction in lacunar stroke: a systematic review. *Cerebrovasc Dis* **27**, 519 (Jan 1, 2009).

16. M. Ruggeri *et al.*, Postsurgery outcomes in patients with polycythemia vera and essential thrombocythemia: a retrospective survey. *Blood* **111**, 666 (Jan 15, 2008).

17. H. Kwaan, J. Wang, Hyperviscosity in polycythemia vera and other red cell abnormalities. *Semin Thromb Hemost* **29**, 451 (Oct 1, 2003).

18. J. Spivak, Daily aspirin--only half the answer. *N Engl J Med* **350**, 99 (Jan 8, 2004).

19. S. Austin, J. Lambert, The JAK2 V617F mutation and thrombosis. *Br J Haematol* **143**, 307 (Nov 1, 2008).

20. D. Thomas *et al.*, Cerebral blood-flow in polycythaemia. *Lancet* **2**, 161 (Jul 23, 1977).

21. T. C. Pearson, C. P. Ring, G. Wetherley-Mein, Plasma and whole blood viscosity in treated primary polycythaemia. *Clin Lab Haematol* **2**, 73 (Jan 1, 1980).

22. V. Richter *et al.*, Excessive erythrocytosis compromises the blood-endothelium interface in erythropoietin-overexpressing mice. *The Journal of Physiology* **589**, 5181 (Nov 1, 2011).

23. R. Landolfi *et al.*, Leukocytosis as a major thrombotic risk factor in patients with polycythemia vera. *Blood* **109**, 2446 (Mar 15, 2007).

24. M. Di Nisio *et al.*, The haematocrit and platelet target in polycythemia vera. *Br J Haematol* **136**, 249 (Jan 1, 2007).

25. T. Barbui, A. Carobbio, A. Rambaldi, G. Finazzi, Perspectives on thrombosis in essential thrombocythemia and polycythemia vera: is leukocytosis a causative factor? *Blood*, 1 (Apr 16, 2009).

26. N. Gangat *et al.*, Leucocytosis in polycythaemia vera predicts both inferior survival and leukaemic transformation. *Br J Haematol* **138**, 354 (Aug 1, 2007).

27. M. Buemi *et al.*, The pleiotropic effects of erythropoietin in the central nervous system. *J Neuropathol Exp Neurol* **62**, 228 (Feb 28, 2003).

28. C. Fones, W. F. Tsoi, Polycythaemia rubra vera presenting with depression: recognising the syndrome abulia. *Br J Clin Pract* **49**, 97 (Jan 1, 1995).

29. M. Bauer, Absolutely therapy-resistant depression and mixed movement disorder in an unusual case of polycythemia vera. *Pharmacopsychiatry* **28**, 66 (Mar 1, 1995).

30. J. Kondlapudi, R. J. O'Connor, S. Mawer, Cerebral haemorrhage as the presenting feature of myeloproliferative disorder. *BMJ Case Rep* **2009**, (Jan 1, 2009).

31. S. Richard, J. Perrin, P.-A. Baillot, J.-C. Lacour, X. Ducrocq, Ischaemic stroke and essential thrombocythemia: a series of 14 cases. *Eur J Neurol* **18**, 995 (Jul 1, 2011).

32. T. Segura, J. Serena, J. Teruel, A. Davalos, Cerebral embolism in a patient with polycythemia rubra vera. *Eur J Neurol* **7**, 87 (Jan 1, 2000).

33. F. Cervantes, E. Arellano-Rodrigo, A. Alvarez-Larrán, Blood cell activation in myeloproliferative neoplasms. *Haematologica* **94**, 1484 (Nov 1, 2009).

34. T. Villmow, B. Kemkes-Matthes, A. Matzdorff, Markers of platelet activation and platelet-leukocyte interaction in patients with myeloproliferative syndromes. *Thromb Res* **108**, 139 (Nov 1, 2002).

35. C. Burgaleta, N. González, J. César, Increased CD11/CD18 expression and altered metabolic activity on polymorphonuclear leukocytes from patients with polycythemia vera and essential thrombocythemia. *Acta Haematol* **108**, 23 (Jan 1, 2002).

36. A. Belotti *et al.*, Circulating endothelial cells and endothelial activation in essential thrombocythemia: results from CD146+ immunomagnetic enrichment--flow cytometry and soluble E-selectin detection. *Am J Hematol* **87**, 319 (Mar 1, 2012).

37. J. Duchemin *et al.*, Increased circulating procoagulant activity and thrombin generation in patients with myeloproliferative neoplasms. *Thromb Res* **126**, 238 (Sep 1, 2010).

38. E. Arellano-Rodrigo *et al.*, Increased platelet and leukocyte activation as contributing mechanisms for thrombosis in essential thrombocythemia and correlation with the JAK2 mutational status. *Haematologica* **91**, 169 (Feb 1, 2006).

39. A. Falanga, M. Marchetti, T. Barbui, C. W. Smith, Pathogenesis of thrombosis in essential thrombocythemia and polycythemia vera: the role of neutrophils. *Semin Hematol* **42**, 239 (Oct 1, 2005).

40. A. Falanga *et al.*, Polymorphonuclear leukocyte activation and hemostasis in patients with essential thrombocythemia and polycythemia vera. *Blood* **96**, 4261 (Dec 15, 2000).

41. E. Shantsila, P. W. Kamphuisen, G. Y. H. Lip, Circulating microparticles in cardiovascular disease: implications for atherogenesis and atherothrombosis. *J Thromb Haemost* **8**, 2358 (Nov 1, 2010).

42. A. Carobbio *et al.*, Leukocytosis and risk stratification assessment in essential thrombocythemia. *J Clin Oncol* **26**, 2732 (Jun 1, 2008).

43. T. Saigusa *et al.*, A case of essential thrombocytosis developing nephrotic syndrome and severe endothelial damage. *J Nephrol* **19**, 656 (Jan 1, 2006).

44. A. Hassan *et al.*, Markers of endothelial dysfunction in lacunar infarction and ischaemic leukoaraiosis. *Brain* **126**, 424 (Feb 1, 2003).

45. Z. G. Franks, R. A. Campbell, A. S. Weyrich, M. T. Rondina, Platelet-leukocyte interactions link inflammatory and thromboembolic events in ischemic stroke. *Annals of the New York Academy of Sciences* **1207**, 11 (Oct 7, 2010).

46. G. Finazzi, T. Barbui, The treatment of polycythaemia vera: an update in the JAK2 era. *Intern Emerg Med* **2**, 13 (Mar 1, 2007).

47. E. Voskaridou *et al.*, The effect of prolonged administration of hydroxyurea on morbidity and mortality in adult patients with sickle cell syndromes: results of a 17-year, single-center trial (LaSHS). *Blood* **115**, 2354 (Mar 25, 2010).

48. R. T. Silver *et al.*, JAK2(V617F) allele burden in polycythemia vera correlates with grade of myelofibrosis, but is not substantially affected by therapy. *Leukemia research*, (Jul 22, 2010).

49. A. Vannucchi *et al.*, Prospective identification of high-risk polycythemia vera patients based on JAK2(V617F) allele burden. *Leukemia* **21**, 1952 (Sep 1, 2007).

50. H. S. Lee *et al.*, Incidence rates and risk factors for vascular events in patients with essential thrombocythemia: a multicenter study from Korea. *Clin Lymphoma Myeloma Leuk* **12**, 70 (Feb 1, 2012).

CHAPTER 3

TWO-PHOTON EXCITED FLUORESCENCE MICROSCOPY

Recent advances in non-linear optical imaging methods such as two-photon excited fluorescence microscopy (2PEF) have enabled immense progress to be made in studies of biological systems as complex as the brain (*1*). 2PEF has enabled studies that visualize subcellular structures and functions, and observe dynamics of specific cells *in vivo* (*1, 2*). 2PEF provides a means to observe subcellular structures smaller than 1 μm and as deep as 1 mm inside the brain without causing damage to the surrounding tissue (*3, 4*) (**Fig. 3.1**). When combined with chronic surgical preparations, structures of interest can be monitored over months. In this chapter, we provide a framework of 2PEF by briefly reviewing fluorescence optical imaging, two-photon excitation and second harmonic generation processes, and describing the 2PEF microscope setup. The imaging techniques described in this dissertation were utilized in all of our studies presented in Chapters 4 - 7.

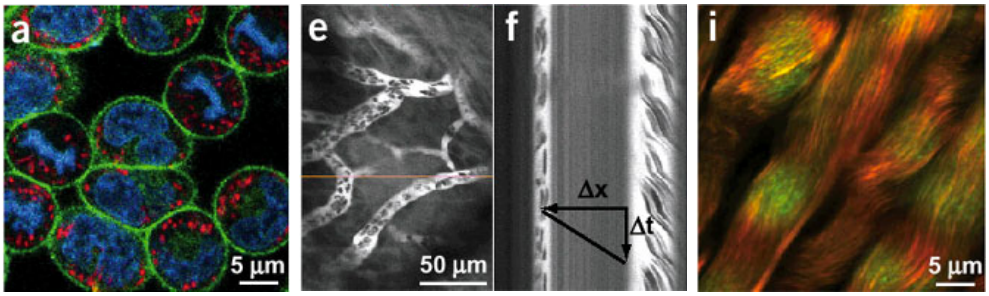

Figure 3.1. Applications Showing Various Capabilities of Multi-Photon Microscopy

(a) Simultaneous imaging of three different fluorophores in RBL-2H3 cells, commonly used as mast cell model in leukemia research, labeled with 4',6-diamidino-2-phenylindole (DAPI) (DNA, blue pseudo color), PATMAN (plasma membrane, green) and tetramethylrhodamine (mitochondria, red). (e) Blood vessels under a tibial growth plate perichondrium in a mouse. Red blood cells appear as shadows within the fluorescence-containing blood plasma. (f) The angle of the shadow traces in the linescan can be used to calculate blood flow velocity. (i) SHG imaging of collagen in a baby rat's tail tendon. Immature fibril segments scatter backward (green), whereas mature fibrils scatter forward (red) (*5*).

FLUORESCENCE OPTICAL IMAGING

Fluorescence optical imaging utilizes fluorophores to visualize biological structures. Fluorophores are compounds that absorb energy, become "excited"—the absorbed energy leads to electron transitions from the ground state to higher, excited, states—and emit light upon relaxation. They can be introduced inside live animals through genetic manipulation or injection of fluorescent dyes to label specific structures of interest; they can also be endogenous to some cellular structures. As an example of fluorophore use, one of our studies utilized Rhodamine-6G, a lipophilic dye with high cell membrane permeability, to label white blood cells and a dextran tagged with Texas Red to label blood plasma. This allowed us to visualize the cortical vasculature and the circulation of leukocytes in blood vessels.

In order to excite a fluorophore, a quantized amount of energy must be introduced to enable electrons to transition from the ground energy state to a higher excitation state. This energy can be delivered by one photon of the correct energy, or multiple photons whose energies add up to the correct amount for that particular kind of fluorophore. The energy of a photon is inversely proportional to its wavelength and can be described with the following equation:

$$E = \frac{hc}{\lambda}$$

where h is Planck's constant and c and λ are the speed and wavelength of light in vacuum, respectively.

The amount of energy required to excite a fluorophore depends on the chemical structure of that particular fluorophore compound. Once excited, the electrons relax to the ground state and emit photons that have less energy than what was absorbed due to heat loss (**Fig. 3.2**). There is a large selection of fluorophores available that use a wide range of excitation energies and exhibit an equally wide range in the energy/wavelength of emitted photons (*6*). Such diversity in fluorophore properties, coupled with the use of spectral filters and different excitation wavelengths, allow many structures labeled with different dyes to be distinguished.

TWO-PHOTON EXCITATION

Two photons can provide the same amount of energy as a single photon at half their wavelength (**Fig. 3.2**). For the 2-photon nonlinear absorption process to occur, both photons must interact with the fluorophore within about 10^{-16} s of each other, i.e. essentially simultaneously. However, the probability that two photons will be absorbed simultaneously is quadratically dependent on the light intensity. Therefore, high light intensity is required in order for this absorption to occur. In order to avoid damaging the biological sample, tightly focused, femtosecond laser pulses are exploited to achieve a sufficiently high intensity with low average power (*7*). This technique also leads to a high signal-to-noise ratio. Because two photons must simultaneously collide in order to be absorbed by a fluorophore, the only location the intensity of the femtosecond pulses are sufficiently high to cause this collision is the submicron-sized focal volume. Therefore, scattered excitation light cannot effectively generate fluorescence, leading to less background noise (*8, 9*) (**Fig. 3.3**).

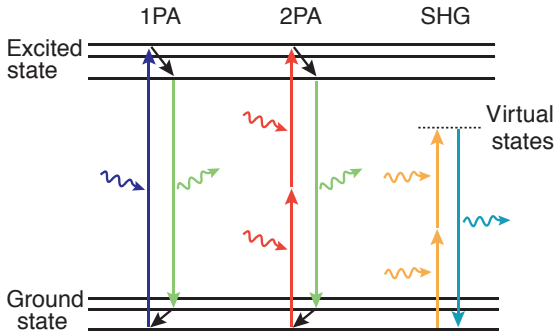

Figure 3.2: Nonlinear absorption and excitation
Energy level diagram illustrating the one- and two-photon absorption and excitation that enables fluorescence generation, as well as second harmonic generation (*10*).

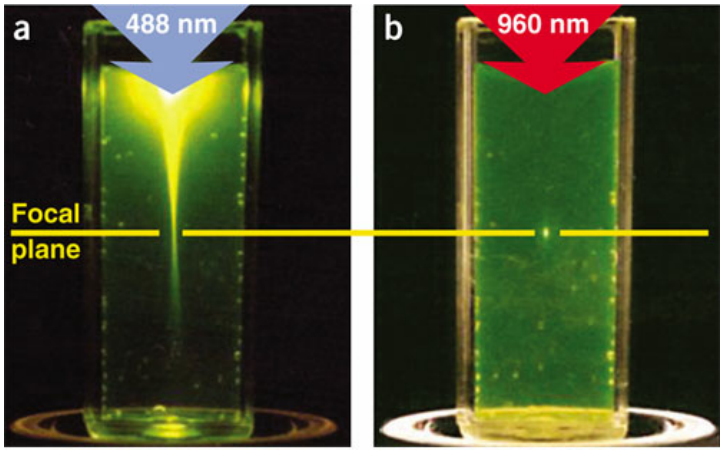

Figure 3.3: Localization of Excitation by Two-Photon Excitation
(a). Single-photon excitation of fluorescein by focused 488-nm light. (b) Two-photon excitation using focused femtosecond pulses of 960-nm light (*5*).

SECOND HARMONIC GENERATION

Another process that makes use of nonlinear optical interactions is second harmonic generation (SHG). SHG microscopy is appropriate when visualizing structures that lack inversion symmetry and are regularly oriented, such as collagen. The excitation beam interacts with the nonlinear material, effectively "combining" two photons to form a new photon with exactly half the wavelength, emitted in the same propagation direction as the input (**Fig. 3.2**). SHG is dependent on the intensity squared of the input pump. Labeling is not required for SHG to occur, but the molecules being imaged must lack inversion symmetry. Therefore, this method is widely used to study structures that are composed of collagen fibers such as corneal tissue and extracellular matrix, or to look at myosin fibers (which also lack inversion symmetry) in muscle tissue. We employed this technique to study the rearrangement of collagen fibers in engineered tissue, described in Chapter 7.

TWO-PHOTON EXCITED FLUORESCENCE MICROSCOPE SETUP

Pulse Laser Source

Titanium-sapphire (Ti:S) lasers are the most widely used in two-photon microscopy. Their repetition rate is ~100 MHz, which matches typical fluorescence lifetimes of ~10 ns, resulting in minimum saturation and maximized excitation efficiency. The wavelength can be tuned over a large range (670-1070 nm) to excite many different kinds of fluorophores. In addition, the laser power is variable,

depending on the power of the pump laser and design of the Ti:S laser cavity. For instance, an 18 W pump is able to produce approximately 3.5 W at 800 nm.

Excitation Pathway

Starting from the laser, the beam is routed through a telescope(s) to adjust the beam size to ultimately overfill the back aperture of the objective. Because the beam intensity profile is Gaussian-shaped, overfilling of the back aperture provides a compromise between maximized power transmission and optimal resolution. When the laser's ultrashort pulses propagate through optical elements in the microscope, dispersion occurs because longer-wavelength components (e.g. red) travel faster through materials than shorter-wavelength components (e.g. blue). In order to compensate for this dispersion, a prism is inserted to spatially separate the different-wavelength components, which are then forced to travel through different path lengths before being recombined. One way to implement this dispersion compensation is to place a pair of prisms at a point in the system where the laser beam propagates through twice.(*11*) Lastly, the beam intensity at the sample can be controlled using neutral-density (ND) filters or a rotatable waveplate combined with a polarizer.

Beam Scanner

An image from a 2PEF microscope is acquired by detecting fluorescence signals emitted as the laser raster scans over the region of interest. Because fluorescence is produced only in a small focal volume, the focal volume is scanned through the sample, causing fluorescence. The intensity measurement at each focus location becomes a voxel in the final image. Two rotating mirrors are used for XY

scanning over the sample. The field of view depends on how far the mirrors can rotate, while the acquisition rate depends on how fast the mirrors can move. Thus, there is a trade-off between spatial and temporal resolution. The sample or the objective is moved to adjust the imaging plane and acquire stacks of 2D images.

Detectors

The photons from sample fluorescence are emitted in all directions, but only the ones that travel back towards the microscope objective are collected. These photons reflect from a dichroic mirror that separates excitation from emission light based on their wavelength. The signal passes through a filter for the particular wavelength range being detected before reaching a photomultiplier tube, where it is then converted into a voltage measurement. This voltage signal is then digitized and recorded using software such as MPScope (*12*) or ScanImage (*13*) (**Fig. 3.4**).

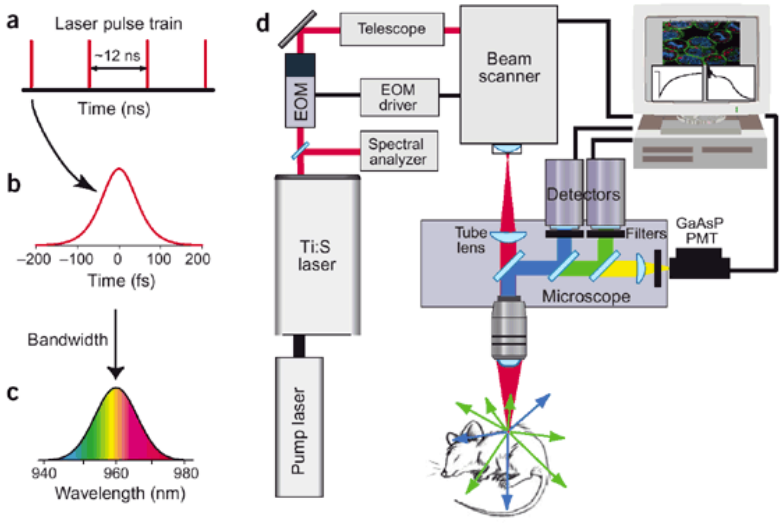

Figure 3.4: Components of a Multiphoton Microscope
(a) Pulse train from a laser mode-locked Ti:S at 80 MHz. (b) Pulses out of the laser typically have a full-width half-maximum (FWHM) duration of 100 fs and a spectral FWHM (c) of ~10 nm. (d) Schematic of a multi-photon microscopy system.

REFERENCE

1. J. N. D. Kerr, W. Denk, Imaging in vivo: watching the brain in action. *Nat Rev Neurosci* **9**, 195 (Mar 1, 2008).
2. W. Denk, K. Svoboda, Photon upmanship: why multiphoton imaging is more than a gimmick. *Neuron* **18**, 351 (Mar 1, 1997).
3. D. Kobat *et al.*, Deep tissue multiphoton microscopy using longer wavelength excitation. *Opt Express* **17**, 13354 (Aug 3, 2009).
4. M. Garcia-Alloza, B. J. Bacskai, Techniques for brain imaging in vivo. *Neuromolecular Med* **6**, 65 (Jan 1, 2004).
5. W. Zipfel, R. Williams, W. Webb, Nonlinear magic: multiphoton microscopy in the biosciences. *Nat Biotechnol* **21**, 1369 (Nov 1, 2003).
6. F. Bestvater *et al.*, Two-photon fluorescence absorption and emission spectra of dyes relevant for cell imaging. *J Microsc* **208**, 108 (Nov 1, 2002).
7. R. M. Williams, W. R. Zipfel, W. W. Webb, Multiphoton microscopy in biological research. *Curr Opin Chem Biol* **5**, 603 (Oct 1, 2001).
8. W. Denk, J. Strickler, W. Webb, Two-photon laser scanning fluorescence microscopy. *Science* **248**, 73 (Apr 6, 1990).
9. H. C. Gerritsen, C. J. De Grauw, Imaging of optically thick specimen using two-photon excitation microscopy. *Microsc Res Tech* **47**, 206 (Nov 1, 1999).
10. F. Helmchen, W. Denk, Deep tissue two-photon microscopy. *Nat Methods* **2**, 932 (Dec 1, 2005).

11. P. Tsai *et al.*, Principles, design, and construction of a two photon laser scanning microscope for in vitro and in vivo brain imaging. *In vivo optical imaging of brain function*, 113 (2002).

12. Q. Nguyen, P. Tsai, D. Kleinfeld, MPScope: a versatile software suite for multiphoton microscopy. *J Neurosci Methods* **156**, 351 (Sep 30, 2006).

13. T. A. Pologruto, B. L. Sabatini, K. Svoboda, ScanImage: flexible software for operating laser scanning microscopes. *Biomed Eng Online* **2**, 13 (May 17, 2003).

CHAPTER 4

IN VIVO TWO-PHOTON EXCITED FLUORESCENCE MICROSCOPY REVEALS CARDIAC- AND RESPIRATION-DEPENDENT PULSATILE BLOOD FLOW IN CORTICAL BLOOD VESSELS IN MICE

Thom P. Santisakultarm[1], Nathan R. Cornelius[1], Nozomi Nishimura[1], Andrew I. Schafer[2], Richard T. Silver[2], Peter C. Doerschuk[1,3], William L. Olbricht[1,4], Chris B. Schaffer[1]

[1]Department of Biomedical Engineering, Cornell University, Ithaca, NY 14853

[2]Department of Medicine, Weill Cornell Medical College, New York, NY 10065

[3]Department of Electrical and Computer Engineering, Cornell University, Ithaca, NY 14853

[4]Department of Chemical and Biomolecular Engineering, Cornell University, Ithaca, NY 14853

This research was originally published in the American Journal of Physiology Heart and Circulation Physiology. T. P. Santisakultarm *et al.*, In Vivo Two-photon Excited Fluorescence Microscopy Reveals Cardiac- and Respiration-Dependent Pulsatile Blood Flow in Cortical Blood Vessels in Mice. *Am J Physiol Heart Circ Physiol*, (Jan 20, 2012).

ABSTRACT

Subtle alterations in cerebral blood flow can impact the health and function of brain cells and are linked to cognitive decline and dementia. To understand hemodynamics in the three-dimensional vascular network of the cerebral cortex, we applied two-photon excited fluorescence microscopy to measure the motion of red blood cells (RBCs) in individual microvessels throughout the vascular hierarchy in anesthetized mice. To resolve heartbeat- and respiration-dependent flow dynamics we simultaneously recorded the electrocardiogram and respiratory waveform. We found that centerline RBC speed decreased with decreasing vessel diameter in arterioles, slowed further through the capillary bed, then increased with increasing vessel diameter in venules. RBC flow was pulsatile in nearly all cortical vessels, including capillaries and venules. Heartbeat-induced speed modulation decreased through the vascular network, while the delay between heartbeat and the time of maximum speed increased. Capillary tube hematocrit was 0.21 and did not vary with centerline RBC speed or topological position. Spatial RBC flow profiles in surface vessels were blunted compared to a parabola, and could be measured at vascular junctions. Finally, we observed a transient decrease in RBC speed in surface vessels prior to inspiration. In conclusion, we have developed an approach to study detailed characteristics of RBC flow in the three-dimensional cortical vasculature, including quantification of fluctuations in centerline RBC speed due to cardiac and respiratory rhythms and flow profile measurements. These methods and the quantitative data on basal cerebral hemodynamics open the door to studies of normal and disease state cerebral microcirculation.

INTRODUCTION

The complex, three-dimensional vascular architecture of the brain presents a challenge to studies of microvascular hemodynamics. Larger arterioles form a net at the cortical surface and give rise to penetrating arterioles that plunge into the brain and feed capillary networks, where most nutrient and metabolite exchange occurs (*1*). These capillaries coalesce into ascending venules, which return to the cortical surface and drain into larger surface venules (*2*). Several lines of evidence suggest that even small changes in hemodynamics in the brain can have detrimental impacts on the health and function of neurons. Chronic diseases that alter microcirculation, such as hypertension (*3*) and diabetes (*4*), are risk factors for dementia and are linked to cognitive decline (*5*). Flow disruptions from hyperviscous blood in diseases such as polycythemia vera and essential thrombocythemia are linked to neural degeneration (*6*). In addition, occlusion of cerebral microvessels may cause the small, clinically silent, strokes that have been associated with cognitive impairment and are a risk factor for dementia (*7*). Furthermore, decreases in the pulsatility of blood flow results in higher systemic vascular resistance, decreased oxygen metabolism, and reduced efficiency of the microcirculation (*8*). Novel methods that enable quantification of blood flow and vascular changes at the level of individual microvessels in the complex cortical vasculature would greatly improve our understanding of the causes and consequences of such microvascular pathologies as well as provide insight into normal-state hemodynamic regulation.

The most extensive data on blood flow dynamics in microvascular networks come from two-dimensional vascular beds, such as the cremaster muscle, omentum, and the mesentery, where experimental techniques such as widefield intravital microscopy can be readily applied. In these systems, studies of average blood flow speed in individual microvessels (*9*), the distribution of red blood cells (RBCs) at microvascular junctions (*10*), as well as flow pulsatility in capillaries (*9*) have been made. These data have fueled detailed modeling of blood flow dynamics in microcirculatory networks that has elucidated the biophysical and physiological principles that govern flow (*11-14*).

In early studies of brain microcirculation, the average flow speed and pulsatility of flow in cortical surface vessels was characterized (*15*), and more recent work has measured flow profiles in pial arterioles using Doppler optical coherence tomography (*16*). However, because of the three-dimensional vascular architecture of the brain, techniques with the ability to resolve flow in microvessels at different depths in the tissue are required to quantify flow dynamics throughout the vascular hierarchy. Recently, two-photon excited fluorescence (2PEF) microscopy has emerged as an approach to quantify flow changes in individual cortical microvessels in response to neural activity (*17*) and microvascular occlusion (*18-20*), with the potential to access vessels throughout the full cortical thickness of a mouse (*21*). However, the careful quantification of blood flow dynamics that has been done in two-dimensional microvascular beds has not yet been performed in brain vascular network. For example, previous work has not mapped average flow speed nor heartbeat-induced

flow modulation in vessels throughout the cortical network, measured spatial flow profiles in brain microvessels, or quantified important hemodynamic parameters such as pulse wave velocity.

Our work aims to overcome the challenges of quantifying blood flow dynamics in three-dimensional microvascular networks in live animal models. We coupled electrocardiogram (EKG) and respiratory waveform measurements with 2PEF-based assessment of RBC speed in individual vessels in anesthetized mice. We quantified average centerline RBC flow speed as well as temporal flow fluctuations due to cardiac and respiratory rhythms in cortical arterioles, capillaries, and venules. Interestingly, we found pulsatile RBC flow in vessels throughout the cortical network, including capillaries and venules, and identified respiration-dependent changes in cortical blood flow. We quantified the tube hematocrit in brain capillaries and found no dependence on centerline RBC speed or position in the vascular hierarchy. We also measured time- and space-dependent RBC flow profiles in arterioles, venules, and at vascular junctions, and found that spatial flow profiles were blunted in most vessels. These data provide a detailed quantification of cerebral hemodynamics in brain microvessels, while the methods we developed open the door to future studies of alterations in brain hemodynamics due to cerebrovascular disease.

MATERIALS AND METHODS

Animals and surgical preparation

We used 19 male and three female adult (3-7 month-old), wild-type C57BL/6 mice, 18-31 g in mass, in this study. Animals were anesthetized with 5% isoflurane in oxygen and maintained at 1.5-2% during surgery and imaging. Glycopyrrolate (0.05 mg per 100-g mouse) was intramuscularly injected to facilitate respiration. Bupivacaine (0.1 mL, 0.125%) was subcutaneously administered at the incision site to provide local anesthesia. A 5-mm craniotomy was prepared over the parietal cortex. An 8-mm diameter, No. 1.5 glass cover slip (50201; World Precision Instruments) was glued to the skull using cyanoacrylate (Loctite) and dental cement (Co-Oral-Ite Dental Mfg Co.). The space between the exposed brain and the cover glass was filled with artificial cerebrospinal fluid (*22*). Mouse body temperature was maintained at 37.5° C with a feedback controlled heating blanket (50-7053P; Harvard Apparatus). Subjects received 5% (w/v) glucose in physiological saline (0.5 mL per 100-g mouse) hourly. To fluorescently label the vasculature, 0.1 mL of a 2.5% (w/v) solution of 70-kDa Texas Red-dextran (D1830; Invitrogen) or 70-kDa fluorescein-conjugated dextran (FD70S; Sigma) in physiological saline was injected retroorbitally. The resulting dextran concentration in the blood was about 0.0015 g/mL, well below the concentration required to trigger RBC aggregation (*23*). No RBC aggregation was observed in our experiments. The care and experimental manipulation of our animals have been reviewed and approved by the Institutional Animal Care and Use Committee at Cornell University.

In vivo *two-photon excited fluorescence imaging of cerebral blood vessels*

Images were obtained using a custom-built 2PEF microscope that utilized a train of 1040-nm, 1-MHz, 300-fs pulses from a Yb-fiber chirped pulse amplifier (FCPA μJewel D-400; IMRA America, Inc.) for two-photon excitation of Texas Red or a train of 800-nm, 87-MHz, 100-fs pulses from a Ti:sapphire laser oscillator (MIRA HP, pumped by a Verdi-V18; Coherent, Inc.) for fluorescein. The laser pulses were scanned in a raster pattern by galvanometric mirrors that are imaged to the back aperture of the objective. The two-photon excited fluorescence is reflected by a dichroic mirror and relayed to a photomultiplier tube through a filter centered at 645 or 517 nm, both with 65-nm bandwidth, for Texas Red and fluorescein imaging, respectively. Laser scanning and data acquisition was controlled by MPScope software (*24*). Low magnification images of the vasculature in the entire cranial window were taken using a 0.28 numerical aperture (NA) 4X air objective (Olympus) (**Fig. 4.1A**). For high-resolution imaging (**Fig. 4.1B**), RBC flow speed measurements (**Fig. 4.1E** and **1F**), and vessel diameter measurements (**Fig. 4.1C** and **1D**), we used a 0.95-NA, 20X water immersion objective (Olympus).

To map vascular topology and determine vessel classes (i.e. arteriole vs. capillary vs. venule), stacks of images spaced 1 μm axially through the top 350 μm of the cortex were obtained (**Fig. 4.1B**). Penetrating arterioles were identified as vessels that branched from readily-identifiable surface arterioles and plunged vertically into

the brain. We confirmed the flow was into the brain using line-scan measurements (see below). Similarly, ascending venules had flow that emerged from the brain and drained into readily-identifiable surface venules. We classed all sub-surface vessels branching from penetrating arterioles and ascending venules as capillaries, and determined the number of capillary segments separating each capillary from the topologically nearest penetrating arteriole or ascending venule. The depth of each capillary was measured relative to the middle of the cortical surface vessels. We measured blood flow speed and diameter of surface vessels and capillaries up to ten branches downstream and upstream from penetrating and ascending vessels, respectively. To determine vessel diameter, we recorded images of individual vessels stepping from above to below the vessel. These images were averaged, and diameters were calculated by manually selecting a portion of the vessel, calculating the area above threshold (20% of maximum intensity), and divided this by the length of the selected segment.

2PEF measurement of RBC flow speed

The intravenously-injected dye labels only the blood plasma, so RBCs appear as moving dark patches within the vessel lumen. Tracking the motion of these dark patches enables measurement of centerline RBC flow speed. We tracked RBC motion by repetitively scanning a line along the central axis of single vessels at a line rate of 1.7 kHz for at least 30 s (*17, 20*). The space-time image produced by the line-scan

contained diagonal dark streaks formed by moving RBCs, with a slope that is inversely proportional to the centerline RBC speed (**Fig. 4.1E** and **1F**).

Determination of RBC flow speed from line-scan images

To quantify RBC speed in individual vessels from the space-time images, we used a Radon transform-based algorithm similar to that of Drew et al. (*25*). Low spatial frequency components in the line-scan image were filtered with a high-pass isotropic Gaussian filter. The frequency response of the filter was one minus a scaled Gaussian, centered at zero frequency, with a diagonal covariance matrix with values of 25 pixel^{-2}, and the scaling set so the frequency response at zero frequency is zero. Eliminating low-frequency components, such as vertical streaks in the space-time image that arise from stationary artifacts in the blood vessel, greatly decreased the amount of noise and accentuated the difference between the dark and light streaks formed by moving RBCs.

$$g(\rho,\theta) = \int_{-\infty}^{\infty}\int_{-\infty}^{\infty} g(x,y)\,\delta(\rho - x\cos\theta - y\sin\theta)\,dx\,dy \qquad \textbf{[1]}$$

We then performed a Radon transform on the filtered data, which computes line integrals of a two-dimensional function g(x,y) at different angles, θ, from 0 to π with respect to the y-axis and at different radial offsets from the origin, ρ, to yield a new function g(ρ, θ). When θ = θ* matches the angle of the streaks in a line-scan image, the fluctuations of g(ρ,θ*) with respect to ρ are greatest. To identify θ*, we found the value of θ where the variance along the ρ-axis was a maximum. The RBC speed is

then equal to $\tan^{-1}\theta^*$ multiplied by time and length coefficients that depend on the line-scan rate and the spatial extent of the line-scan image. For vessels on the brain surface, the image plane was aligned with the plane of the vessel. For sub-surface capillaries, there was sometimes a small angle between the image plane and the vessel. These angles were measured from the 3D image stacks for each capillary, and the calculated centerline RBC flow speed was divided by the cosine of this angle.

Alignment of flow speed measurements to the cardiac cycle

To measure the temporal centerline RBC flow profile during a cardiac cycle, we placed intramuscular leads in the animal's left anterior and right posterior limbs. The EKG signal was amplified (ISO-80 Bio-Amplifier; World Precision Instruments, Inc.) and recorded (3.4-kHz sampling rate) simultaneously with the line-scan data (**Fig. 4.1G**). The temporal locations of R-waves (identified by thresholding) in the EKG signal were used as markers to align centerline RBC speed measurements from each cardiac cycle. A moving average of the RBC flow speed over the cardiac cycle was computed with a window size of approximately 1.5% of the cardiac cycle (**Fig. 4.1H**). The modulation depth of the flow speed was calculated by normalizing the difference between the maximum and minimum flow speed across the cardiac cycle by the average flow speed. A vessel was designated as having no flow modulation if the difference between maximum and minimum centerline RBC flow speed was less than the standard deviation of the speed across the cardiac cycle. The delay between heartbeat (R-wave) and the time of maximal flow speed for vessels with flow

modulation was calculated and normalized by the average time between heartbeats. This delay was aggregated across multiple vessels and animals by temporally aligning all measurements using the R-wave of the EKG.

Estimation of capillary tube hematocrit

Tube hematocrit, hct_{tube}, was calculated from (*26*)

$$hct_{tube} = \frac{fV_{RBC}}{v\pi R^2} \quad \textbf{[2]}$$

where f, v, and R are RBC flux, centerline RBC speed, and vessel radius, respectively. RBC flux was extracted from line-scan data by manually counting the number of cells in ten 0.3-s time segments, spaced by 3 s throughout the measurement. We only included vessels with single file RBC motion, where each RBC made a distinct streak in the space-time image. This excluded all capillaries with RBC flux above 270 RBCs/s, where manual counting of RBC flux was unreliable. We took the mean corpuscular volume of mouse RBCs, V_{RBC}, to be 45 μm^3 (*27*).

Spatial blood flow profile measurement

To obtain a spatial RBC flow profile in individual surface vessels, line-scans were sequentially recorded as a function of lateral position, from one vessel wall to the other with a step size of 2-4 μm, all in a horizontal plane located at the depth where the vessel was widest. The blood flow speed data from all line-scan measurements was temporally aligned using the EKG to obtain time- and space-dependent flow profiles

in individual vessels (**Fig. 4.5**). The data was smoothed first temporally and then spatially using moving averages with a temporal width of ~1.5% of the cardiac cycle and a spatial extent of three adjacent line-scans, respectively. For each vessel, the spatial flow speed profile, v(r), was fit using the equation (*28*),

$$v(r) = v_{max}\left(1 - \left|\frac{r}{R}\right|^{k}\right) \quad \textbf{[3]}$$

where R is the vessel radius, k represents the degree of blunting (a value of two corresponds to a parabolic profile), and v_{max} is the maximum flow speed. Similar measurements were made before, at, and after bifurcations or mergers in surface arterioles and venules, respectively (**Fig. 4.5**). In arteriole (venule) measurements, the RBC speed profile in the upstream vessel(s) was characterized about one vessel diameter upstream from the bifurcation (merger), while downstream branch(es) were characterized immediately after the bifurcation (merger).

Alignment of flow speed measurements to the respiratory cycle

To measure the temporal RBC flow speed profile during each respiratory cycle, a breathing signal was recorded simultaneously with EKG and line-scan data using a locally-designed breathing sensor. Briefly, an 805-nm light-emitting device (LED) illuminated the back of the mouse above the chest cavity from a distance of approximately 1 cm. The amplitude of the LED emission was sinusoidally modulated at 2 kHz. A photodiode located adjacent to the LED detected the light reflected from the animal. The photodiode signal was amplified using a lock-in amplifier (SR530;

Stanford Research Systems) with a 30-ms time constant using the 2-kHz LED modulation as a reference. As the animal inhales and exhales, the amount of light reaching the photodiode changes slightly, allowing continuous monitoring of the breathing waveform (**Fig. 4.7A**, top). Line-scan data were recorded concurrently with both EKG and breath signals for 10 minutes. To align RBC flow speed data with the respiratory cycle, we used the same method described for cardiac cycle alignment, but using the inspiration signal as the alignment marker (**Fig. 4.7B**). To align flow speed data with both the cardiac and respiratory waveforms, we used R-waves of the EKG signal and inspiration peaks of the respiratory signal as markers and binned each flow speed measurement into a two-dimensional matrix that specifies the measurement time with respect to both heartbeat and inspiration. The data was then smoothed using a rectangular two-dimensional moving average that had a width of 5% of the cardiac cycle and a length of 5% of the respiratory cycle. The data was used to create a three-dimensional plot that decoupled RBC flow speed dependence on heartbeat and breathing (**Fig. 4.7D** and **7E**).

RESULTS

Temporal blood flow fluctuations due to rhythmic cardiac contractions

We used 2PEF imaging of fluorescently-labeled vasculature in craniotomized, anesthetized mice to quantify the temporal blood flow dynamics in cortical microvessels. Vascular topology was traced in three-dimensional image stacks to identify surface and penetrating arterioles, capillaries, and ascending and surface venules (**Fig. 4.1A** and **1B**). We measured diameter and centerline RBC flow speed (by tracking RBC motion) in individual arterioles (**Fig. 4.1C** and **1E**), capillaries (**Fig. 4.1D** and **1F**), and venules. RBC speed measurements in each vessel were temporally aligned to heartbeat (**Fig. 4.1H**). The average cardiac period was 0.14±0.04 s (mean ± standard deviation), which corresponds to a heart rate of 430±100 bpm (20 mice). Arteriole temporal centerline RBC flow profiles typically displayed a clear speed modulation with heartbeat (**Fig. 4.1Hi**), while capillaries (**Fig. 4.1Hii**) and venules (**Fig. 4.1Hiv**) showed smaller modulation depth, with speed modulation not detectable above noise in some capillaries (**Fig. 4.1Hiii**) and venules. The delay between the heartbeat and the time of maximum centerline RBC flow speed was shortest in arterioles, followed by capillaries, then venules (**Fig. 4.1H**).

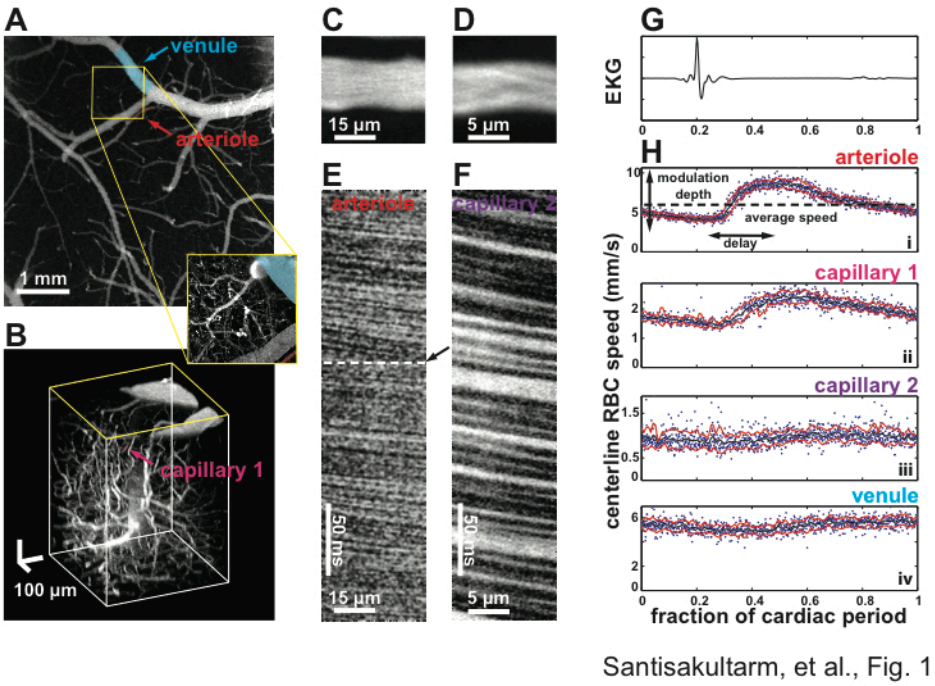

Fig. 4.1. In vivo 2PEF imaging of vascular topology and cerebral blood flow during the cardiac cycle. (A) Low magnification 2PEF image of fluorescently-labeled brain vasculature in an anesthetized mouse. (B) Three-dimensional rendering of the vasculature with the brain surface at the top of the image. Axially-projected image of an arteriole (C) and a capillary (D) with their line-scan images (E and F). The arrow in (E) indicates RBC flow speed increase due to a heartbeat. (G) EKG used to align the flow speed data. (H) Centerline RBC speed of an arteriole (i), two capillaries (ii and iii), and a venule (iv) as a function time, expressed as a fraction of the cardiac cycle. The colors of the vessel labels in H correspond to the colored highlights in the 2PEF images and line-scan images.

Quantification of average RBC flow speed and heartbeat-dependent speed fluctuations

We measured temporal RBC speed profiles in microvessels throughout the cortical vascular hierarchy. Centerline RBC flow speed (averaged over ~200 cardiac cycles) significantly decreased (from 13 to 3 mm/s) with decreasing diameter (60 to 10 μm) in surface and penetrating arterioles ($p < 0.0003$, Cuzick's trend test (*29*), 66 vessels, 14 animals) (**Fig. 4.2A**). Capillaries (<10-μm diameter) exhibited the slowest RBC flow speeds of 1.5±1.2 mm/s (156 vessels, 17 animals), with capillaries topologically closer to arterioles having significantly higher flow speeds than those closer to venules ($p < 0.0001$, Cuzick's trend test, **Fig. 4.2D**). We found no dependence of capillary blood flow speed on the depth of the vessel beneath the cortical surface (**Fig. 4.3**). Flow speed significantly increased (1 to 4 mm/s) with increasing vessel diameter (10 to 60 μm) in ascending and surface venules ($p < 0.0001$, Cuzick's trend test, 56 vessels, 14 animals), but remained slow compared to arterioles ($p < 0.0001$, two-sided t-test, **Fig. 4.2A**). The average magnitude of the centerline RBC flow speed modulation with heartbeat decreased continuously from arterioles (43±15%, 61 vessels) to capillaries (28±12%, 81 vessels) to venules (10±8%, 54 vessels) ($p < 0.0001$, ANOVA, **Fig. 4.2B** and **2E**). The flow modulation was undetectable in many of the slower vessels (**Fig. 4.2B**, inset), especially in capillaries topologically further from penetrating arterioles (**Fig. 4.2E**, inset). Nearly all venules exhibited some modulation in blood flow speed with heartbeat. The delay between heartbeat and the time of maximum RBC flow speed significantly increased

for vessels topologically further away from the heart ($p < 0.0001$, Cuzick's trend test, **Fig. 4.2C** and **2F**)

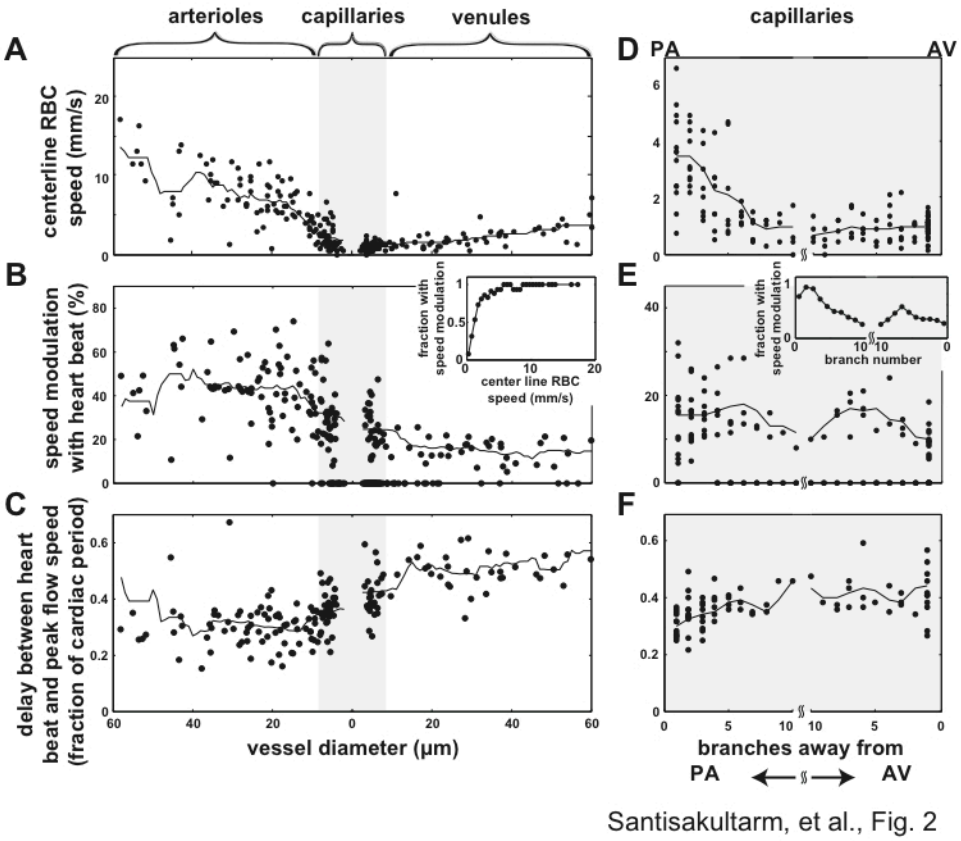

Fig. 4.2. Average centerline RBC speed, flow speed modulation, and delay to maximal flow speed for cerebral microvessels. (A) Average centerline RBC speed, (B) flow speed modulation with heartbeat, and (C) delay between heartbeat and time of maximal flow speed as a function of vessel diameter. To display the progression of blood flow through the vascular network, data for arterioles (venules) are displayed on the left (right) portion of the plot with decreasing (increasing) diameter. Capillaries are toward the middle and placed to the arteriole or venule side based on which they are topologically closer to. (D) Average centerline RBC speed, (E) flow speed modulation with heartbeat, and (F) delay between heartbeat and time of maximal flow speed for capillaries as a function of topological connectivity to penetrating arterioles (PA) from the left side and to ascending venules (AV) from the right side.

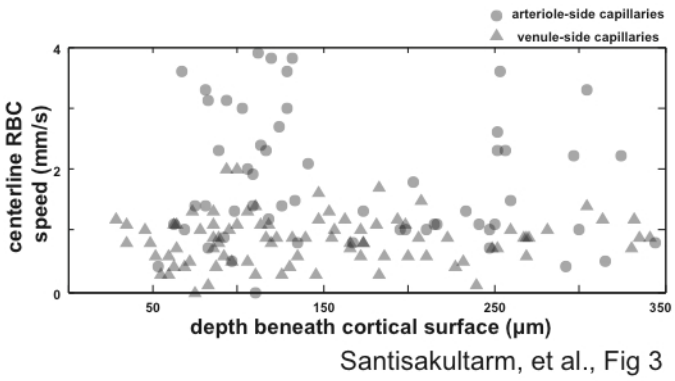

Fig. 4.3. Capillary RBC flow speed as a function of depth beneath the cortical surface.

Capillary tube hematocrit

We manually counted RBC flux in the line-scan data and determined the tube hematocrit of many of the capillaries using Eq. 2. We found that the average capillary hematocrit was 0.22±0.19 (n = 97 capillaries), with a weak tendency for hematocrit to increase for smaller diameter vessels ($p = 0.0005$, Cuzick's trend test, **Fig. 4.4A**), where RBCs deform significantly as they squeeze through the capillary and thus occupy a larger volume fraction. Tube hematocrit did not depend on the mean centerline flow speed in the capillary over the narrow range of flow speeds investigated (*26*) (**Fig. 4.4B**) or on the topological position of the capillary in the vascular bed (**Fig. 4.4C**).

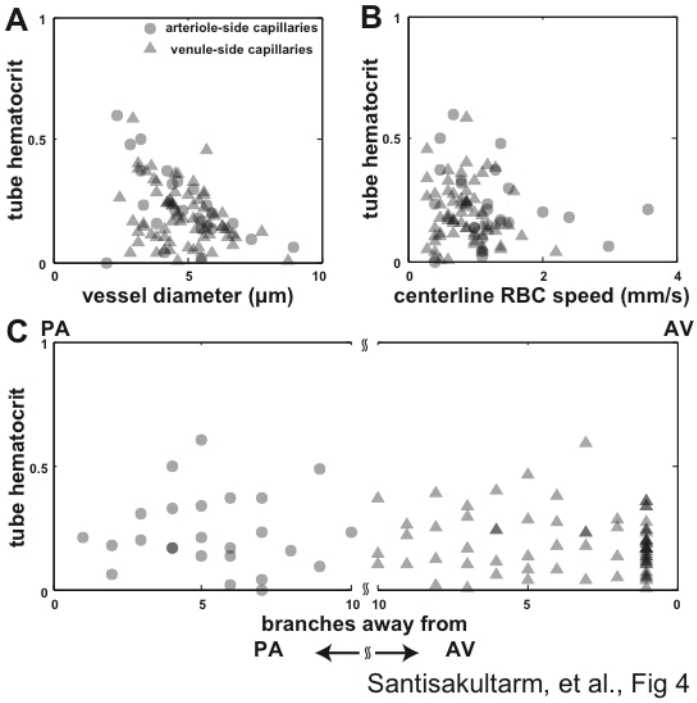

Fig. 4.4. Capillary tube hematocrit in the cortical microvascular network. Tube hematocrit as a function of (A) capillary diameter, (B) centerline RBC speed, and (C) topological connectivity to penetrating arterioles (PA) from the left side and to ascending venules (AV) from the right side.

Spatial blood flow profiles during a cardiac cycle

Spatial RBC flow profiles were obtained in vessels by measuring RBC flow speed at different positions within the vessel lumen. In both arterioles (**Fig. 4.5B**) and venules (**Fig. 4.5C**), flow speed was fastest in the center of the vessel and decreased toward the vessel walls. In both vessel classes, the spatial RBC flow profile was slightly blunted (average blunting index, k, of 3.3±1.1 in arterioles; k = 3.7±1.5 in venules) as compared to the parabolic flow profile expected for steady laminar flow (**Fig. 4.5Biii** and **5Ciii**). In arterioles, the degree of blunting was significantly higher at diastole (k = 3.4±1.1) as compared to systole (k = 3.1±1.1; p = 0.002, paired t-test). Vessels with slower flow speeds tended toward increased blunting regardless of vessel class or cardiac phase (**Fig. 4.5D**).

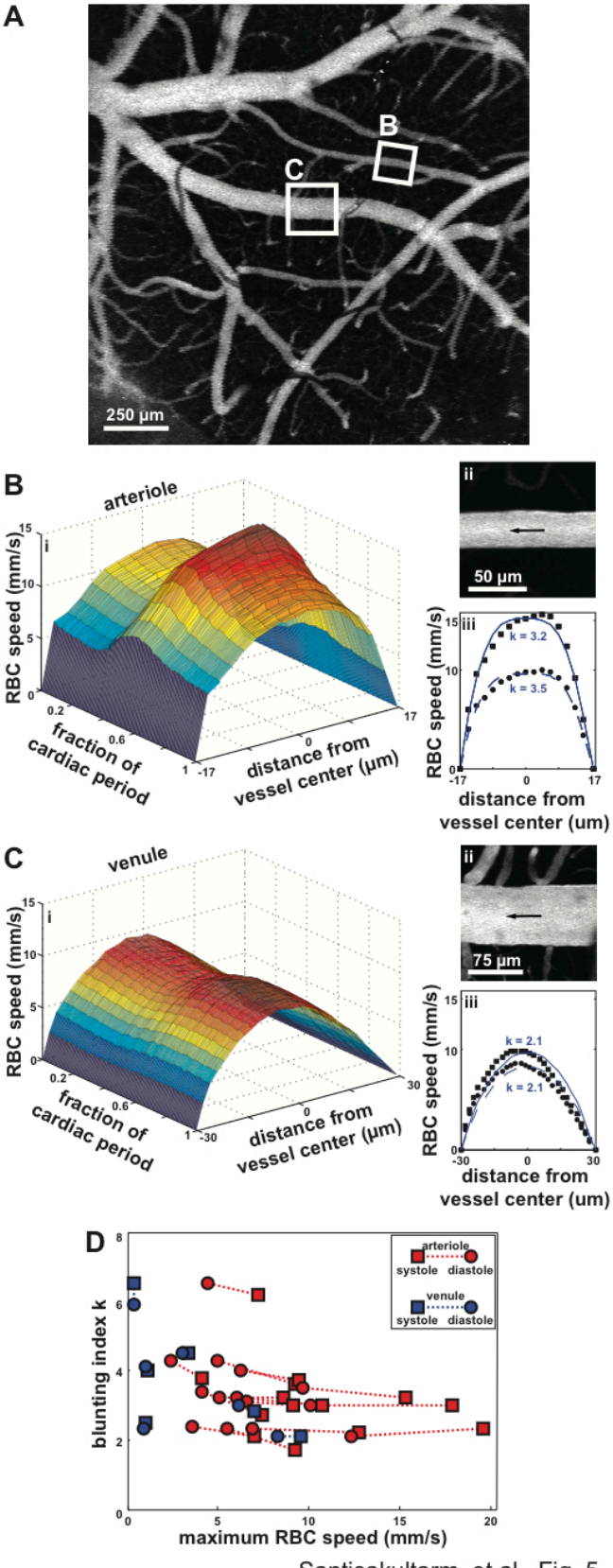

Santisakultarm, et al., Fig. 5

Fig. 4.5. RBC flow speed across the spatial profile of an arteriole and venule over the cardiac cycle. (A) Low magnification 2PEF image of fluorescently-labeled brain vasculature. RBC speed from wall-to-wall across a surface arteriole (Bi) and a surface venule (Ci) over the cardiac cycle with corresponding 2PEF images of the vessels (Bii and Cii). The spatial flow speed profiles during systole and diastole are also displayed (Biii and Ciii). (D) Blunting index, k, of surface arterioles and venules as a function of maximum RBC flow speed during systole and diastole, determined from fits of the flow profile at systole and diastole to Eq. 3.

We measured spatial RBC flow speed profiles upstream from, at, and downstream from surface arteriole bifurcations (**Fig. 4.6A**) and surface venule mergers (**Fig. 4.6C**). At the arteriole bifurcation, a spatial flow profile with two peaks was observed, while the peaks in the downstream branches were shifted laterally toward the outer sides of the vessels (**Fig. 4.6B**). Similarly, at the venule merger, a double-peaked flow profile was observed (**Fig. 4.6D**). We found that RBC flux (calculated assuming an axially symmetric flow profile) was conserved to within 30% and 11% in the arteriole and venule junctions, respectively. These errors likely reflect the fact that there was some physiological drift during the approximately one-hour time required to take all the necessary line-scan measurements and that the downstream flow profiles this close to a junction are likely not fully axially symmetric. Because our approach for measuring flow speed relies on tracking RBC motion, the flow profiles in Figs. 5 and 6 are effectively spatially-averaged over the ~7-μm size of an RBC. This averaging likely reduces the depth of the dip in flow speed observed at the center of the flow profile in the bifurcation and merger shown in **Fig. 4.6B** and **D**, respectively.

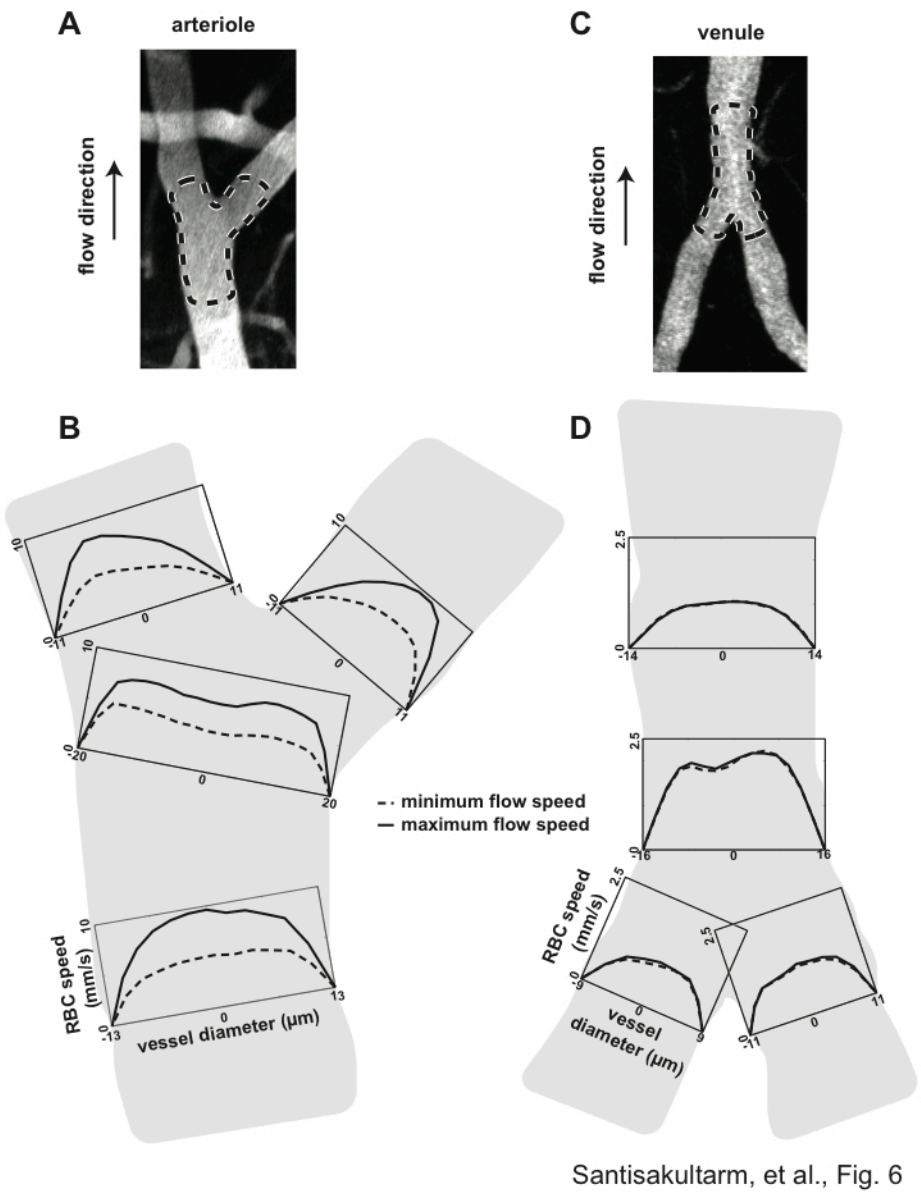

Fig. 4.6. Spatial RBC flow profiles upstream, at, and downstream of vascular junctions. (A) 2PEF image of an arteriole bifurcation. (B) Wall-to-wall flow profiles in the upstream arteriole, at the bifurcation, and in the downstream branches during systole and diastole. (C) 2PEF image of a venule merger and (D) corresponding flow profiles.

Temporal blood flow fluctuations due to breathing

In two animals, we measured centerline RBC flow speed in surface arterioles and venules while monitoring both respiration and heartbeat (**Fig. 4.7A**), and then aligned the flow speed data with respect to both respiratory (**Fig. 4.7B**) and cardiac (**Fig. 4.7C**) cycles. In arterioles (**Fig. 4.7D**) and venules (**Fig. 4.7E**), we observed a 33±5% (3 vessels, 2 animals) and 29±15% (3 vessels, 2 animals) decrease in blood flow speed just before inhalation (defined by chest wall motion), respectively (**Fig. 4.7F**). This flow speed decrease was preserved at all phases of the cardiac cycle, and occurred significantly earlier in arterioles (0.08±0.004 of a breath period before inhalation) than in venules (0.05±0.012; $p = 0.004$, two-tailed t-test; **Fig. 4.7G**). To rule out motion artifact as a source of this observation, we measured RBC flow speed at locations shifted by ~10 μm horizontally and vertically from the center axis of an arteriole and found a similar decrease in flow speed just prior to inspiration at all locations (**Fig. 4.8**).

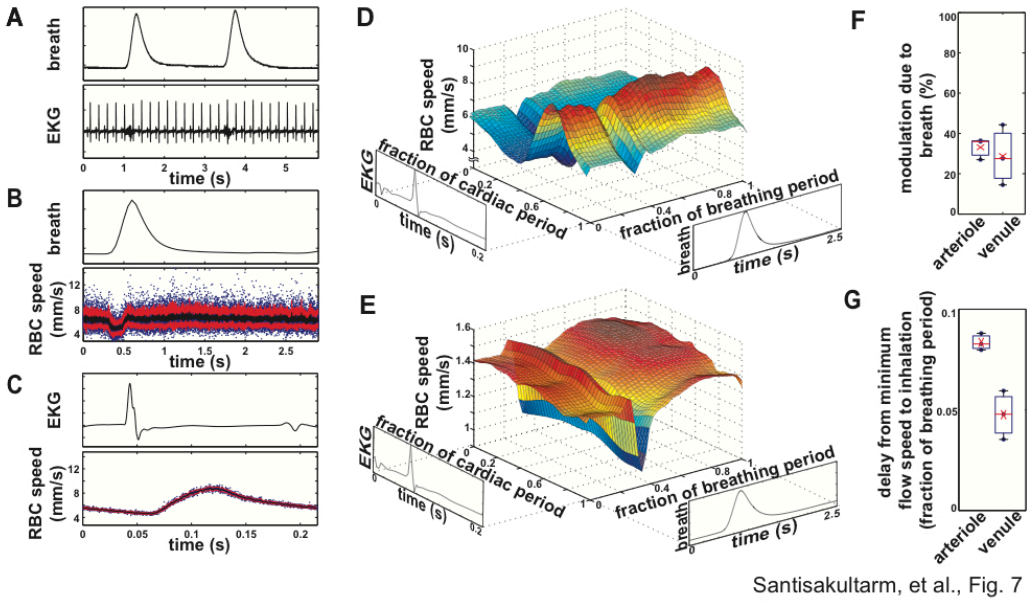

Fig. 4.7. Centerline RBC flow speed dependence on respiration and heartbeat. (A) Simultaneously recorded respiratory waveform and EKG. Centerline RBC flow speed in an arteriole aligned relative to respiratory (B) and cardiac (C) cycles. Two-dimensional plot of RBC flow speed in an arteriole (D) and a venule (E) as a function of both respiratory and cardiac cycle. Boxplot of flow speed modulation due to breathing (F) and delay from the time of the respiration-dependent decrease in flow speed to inspiration (G) in surface arterioles and venules.

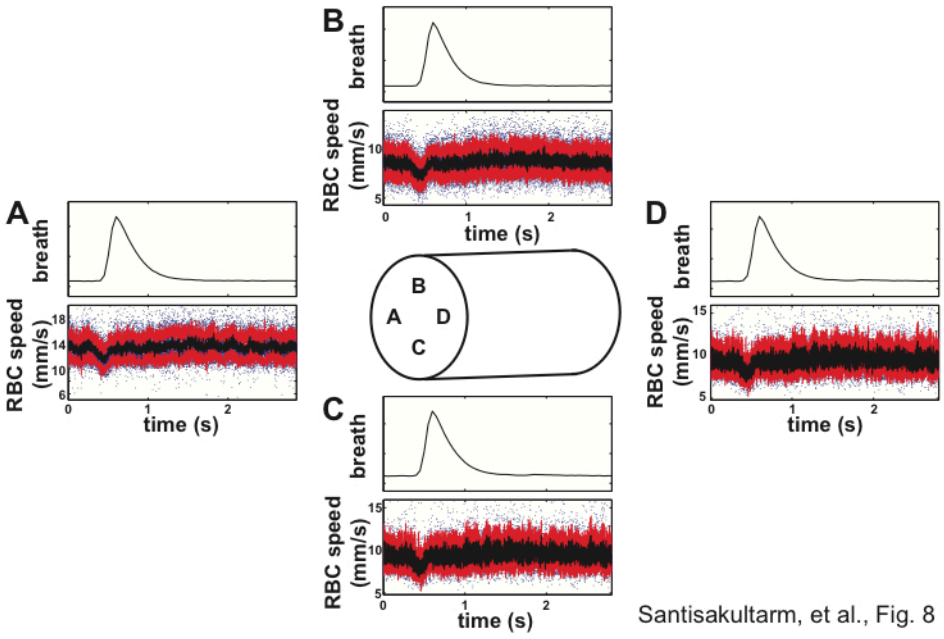

Fig. 4.8. Respiration-dependent flow speed fluctuations at different positions inside the lumen of a 43-µm diameter cortical arteriole. Each flow speed measurement was displaced approximately 10 µm from the vessel center in the direction indicated by the schematic at center of the figure.

DISCUSSION

Average RBC flow speed in cerebral vessels

We quantified centerline RBC flow speed in vessels throughout the cortical vascular hierarchy, starting from surface and penetrating arterioles, continuing to capillaries within the three-dimensional network deep in the cortex, and finally to ascending and surface venules. As expected, centerline RBC flow speed decreased with decreasing vessel diameter in arterioles, further slowed in capillaries, then increased slightly with increasing vessel diameter in venules (**Fig. 4.2A**). In capillaries, flow speeds decreased about three-fold over the first five capillary branches downstream from penetrating arterioles, then remained relatively uniform, at about 1 mm/s, through the rest of the capillary bed (**Fig. 4.2D**), with no dependence on depth beneath the cortical surface (**Fig. 4.3**). The average flow speeds for different class vessels measured here agree well with previous measurements of cerebral blood flow in rodents for arterioles (*19, 20*), capillaries (*17*), and venules (*15, 30*).

Pulsatile flow due to heartbeat

Pulsatile RBC flow was observed in all classes of cortical microvessels, including capillaries and venules, with a decreasing modulation depth from arterioles to capillaries to venules (**Fig. 4.2B**). In the majority of vessels of all classes, flow speed was modulated by heartbeat, although some of the slower capillaries and venules did not clearly show modulation. However, the variability in RBC speed was proportionally larger in these slower vessels, reducing our ability to resolve heartbeat-

induced speed changes. As a result, the decrease in the number of vessels showing modulation with decreasing average flow speed may be due, in part, to this decreased sensitivity. Our data thus establishes the minimum fraction of vessels whose flow speed is modulated by heartbeat. In previous work, heartbeat-induced speed modulation has been quantified in the aorta (*31*) and in large arteries (*32*) and veins (*33*) in the thoracic cavity of larger animals such as pigs and dogs. Pulsatile flow has also been observed in surface arterioles and venules in the brain of rodents (*15*) and in two-dimensional microvascular beds such as omentum and mesentery (*34*). Due to limitations in the spatial and temporal resolution as well as flow speed measurement precision of previous approaches, the pulsatility of blood flow in cortical venules and microvessels less than 10-μm diameter was not observed until now. The magnitude of the heartbeat-induced speed modulation decreased in more distal vessels, consistent with dampening of the pressure pulse from the heartbeat as it travels through the distensible vascular network and loses energy to viscous damping (*12*) (**Fig. 4.2B**).

As expected, the interval between ventricular ejection and the time of maximum flow speed increased for more distal vessels (**Fig. 4.2C** and **2F**) because the pressure wave from the heartbeat must travel through the distensible vascular system (*35*). The interval between the time of maximal flow speed in penetrating arterioles and ascending venules was about 0.02 s, on average (**Fig. 4.2C**). In mouse cortex, the shortest capillary path from a penetrating arteriole to an ascending venule has a median value of 490 μm (330 - 670 μm interquartile range, private communication

from P. Tsai based on data in Ref. (*36*)). Using these data, we estimate the pulse wave velocity through the cortical capillary network to be ~25 mm/s.

In microvessels, the propagation of the pressure pulse from the heart is dominated by viscous forces and is described by a diffusion equation (*13, 14*)

$$\frac{d^2P}{dx^2} = GC\frac{dP}{dt} \quad \textbf{[4]}$$

where P is the intraluminal pressure as a function of position along the vessel, x, and time, t. The viscous resistance term, G, is giving by

$$G = \frac{8\mu}{\pi R^4} \quad \textbf{[5]}$$

where μ is the viscosity of blood and R is the vessel radius. The vascular compliance, C, is described by

$$C = \frac{3\pi R^2(a+1)^2}{E(2a+1)} \quad \textbf{[6]}$$

where a is the ratio of vessel radius to vessel wall thickness and E is the Young's modulus of the vessel wall. The solution to Eq. 4 is a strongly damped oscillatory wave that propagates with a speed, c, given by

$$c = \sqrt{\frac{2\omega}{GC}} \quad \textbf{[7]}$$

where ω is the angular frequency of the heartbeat. To determine the blood viscosity, we followed the approach of Ref. (*37*), using a tube hematocrit of 0.22 and vessel radius of 2.9 μm (the averages for the capillaries in this study). We found the relative viscosity to be 1.2, which yields a whole blood viscosity in the capillary bed of 1.6 X

10^{-3} Pa s (*38*). Using the 25 mm/s pulse wave velocity we estimated experimentally, a vessel wall thickness of 0.5 μm (*39*), and the measured average 7.1-Hz heart rate, Eq. 7 can be solved for the Young's modulus of the vessel, giving a value of 0.12 MPa. This value for the modulus of brain capillaries is in fair agreement with measurements of microvessel modulus from rat spinotrapezius muscle (*40*), but smaller than previous estimates in cat omentum and mesentery (*41, 42*).

Spatial flow profiles in surface arterioles and venules

Blood is composed of both cellular components and the liquid blood plasma. For arteries and veins, where the vessel diameter is much larger than the size of an RBC (6 - 8 μm) (*27*), whole blood can be approximated as a bulk fluid. For the microvessels considered in this study, the size of an RBC is a significant fraction of the vessel diameter. This leads to deviations from the parabolic flow profile expected for laminar flow of a Newtonian fluid (*12*), which is governed by Hagen-Poiseuille's Law. In particular, blunting of the flow profile (i.e. exponent greater than two) is expected in smaller vessels or in low-flow vessels, where RBCs tend to aggregate (*12*). The degree of blunting we observed in both arterioles ($k = 3.3 \pm 1.1$) and venules ($k = 3.7 \pm 1.5$) (**Fig. 4.5D**) compare well with previous measurements of 2.4 - 4 for rabbit mesenteric arterioles (*28*). For surface arterioles, the blunting of the spatial profile is more pronounced during the diastolic phase in both our study (**Fig. 4.5D**) and in previous work (*12*), likely due to increased RBCs aggregation at lower shear rate (*28*).

Diverging and converging flow profiles

Previous studies have investigated blood flow at bifurcations of large arteries, which have fast flow speed and high Reynolds number (*43*). In microcirculatory systems, detailed in vivo measurements of time and space dependent blood flow profiles at vessel junctions have not been made for vessels smaller than 2-mm diameter. In this study, we resolved the spatial flow profile at bifurcations and mergers of cortical surface arterioles and venules, respectively, and observed a double-peaked profile at the junction (**Fig. 4.6B** and **6D**). Interestingly, the flow profile of the two branches immediately downstream from an arteriole bifurcation displayed flow speed maxima that were skewed toward the outer edge of the bifurcation. This asymmetric flow profile is consistent with low Reynolds flow that is dominated by viscous forces, and is skewed in the opposite direction that is found in bifurcations of larger vessels with faster flow speeds, such as the carotid bifurcation (*43*). After about one vessel diameter away from the junction, the spatial flow profiles shifted so the maximum speed was once again at the vessel center.

Blood flow speed modulation due to respiration

Breath inhalation was found to cause a transient decrease in centerline RBC flow speed in both cortical arterioles and venules (**Fig. 4.7**). The effect of breathing on blood flow speed has previously been examined in the vena cava, pulmonary artery and vein, and aorta in dogs (*44, 45*) and humans (*33*). During inspiration, the

diaphragm movement creates a negative pressure in the thoracic cavity allowing lung expansion, and thus an increase in the total vascular volume of the lung. This causes a decrease in pulmonary return to the heart, which leads to a decrease in systemic blood pressure (*45*), although other studies have disagreed (*33, 44*). The transient flow speed decrease we observe in both surface arterioles and venules is consistent with such a decrease in systemic blood pressure during inhalation.

Comparison to other cerebral blood flow measurement modalities

Most current approaches for measuring cerebral hemodynamics focus on quantification of regional changes in blood flow and do not resolve flow dynamics in individual microvessels. Clinical tools include magnetic resonance imaging (MRI) approaches, such as blood oxygen level dependent (BOLD) MRI (*46*) and arterial spin labeling (*47*), as well as positron emission tomography (*46, 48*). These techniques are well suited to the measurement of regional changes of blood flow in the brain of humans and animals models with a spatial resolution of about a millimeter to a centimeter (*46-48*). Laser Doppler spectroscopy (*48*), intrinsic optical imaging (*49*), and laser speckle contrast imaging (*50*) enable millimeter or better resolution mapping of flow changes in animal models, but still cannot resolve dynamics in individual microvessels. Doppler optical coherence tomography has recently emerged as an approach to mapping cerebral blood flow in many diving and ascending vessels simultaneously, but still cannot resolve flow in individual capillaries (*16*). Transcranial Doppler ultrasonography enables measurement of detailed blood flow

information including pulsatile flow due to each heartbeat (*48*), but is unable to resolve blood flow in vessels smaller than the middle cerebral artery. It is optical microscopies that provide the necessary spatial and temporal resolution to quantify flow dynamics in vessels as small as capillaries. However, standard techniques such as confocal microscopy are limited in depth penetration by optical scattering (*51*). In vivo 2PEF microscopy overcomes some of these limitations and has allowed in vivo imaging of vascular topology and blood flow in murine brain to a depth of 1 mm (*21*). This technique relies on nonlinear excitation of fluorescent molecules by tightly focused, infrared wavelength, femtosecond-duration laser pulses to restrict fluorescence emission to the focal volume, which is scanned in three-dimensions to form an image. With this tool, it is possible to image fluorescently-labeled objects with micrometer resolution deep in the brain tissue of live, anesthetized rodents without damaging the tissue (*52, 53*). When the blood plasma is labeled with an intravenously-injected fluorescent dye, this imaging method enables in vivo mapping of vascular architecture and, by directly tracking the motion of unlabeled RBCs, quantification of flow speed in individual vascular segments (*17, 20*). This flow measurement technique, however, is able to quantify only the motion of RBCs, not of blood plasma. As a result, we are unable to characterize differences in average speed, or in temporal or spatial flow profiles, for blood plasma versus RBCs.

CONCLUSIONS

We have shown that 2PEF microscopy, together with EKG and respiratory waveform recordings, enables cerebral blood flow dynamics to be quantified with high spatial and temporal resolution and high flow speed precision in individual cerebral microvessels. The detailed information on cerebral hemodynamics obtained in this study and the experimental approach we developed has many applications. Because disruption of blood flow in small cerebral vessels is associated with cognitive decline and dementia (*5*), our measurements of hemodynamics in cortical arterioles, capillaries, and venules can serve as a foundation for studies of altered brain blood flow in pathological conditions. Our discovery of pulsatile blood flow in brain capillaries is also of importance. Loss of pulsatile flow leads to increases in systematic vascular resistance and may cause tissue damage (*8*), while in pulmonary capillaries pulsatile blood flow is essential for efficient oxygen transfer (*8*). Pulsatility may similarly be important for brain capillary function and neural tissue health. The interval between heartbeat and the time of maximum flow speed is an indicator of vascular health. Clinically, increases in pulse wave velocity are used to diagnose arterial stiffening (e.g. due to atherosclerosis), which is a contributing factor to cognitive decline and dementia (*3*). In addition, changes in the microcirculation that contribute to the central nervous system damage that results from chronic hypertension may depend, in part, on the abnormal transmission of highly pulsatile blood pressure into the microvascular networks of the brain (and other highly perfused organs with low vascular resistance) (*5*). Our experimental approach allows these important hemodynamic phenomena to be investigated in murine brain vasculature. When

combined with transgenic animals, this approach may allow in-depth studies of the role of microvascular dysfunction in a variety of brain diseases, including Alzheimer's disease and vascular dementia. Previous work has found that endothelial cells experiencing low shear or turbulent flow become seed sites for the formation of atherosclerotic plaques, and that such flow disturbances are common at arterial bifurcations (*54*) . Our method to quantify flow profiles in individual microvessels and at microvascular junctions could enable investigation of potentially pathogenic flow in these small diameter vessels. The ability to carefully quantify these blood flow dynamics, as well investigate how hemodynamics may change in pathological conditions, provides a new window on normal and disease-state cerebral microcirculation.

REFERENCES

1. P. Blinder, A. Y. Shih, C. Rafie, D. Kleinfeld, Topological basis for the robust distribution of blood to rodent neocortex. *Proc Natl Acad Sci USA* **107**, 12670 (Jul 13, 2010).
2. S. Lorthois, F. Cassot, F. Lauwers, Simulation study of brain blood flow regulation by intra-cortical arterioles in an anatomically accurate large human vascular network: Part I: Methodology and baseline flow. *NeuroImage* **54**, 1031 (Jan 15, 2011).
3. G. F. Mitchell *et al.*, Arterial stiffness, pressure and flow pulsatility and brain structure and function: the Age, Gene/Environment Susceptibility - Reykjavik Study. *Brain* **134**, 3398 (Nov 1, 2011).
4. K. Cruickshank *et al.*, Aortic pulse-wave velocity and its relationship to mortality in diabetes and glucose intolerance: an integrated index of vascular function? *Circulation* **106**, 2085 (Oct 15, 2002).
5. J. O'Brien, Vascular cognitive impairment. *Am J Geriatr Psychiatry* **14**, 724 (Sep 1, 2006).
6. K. Heinicke *et al.*, Excessive erythrocytosis in adult mice overexpressing erythropoietin leads to hepatic, renal, neuronal, and muscular degeneration. *Am J Physiol Regul Integr Comp Physiol* **291**, R947 (Oct 1, 2006).
7. L. Pantoni, Cerebral small vessel disease: from pathogenesis and clinical characteristics to therapeutic challenges. *Lancet Neurol* **9**, 689 (Jul 1, 2010).

8. H. Wilkens, W. Regelson, F. S. Hoffmeister, The physiolgic importance of pulsatile blood flow. *N Engl J Med* **267**, 443 (Aug 30, 1962).

9. B. W. Zweifach, H. H. Lipowsky, Quantitative studies of microcirculatory structure and function. III. Microvascular hemodynamics of cat mesentery and rabbit omentum. *Circ Res* **41**, 380 (Sep 1, 1977).

10. A. Pries, K. Ley, M. Claassen, P. Gaehtgens, Red cell distribution at microvascular bifurcations. *Microvasc Res* **38**, 81 (Jul 1, 1989).

11. D. Audet, W. Olbricht, The motion of model cells at capillary bifurcations. *Microvasc Res* **33**, 377 (May 1, 1987).

12. A. S. Popel, P. C. Johnson, Microcirculation and Hemorheology. *Annual review of fluid mechanics* **37**, 43 (Jan 1, 2005).

13. J. F. Gross, M. Intaglietta, B. W. Zweifach, Network model of pulsatile hemodynamics in the microcirculation of the rabbit omentum. *Am J Physiol* **226**, 1117 (May 1, 1974).

14. G. W. Schmid-Schönbein, S. Y. Lee, D. Sutton, Dynamic viscous flow in distensible vessels of skeletal muscle microcirculation: application to pressure and flow transients. *Biorheology* **26**, 215 (Jan 1, 1989).

15. W. Rosenblum, Erythrocyte velocity and a velocity pulse in minute blood vessels on the surface of the mouse brain. *Circ Res* **24**, 887 (Jun 1, 1969).

16. V. J. Srinivasan *et al.*, Optical coherence tomography for the quantitative study of cerebrovascular physiology. *J Cereb Blood Flow Metab*, (Mar 2, 2011).

17. D. Kleinfeld, P. Mitra, F. Helmchen, W. Denk, Fluctuations and stimulus-induced changes in blood flow observed in individual capillaries in layers 2

through 4 of rat neocortex. *Proc Natl Acad Sci U S A* **95**, 15741 (Dec 22, 1998).

18. N. Nishimura, N. L. Rosidi, C. Iadecola, C. B. Schaffer, Limitations of collateral flow after occlusion of a single cortical penetrating arteriole. *J Cereb Blood Flow Metab* **30**, 1914 (Dec 1, 2010).

19. N. Nishimura *et al.*, Targeted insult to subsurface cortical blood vessels using ultrashort laser pulses: three models of stroke. *Nat Methods* **3**, 99 (Feb 1, 2006).

20. C. Schaffer *et al.*, Two-photon imaging of cortical surface microvessels reveals a robust redistribution in blood flow after vascular occlusion. *PLoS Biol* **4**, e22 (Feb 1, 2006).

21. D. Kobat *et al.*, Deep tissue multiphoton microscopy using longer wavelength excitation. *Opt Express* **17**, 13354 (Aug 3, 2009).

22. D. Kleinfeld, K. R. Delaney, Distributed representation of vibrissa movement in the upper layers of somatosensory cortex revealed with voltage-sensitive dyes. *J Comp Neurol* **375**, 89 (Nov 4, 1996).

23. B. Neu, R. Wenby, H. J. Meiselman, Effects of Dextran Molecular Weight on Red Blood Cell Aggregation. *Biophysical Journal* **95**, 3059 (Sep 15, 2008).

24. Q. Nguyen, P. Tsai, D. Kleinfeld, MPScope: a versatile software suite for multiphoton microscopy. *J Neurosci Methods* **156**, 351 (Sep 30, 2006).

25. P. Drew, P. Blinder, G. Cauwenberghs, A. Shih, D. Kleinfeld, Rapid determination of particle velocity from space-time images using the Radon transform. *J Comput Neurosci*, (May 21, 2009).

26. A. A. Constantinescu, H. Vink, J. A. Spaan, Elevated capillary tube hematocrit reflects degradation of endothelial cell glycocalyx by oxidized LDL. *Am J Physiol Heart Circ Physiol* **280**, H1051 (Mar 1, 2001).

27. C. M. Hawkey, P. M. Bennett, S. C. Gascoyne, M. G. Hart, J. K. Kirkwood, Erythrocyte size, number and haemoglobin content in vertebrates. *Br J Haematol* **77**, 392 (Mar 1, 1991).

28. G. Tangelder *et al.*, Velocity profiles of blood platelets and red blood cells flowing in arterioles of the rabbit mesentery. *Circ Res* **59**, 505 (Nov 1, 1986).

29. J. Cuzick, A Wilcoxon-type test for trend. *Stat Med* **4**, 87 (Jan 1, 1985).

30. J. Nguyen, N. Nishimura, R. N. Fetcho, C. Iadecola, C. B. Schaffer, Occlusion of cortical ascending venules causes blood flow decreases, reversals in flow direction, and vessel dilation in upstream capillaries. *J Cereb Blood Flow Metab* **31**, 2243 (Nov 1, 2011).

31. W. Seed, N. Wood, Velocity patterns in the aorta. *Cardiovasc Res* **5**, 319 (Jul 1, 1971).

32. C. Mills *et al.*, Pressure-flow relationships and vascular impedance in man. *Cardiovasc Res* **4**, 405 (Oct 1, 1970).

33. L. Wexler, D. Bergel, I. Gabe, G. Makin, C. Mills, Velocity of blood flow in normal human venae cavae. *Circ Res* **23**, 349 (Sep 1, 1968).

34. A. G. Salotto, L. F. Muscarella, J. Melbin, J. K. Li, A. Noordergraaf, Pressure pulse transmission into vascular beds. *Microvasc Res* **32**, 152 (Sep 1, 1986).

35. G. Schmid-Schonbein, Biomechanics of microcirculatory blood perfusion. *Annu Rev Biomed Eng* **1**, 73 (1999).

36. P. Tsai *et al.*, Correlations of neuronal and microvascular densities in murine cortex revealed by direct counting and colocalization of nuclei and vessels. *J Neurosci* **29**, 14553 (Nov 18, 2009).

37. A. R. Pries, D. Neuhaus, P. Gaehtgens, Blood viscosity in tube flow: dependence on diameter and hematocrit. *Am J Physiol* **263**, H1770 (Dec 1, 1992).

38. U. Windberger, A. Bartholovitsch, R. Plasenzotti, K. J. Korak, G. Heinze, Whole blood viscosity, plasma viscosity and erythrocyte aggregation in nine mammalian species: reference values and comparison of data. *Exp Physiol* **88**, 431 (May 1, 2003).

39. A. C. H. Guyton, J E, *Textbook of Medical Physiology*. (Saunders, ed. 11, 2005).

40. T. C. Skalak, G. W. Schmid-Schonbein, Viscoelastic properties of microvessels in rat spinotrapezius muscle. *J Biomech Eng* **108**, 193 (Aug 1, 1986).

41. L. H. Smaje, P. A. Fraser, G. Clough, The distensibility of single capillaries and venules in the cat mesentery. *Microvasc Res* **20**, 358 (Nov 1, 1980).

42. M. Intaglietta, D. R. Richardson, W. R. Tompkins, Blood pressure, flow, and elastic properties in microvessels of cat omentum. *Am J Physiol* **221**, 922 (Sep 1, 1971).

43. M. Motomiya, T. Karino, Flow patterns in the human carotid artery bifurcation. *Stroke* **15**, 50 (Jan 1, 1984).

44. W. G. Guntheroth, B. C. Morgan, G. L. Mullins, Effect of respiration on venous return and stroke volume in cardiac tamponade. Mechanism of pulsus parodoxus. *Circ Res* **20**, 381 (Apr 1, 1967).

45. B. Morgan, D. Dillard, W. Guntheroth, Effect of cardiac and respiratory cycle on pulmonary vein flow, pressure, and diameter. *J Appl Physiol* **21**, 1276 (Jul 1, 1966).

46. D. P. Bulte *et al.*, Quantitative measurement of cerebral physiology using respiratory-calibrated MRI. *NeuroImage*, (Dec 22, 2011).

47. R. B. Buxton, L. R. Frank, A model for the coupling between cerebral blood flow and oxygen metabolism during neural stimulation. *J Cereb Blood Flow Metab* **17**, 64 (Jan 1, 1997).

48. W. Heiss, M. Forsting, H. Diener, Imaging in cerebrovascular disease. *Curr Opin Neurol* **14**, 67 (Feb 1, 2001).

49. D. Y. Ts'o, R. D. Frostig, E. E. Lieke, A. GRINVALD, Functional organization of primate visual cortex revealed by high resolution optical imaging. *Science* **249**, 417 (Jul 27, 1990).

50. D. A. Boas, A. K. Dunn, Laser speckle contrast imaging in biomedical optics. *J Biomed Opt* **15**, 011109 (Jan 1, 2010).

51. L. Nyman *et al.*, Real-time, multidimensional in vivo imaging used to investigate blood flow in mouse pancreatic islets. *J Clin Invest* **118**, 3790 (Nov 1, 2008).

52. W. Denk, J. Strickler, W. Webb, Two-photon laser scanning fluorescence microscopy. *Science* **248**, 73 (Apr 6, 1990).

53. W. Zipfel, R. Williams, W. Webb, Nonlinear magic: multiphoton microscopy in the biosciences. *Nat Biotechnol* **21**, 1369 (Nov 1, 2003).

54. C. Hahn, M. A. Schwartz, The role of cellular adaptation to mechanical forces in atherosclerosis. *Arteriosclerosis, Thrombosis, and Vascular Biology* **28**, 2101 (Dec 1, 2008).

CHAPTER 5

IN VIVO TWO-PHOTON IMAGING OF CEREBRAL MICROCIRCULATION IN ANIMAL MODELS OF ESSENTIAL THROMBOCYTHEMIA AND POLYCYTHEMIA VERA: PLATELET AND LEUKOCYTE CONTRIBUTIONS TO CORTICAL MICROVASCULAR DYSFUNCTION

Thom P. Santisakultarm[1], Claire Q. Paduano[1], Jane Y. Lee[1], Teresa L. Southard[2], Tracy Stokol[3], Nozomi Nishimura[1], William L. Olbricht[1,4], Richard T. Silver[5], Andrew I. Schafer[5], Chris B. Schaffer[1]

[1]Department of Biomedical Engineering, Cornell University, Ithaca, NY 14853

[2]Department of Biomedical Sciences, Cornell University, Ithaca, NY 14853

[3]Department of Population Medicine and Diagnostic Center, Cornell University, Ithaca, NY 14853

[4]Department of Chemical and Biomolecular Engineering, Cornell University, Ithaca, NY 14853

[5]Department of Medicine, Weill Cornell Medical College, New York, NY 10065

This research is a manuscript, which will be submitted to a peer-reviewed journal

ABSTRACT

Essential thrombocythemia (ET) and polycythemia vera (PV) are among the myeloproliferative neoplasms (MPNs), a group of disorders that exhibit bone marrow hyperactivity. Both ET and PV share a common $JAK2^{V617F}$ mutation in hematopoietic cells, leading to excessive production of platelets in ET, and red blood cells (RBCs), leukocytes, and platelets in PV. The additional blood cells alter rheology and lead to prominent coagulation problem of large vessels in ET and PV. Although evidence suggests cerebral microcirculation problems in these conditions as well, direct observations of microvessel thrombosis or flow problems have not been made. Because disruption to cortical circulation is linked to cognitive decline and dementia, we utilized *in vivo* two-photon excited fluorescence (2PEF) microscopy to examine cerebral microcirculation of $JAK2^{V617F}$ MPN transgenic mice that mimic the phenotypes of ET and PV. As much as 40% of cortical capillaries in MPN models had no blood flow. In mice with erythrocytosis, the proportion of stalled capillaries increased as hematocrit increased. In ET mice, neither hematocrit, leukocyte, nor platelet counts influenced the rate of capillary stalling. In both MPN models, leukocytes and platelets played a major role in adhering to the endothelium and plugging the microvascular flow. They persisted and chronically obstructed blood flow in individual vessels for over 2 hours in some cases. Aspirin did not resolve the microocclusions. Our study suggests cerebral microvascular circulation problems may be a prominent feature of clinical ET and PV.

INTRODUCTION

Essential thrombocythemia (ET) and polycythemia vera (PV) are two of the four myeloproliferative neoplasms (MPNs), the others being myelofibrosis and chronic myelogenous leukemia. These diseases exhibit hyperactivity of the bone marrow, resulting in an increase in the formed elements of the blood(1). A mutation in JAK2, a cytoplasmic tyrosine kinase in the signal transducers and activators of transcription (STAT) signaling pathway, was discovered as a common mutation in MPNs. ET and PV display the most significant amount of this $JAK2^{V617F}$ mutant allele burden among MPNs, with 95% and 60% of patients having mutant protein in hematopoietic stem cells, respectively(2). Normally, STAT molecules are phosphorylated by activated JAK2 only after binding of a signaling molecule such as erythropoietin or thrombopoietin. Phosphorylated STAT then translocates to the nucleus, promoting production of blood cells. With mutant $JAK2^{V617F}$, however, STAT phosphorylation is constitutively turned on, regardless of an extracellular signal presence, leading to the excess hematopoiesis in MPNs(2). Higher levels of $JAK2^{V617F}$ in transgenic mice and human patients has resulted in a PV phenotype, which exhibits increases in red blood cells (RBCs), leukocytes, and platelets. On the other hand, lower levels of the mutant gene are found in ET, which shows primarily excessive platelet production(3).

Both ET and PV display a number of secondary clinical conditions related to blood circulation and coagulation problems. In fact, various types of venous, arterial, and microvascular thrombosis are the most common causes of morbidity and

mortality(4). In PV, excess RBCs contributes to high viscosity that increases flow resistance(5), and elevated leukocyte counts may also exacerbate flow problems, especially in the microvessels where leukocytes must squeeze through vessels and contribute significantly to resistance. In both disorders, elevated platelet counts may alter lead to increased thrombosis. In the brain, decreased blood flow and vascular thrombosis can have devastating consequences. Occlusion of large vessels is a common complication of ET and PV that leads to transient ischemic attacks and cerebral infarcts(6, 7). Small vessel occlusions are also plausible. Although they may not produce acute clinical symptoms, and hence go unnoticed; micro-occlusive events may have an important impact on neuronal health. Small stroke is associated with cognitive decline and development of dementia such as Alzheimer's disease and vascular dementia(8). Indeed, clinical case studies have linked cognitive problems to ET and PV, suggesting neurological effects in these diseases(9-12).

However, because of the lack of robust animal models of MPNs until recently, no clear causative link between ET and PV and neural health has been made, and the role of elevated hematocrit, leukocytes, and platelets on cerebral microvascular flow remains largely unexplored. In order to quantify the effects of PV and ET on the brain, we examined vascular structure and cerebral blood flow in MPN mouse models using two-photon excited fluorescence microscopy (2PEF), which enables micrometer-resolution, three-dimensional imaging deep into the brain tissue. We examined wildtype, erythropoietin-injected (Epo-inj), and ET and PV mouse models. In order to create ET and PV mouse models with $JAK2^{V617F}$ mutation only in the hematopoietic

cells, we transplanted the bone marrow cells of transgenic donors with ubiquitous mutated JAK2 into wildtype recipients. Strikingly, we found a high incidence of stalled blood flow in individual capillary segments in both ET and PV mouse models. In PV animals, the number of stalled microvessels increased with increasing hematocrit, although leukocytes and platelets were frequently identified as the cause of the blockages. We found marked upregulation of intercellular adhesion molecule (ICAM)-1, both *in vivo* and *ex vivo*, which may have led to leukocyte and platelet activation and adhesion to the cerebral vasculature. In the PV models, but not in ET, we found evidence of compromised blood brain barrier. Vessel diameter, volume, and RBC flow speed were examined and found to be modestly altered in PV and ET.

MATERIALS AND METHODS

Animal Models

Five experimental groups of animals were utilized in this study: wildtype (wt), bone marrow transplanted (BMT) wt, Epo-inj wildtype, BMT ET, and BMT PV. All mice were on C57/Bl6 background. The Epo-inj group received 0.5 mL of erythropoietin (20 - 200 IU/mL) subcutaneously for 5 consecutive days to induce erythrocytosis. This group served as the secondary polycythemia model. Both BMT ET and BMT PV groups were derived from mutant $JAK2^{V617F}$ mice, kindly provided by Dr. Radek Skoda(*3*). These transgenic mice were generated using nine copies of the human $JAK2^{V617F}$ gene with the sequences placed in the inverse orientation and flanked by antiparallel loxP sites. MxCre transgene was crossed into the mouse line in order to control FF1 gene activation. These mice were used as bone marrow transplantation donors in order to create mice where the $JAK2^{V617F}$ mutation is only present in the hematopoietic stem cells, rather than in all cells. Induction of the transgene in BMT ET and BMT PV groups made use of interferon-inducible MxCre. By administering polyinosine-polycytosine (pIpC, 0.3 mL of 1 mg/mL) intraperitoneally, Cre recombinase excise, reorient the transgene, and initiate the constitutive production of additional blood cells. We delivered pIpC in one of the two ways: to the donor prior to BMT to obtain recipients with all same phenotype (either ET or PV), or to BMT recipient mice after they have recovered from the irradiation. Within 8 to 12 weeks after $JAK2^{V617F}$ has been activated, mice with spun hematocrit above 55% were classified as PV; those with platelets above 1,000 thou/μL but without elevation of

RBCs were considered ET. Mice that did not exhibit the classical symptoms of ET and PV were excluded from this study. To control for the effects of bone marrow transplantation procedure to subjects' physiology, we created an experimental group where lethally irradiated wildtype mice received normal bone marrow cells from another wildtype control donor. Characteristics of subjects are summarized in **Table 5.1**.

Table 5.1. Characteristics of study subjects

	wt and BMT wt	BMT ET	Epo-inj	BMT PV
Subjects (n)	35	16	19	14
Male/Female	29/6	13/3	9/10	4/10
Age (months)	4.7 (0.4 - 7.6)	5.2 (4 - 12.6)	4.5 (0.8 - 19.7)	5.4 (4.1- 6.5)
Weight (g)	26 (20 - 36)	27 (20 - 33)	24 (18 - 28)*	23 (19 - 28)*
Hematocrit (%)**	46 (38 - 52)	46 (39 - 50)	61 (40 - 71)*	67 (54 - 91)*
Hemoglobin (g/dL)	15.6 (14.1 - 17.2)	16.3 (13.3 - 18.7)	21.1 (19.7 - 21.5)	24.3 (15.2 - 30.7)*
Red blood cells (mil/µL)	10.5 (9.2 - 11.6)	11.1 (7.4 - 13.7)	14.4 (13.9 - 14.9)*	14.9 (10.1 - 18.4)*
Leukocytes (thou/µL)	5.0 (3.1 - 10.2)	10.7 (5.8 - 71.8)	3.5 (1.5 - 9.6)	8.3 (7.6 - 35.0)
Platelets (thou/µL)	882 (787 - 1007)	6226 (1340 - 8019)*	574 (154 - 850)	531 (109 - 1190)

Values are expressed as median (range)

*$p < 0.05$ vs. control group (one-way ANOVA with multiple comparisons and Tukey-Kramer method)

**Packed cell volume

Bone Marrow Transplantation

Recipients were irradiated with 5-Gy gamma ray twice at one-hour interval. Donors received a pentobarbital (intraperitoneal, 12 mg per 100-g rodent) overdose. Bone marrow cells were harvested from their femurs, resuspended in phosphate buffered saline (PBS) and retroorbitally administered to recipient mice. The transplantation was performed with the donor:recipients ratio of 1:8 to ensure that each recipient received at least 2 million bone marrow cells. The recipients were allowed to rest and recover for at least 5 weeks after the procedure.

Surgical Preparation

We follow the surgical procedures previously published(*13*). A total of 55 male and 29 female adults (mean ± standard deviations, 5.3±2.5 months-old), 18 - 36 g in mass were used in this study. Subjects were anesthetized with 2% isoflurane and maintained at 1 - 2.5% at 37.5 °C body temperature with a heating blanket (model 50-7053P; Harvard Apparatus) throughout the experiment. Mice received glycopyrrolate (0.05 mg per 100-g rodent) intramuscularly to facilitate respiration. Bupivacaine (0.1 mL, 0.125% w/v) was subcutaneously administered as a local anesthesia before initial incision and preparation of a 5-mm craniotomy over the parietal cortex. A glass cover (Deckglaser; World Precision Instruments) was glued to the skull using cyanoacrylate (model name; Loctite®) and dental cement (Lang Dental Mfg. Co. & Co-Oral-Ite Dental Mfg. Co.), and the space between the exposed brain and the cover glass slip was filled with artificial cerebrospinal fluid. For acute experiments, subjects were supplemented with 5% (w/v) glucose in physiological saline (0.5 mL per 100-g

rodent) hourly throughout the experiment. For chronic experiments, animals received dexamethesone (0.02 mg per 100-g rodent) intramuscularly to suppress inflammatory response. Subjects received analgesic ketofen (0.2 mg per 100-g rodent) daily or as needed for 3 days and were allowed to recover. The care and experimental manipulation of our animals have been reviewed and approved by the Institutional Animal Care and Use Committee at Cornell University.

Fluorescent Labeling

Texas red dextran (0.05 mL of 2.5% w/v, D1830; Invitrogen) and Rhodamine 6G (0.05 mL of 0.1% w/v) in saline was injected retroorbitally. The Texas red dextran labels the blood plasma, allowing imaging of vascular topology and quantification of blood flow by tracking the motion of non-labeled red blood cells. The lipophilic Rhodamine 6G labels both white blood cells and platelets with very high efficiency(*14*). In some experiments, Hoechst 33342 (0.05 mL of 0.5% w/v, H1399; Invitrogen) was also intravenously administered to label nuclei of blood cells (i.e. leukocytes).

In Vivo Two-photon Excited Fluorescence Imaging

Cerebral vasculature was imaged using a custom-built 2PEF microscope with 800-nm, 87-MHz, 100-fs pulses from a Ti:sapphire laser oscillator (MIRA HP pumped by a Verdi-V18; Coherent, Inc.) or 1040-nm, 1-MHz, 300-fs pulses from a Yb-fiber chirped pulse amplifier (FCPA μJewel D-400; IMRA America, Inc.). The fluorescence collected from the sample was split by a 600-nm long-pass dichroic into

photomultiplier tubes for dual channel imaging of multiple wavelengths. The excitation signal was relayed through filters 460/50, 575/25, and 645/65 nm (center/bandwidth), for Hoechst 33342, Rhodamine 6G, and Texas Red imaging, respectively. Laser scanning and data acquisition was controlled by MPSCOPE(*15*) or ScanImage(*16*). A 4x air objective (Olympus) with a 0.28 numerical aperture (NA) was used for low magnification images of the cranial window. For high magnification imaging of RBC flow speed, vessel diameter, and stall vessel measurements, we used a 0.95-NA, 20x water immersion objective (Olympus).

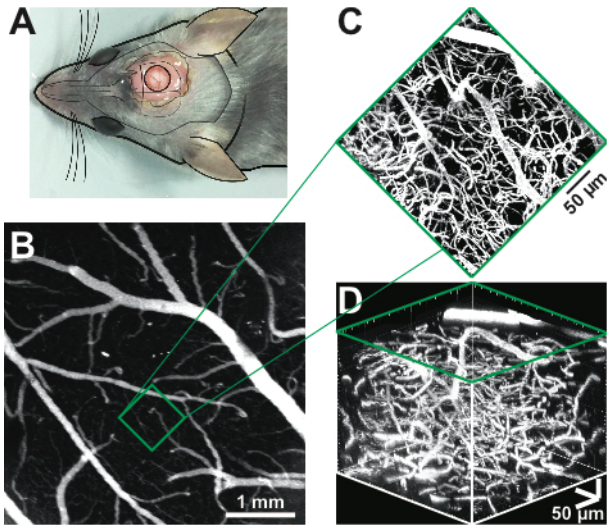

Figure 5.1. In vivo 2PEF imaging of cortical microvessels
(A) Schematic drawing of a cranial window to allow optical access to the brain of an anesthetized rodent. (B) Low (4x air objective, NA = 0.28, Olympus) and (C) high (20x water immersion objective, NA = 0.95, Olympus) magnification images of fluorescently labeled brain vasculature. The images were obtained using a custom-built 2PEF microscopy, and axially projected using ImageJ (National Institutes of Health). (D) Three-dimensional rendering (Imaris; Bitplane Scientific) of the vasculature beneath (C).

Stalled Vessels Evaluation

Multiple, high-resolution, overlapping 200 x 200 μm stacks with 1-μm axial spacing up to 350 μm in cortical depth were recorded, then aligned in three-dimensions by maximizing the cross-correlation signals in the overlapping regions to obtain vascular topology. Each capillary segment in the combined image volume was manually scored to be flowing or stalled, while keeping track of the total capillary number for vascular density per brain volume calculation. Vascular segments with blood cell movement over 1-s of recording were classed as flowing; while others were classed as stalled. This measurement only identifies vessels with no moving blood cells, as we cannot determine motion of plasma. Stalled capillaries were categorized as associated with platelets if immobile platelets, which contain Rhodamine 6G signal, were present within the segment. Stalled capillaries with stationary leukocytes, distinguished by colocalization of both Rhodamine 6G and Hoechst33342 signals, were denoted as associated to leukocytes. Stalled capillaries without leukocytes or platelets were classed as empty or RBCs if stationary RBCs are present. In some animals, only Texas red dextran and Rhodamine 6G were present. Platelets and leukocytes, both labeled by Rhodamine 6G, can still be distinguished based on their appearance. Leukocytes are larger and show solid fluorescence throughout the cell where as platelets are much smaller and tend to sporadically aggregate along vessel walls and present a more punctate appearance. The capillaries plugged by leukocytes or platelets were monitored over the next ~2 hours by examining subsequent image stacks acquired at 15, 30, 60, and 120 minutes later at the same region. We determined

whether initially blocked vessels by leukocytes or platelets did or did not reestablish flow over time.

RBC Flow Speed and Vascular Diameter

We measured blood flow speed and diameter of surface vessels and their connecting microvessels up to 10 branches away. To measure RBC velocity, we repetitively scan single vessels along their central axis at a line rate of 1.7 kHz to track RBC position over at least 30 s. The obtained space-time images contain diagonal dark streaks of the RBC movement over time where the slope is inversely proportional to its speed(*13, 17, 18*). To determine vessel diameter, images of individual vessels were recorded while stepping from above to below the vessel. Once axially projected, diameters were calculated by manual selection of a cross-sectional line perpendicular to the vascular segment. The intensity profile along the selected line was plotted, and the diameter was taken to be the distance over which the intensity exceeds 20% of maximum intensity value(*13*).

Blood and Bone Marrow Evaluation

Subjects were euthanized with pentobarbital (intraperitoneal, 12 mg per 100-g rodent) after imaging session, and a minimum of 0.2 mL of whole blood sample was drawn into an ethylenediaminetetraacetic acid (EDTA, 0.15 mL of 6.7 mg/mL) prefilled syringe by cardiocentesis. The sample was transferred to an EDTA dried-spray blood collection tube (367842; Becton Dickinson) in order to obtain the

complete blood count (Advia 2120; Siemens). Blood smears were made and manually evaluated.

Subjects were fixed in 4% paraformaldehyde. The femurs were isolated for bone marrow examination, and the brain was kept for immunohistochemical staining. Anatomical necropsy was performed on the preserved body to confirm physiological manifestation of MPNs (e.g. splenomegaly, hepatomegaly, myeloid hyperplasia, fibrosis).

RESULTS

Micro-occlusive events in mouse models of MPNs

To study how brain vasculature and blood flow is altered in MPN, we prepared glass-covered craniotomies in mouse models of PV and ET, and then used 2PEF imaging of intravenously-injected fluorescent dye to acquire three-dimensional image stacks of the cortical vasculature (**Figure 5.1**). Because the dye labels only the blood plasma, and not RBCs, we were able to manually score each capillary in the image stack as flowing or stalled, based on the whether RBC motion was observed over the ~4 frames (~1 s) that each capillary was visible in the image stack (**Figure 5.2A**).

In wildtype animals and in wild type animals that received bone marrow transplant from a wildtype animal, we found that the vast majority of brain capillaries were flowing, with only a small fraction stalled (mean ± standard error of the mean (SEM), 3±0.6%, 5,167 vessels, n = 17). In contrast, we found a marked elevation in the number of stalled capillaries in mice with mutant JAK2 in hematopoietic cells that exhibited an ET phenotype (16±5%, 4,692 vessels, n = 8), and an even more dramatic elevation in capillary stalls in both the Epo-injection model of erythrocytosis (19±4%, 5,840 vessels, n = 15) and in animals with mutant JAK2 that exhibit a PV phenotype (28±5%, 8,959 vessels, n = 11) (**Figure 5.2B**). There was no significant difference between wt and BMT wt groups (**S Figure 5.1**) or between sexes (**S Figure 5.2**)

In addition, we found the large variability in the fraction of brain capillaries stalled in both models with excessive erythrocytosis to depend strongly on the hematocrit of the animal (**Figure 5.2C**). In the ET animals, the fraction of stalled capillaries did not appear to depend on hematocrit (**Figure 5.2C**), platelet, nor leukocyte counts (**S Figure 5.3**).

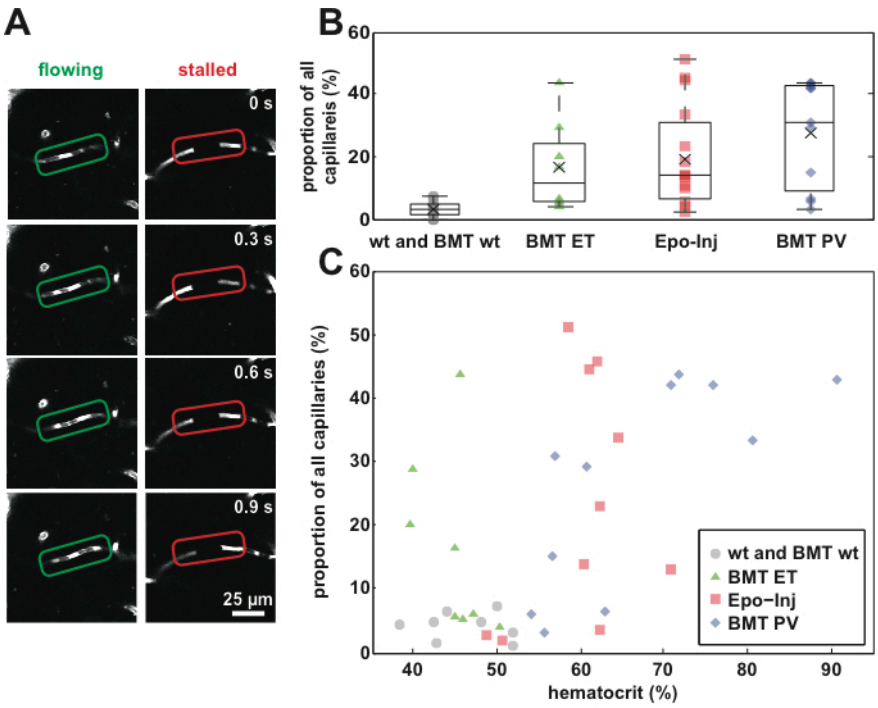

Figure 5.2. Elevated capillary occlusions ("stalls") in mouse models of MPNs
(A) Sequential 2PEF images that demonstrate flowing (left panels) and stalled (right panels) vessels in the cerebral cortex captured every 0.3 s for a total of 1 s. Texas Red dextran was administered to label blood plasma (bright), leaving the cellular components unlabeled (dark). (B) Fraction of capillaries with no RBC flow in wt and BMT wt, BMT ET, Epo-inj, and BMT PV animals. (C) The fraction of capillary stalls increases with increasing hematocrit in Epo-inj and BMT PV animals. The fraction of capillaries stalled in BMT ET group was not dependent on hematocrit.

Leukocytes and platelet aggregation obstruct microvascular flow in PV and ET models, while RBCs block capillaries in PV

To identify the cellular basis for these stalled capillaries, we developed a strategy to distinguish between several potential causes: adhered leukocytes, micro-thrombi, just stagnant RBCs, or a vessel filled with blood plasma and no flowing RBCs (**Figure 5.3A**). Leukocytes contribution to total capillary stalls were highest in BMT PV (5%), followed by Epo-inj (2%), BMT ET (2%), and wt and BMT wt (1%), respectively. Platelet stalls also displayed a similar trend with BMT PV being the highest (7%), followed by Epo-inj (4%), BMT ET (2%), and wt and BMT wt (1%). Both experimental groups with erythrocytosis showed a profound proportion of capillaries stalled with only stagnant RBCs (13% and 12% for Epo-inj and BMT PV, respectively), compared to animals with normal hematocrit (3% for both BMT ET and wt and BMT wt). The rest of the stalled vessels were empty of blood cells (2, 4, 7, and 4% in wt and BMT wt, BMT ET, Epo-inj, and BMT PV, respectively) (**Figure 5.3B**; wt and BMT wt: 4,061 vessels, n = 11. BMT ET: 3,451 vessels, n = 6. Epo-inj: 4,640 vessels, n = 8. BMT PV: 6,005 vessels, n = 9). Proportion of stall types among only stalled vessels (as oppose to all capillaries) is also available in **S Figure 5.5**.

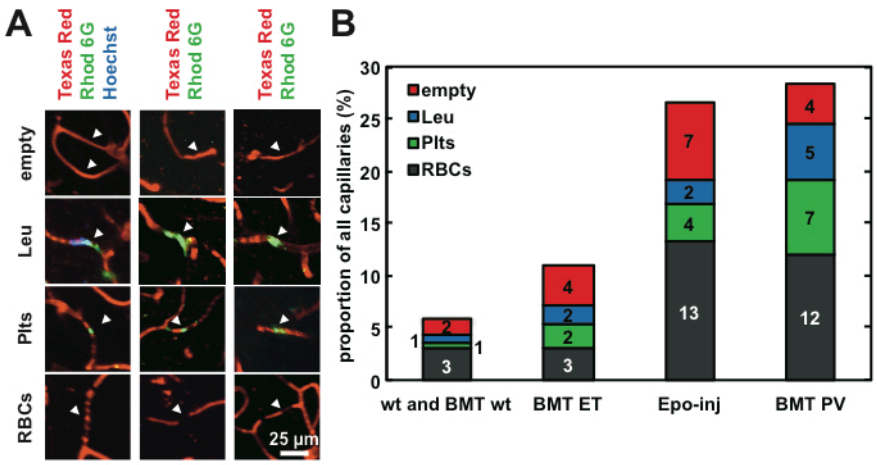

Figure 5.3. Microvascular stalls in PV and ET are associated with leukocytes and platelet aggregates and, in PV models, with RBC plugs

(A) Four classes of microvascular stalls are distinguished: platelets, leukocytes, only RBCs, or empty. Texas Red dextran labeled blood plasma (red), Rhodamine 6G labeled leukocytes and platelets (green), while Hoechst33342 bound to nuclei (blue). Leukocytes and platelets have distinct morphologies that can be differentiated from one another even with the lack of Hoechst33342 dye. RBCs were unlabeled and appeared dark against the labeled blood plasma in each vessel. (B) Composition of stall causes in wt and BMT wt, BMT ET, Epo-inj, and BMT PV.

Estimation of leukocyte and platelet stalls lifetimes

We monitored each capillary stalled due to a leukocyte or platelet aggregate. Over the same region of interest, image stacks were acquired at approximately 15, 30, 60, and 120 mins after the first time point. We quantified the fraction of microvessels where leukocytes and platelets remained in place. **Figure 5.4** shows the proportion of persistent leukocyte (**Figure 5.4A**) and platelet (**Figure 5.4B**) stalls, each fitted to an exponential decay. The mean lifetimes of leukocyte plugs were longest in BMT ET (15 mins; 81 stalls, n = 7) and BMT PV (7 mins; 24 stalls, n = 5), compared to only 2 mins for Epo-inj (53 stalls, n = 7) (**Figure 5.4A**). Platelet stalls reestablish flow quickly in BMT ET (2 mins; 110 stalls, n = 5), but 20% that did not resolve and remained in place for over 2 hours. In Epo-inj (95 stalls, n = 7) and BMT PV (99 stalls, n =7), platelet aggregates persisted longer, for 12 and 42 mins, respectively.

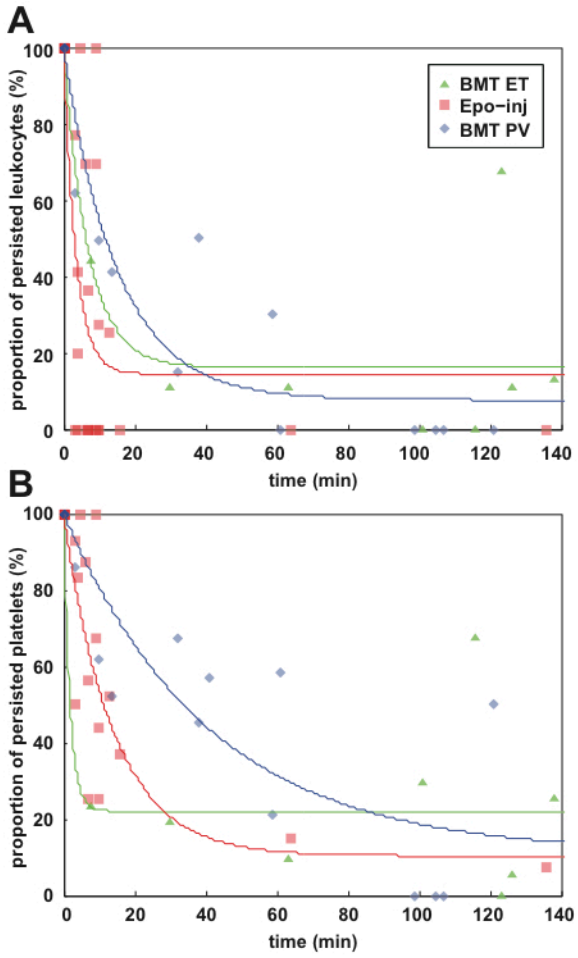

Figure 5.4. Leukocyte and platelet plugs in cortical capillaries are long-lived
Individual microvascular stalls associated with leukocytes and platelets were monitored. Proportion of persistant (A) leukocytes and (B) platelet aggregates decay over time. The mean lifetime of leukocytes and platelets were longest in BMT PV compared to BMT ET and Epo-inj animals. After 2 hours, approximately 80% of these stalls have reestablished flow.

Quantification of average RBC flow speed

Positions of RBCs in flowing blood vessels were tracked over at least 30 s by repetitive line scanning along the centerline of vascular lumen (**Figure 5.5E**). Centerline RBC flow speeds of surface arterioles significantly decreased by 30% in Epo-inj (mean ± SEM, 3.9±0.04 mm/s, 72 vessels, n = 12) and 52% in BMT PV (2.7±0.07 mm/s, 29 vessels, n = 7), respectively, when compared to wt and BMT wt (5.6±0.03 mm/s, 126 vessels, n = 26; one-way ANOVA with multiple comparisons using Tukey-Kramer's method, p = 0.00001). Surface arteriole RBC flow speed in BMT ET group did not change significantly (5.3±0.6 mm/s, 41 vessels, n = 7) (**Figure 5.5F**). For capillaries, RBC flow speed significantly slowed by 24% in BMT PV (0.63±0.04 mm/s, 77 vessels, n = 7) when compared to wt and BMT wt (0.83±0.04 mm/s, 149 vessels, n = 18; p = 0.0002), while BMT ET (0.78±0.03 mm/s, 92 vessels, n = 6) and Epo-inj (0.85±0.03 mm/s, 76 vessels, n = 12) groups were not statistically different (**Figure 5.5G**). Lastly, no statistical difference (p = 0.23) in the mean centerline RBC flow speeds of surface venules between wt and BMT wt (1.58±0.10 mm/s, 141 vessels, n = 27), BMT ET (1.70±0.24 mm/s, 40 vessels, n = 6), Epo-inj (1.72±0.13 mm/s, 106 vessels, n = 12), or BMT PV (1.14±0.22 mm/s, 25 vessels, n = 7) groups was found (**Figure 5.5H**).

Average vascular diameter

We measured diameter of surface arteriole, cortical capillaries, and surface venules (**Figure 5.5A**). There was no significant difference in diameters of surface

arterioles for the BMT ET (15.6±1.9 μm, 51 vessels, n = 9), Epo-inj (21.2±1.6 μm, 70 vessels, n = 12), or BMT PV (20.5±2.4 μm, 31 vessels, n = 7) groups when compared to wt and BMT wt (20.5±1.2 μm, 120 vessels, n = 26) (one-way ANOVA with multiple comparisons using Tukey-Kramer method, p = 0.52) (**Figure 5.5B**). Capillary diameter of BMT PV (5.3±0.1 μm, 96 vessels, n = 7) was significantly larger than those of BMT ET (4.8±0.1 μm, 118 vessels, n = 8) and Epo-inj (4.6±0.1 μm, 110 vessels, n = 12), but not wt and BMT wt (4.9±0.1 μm, 180 vessels, n = 18, p = 0.0005) (**Figure 5.5C**). Diameter of surface venules in Epo-inj group (34.0±3.2 μm, 111 vessels, n = 12) was larger than wt and BMT wt group (22.1±1.9 μm, 134 vessels, n = 27, p = 0.01) (**Figure 5.5D**).

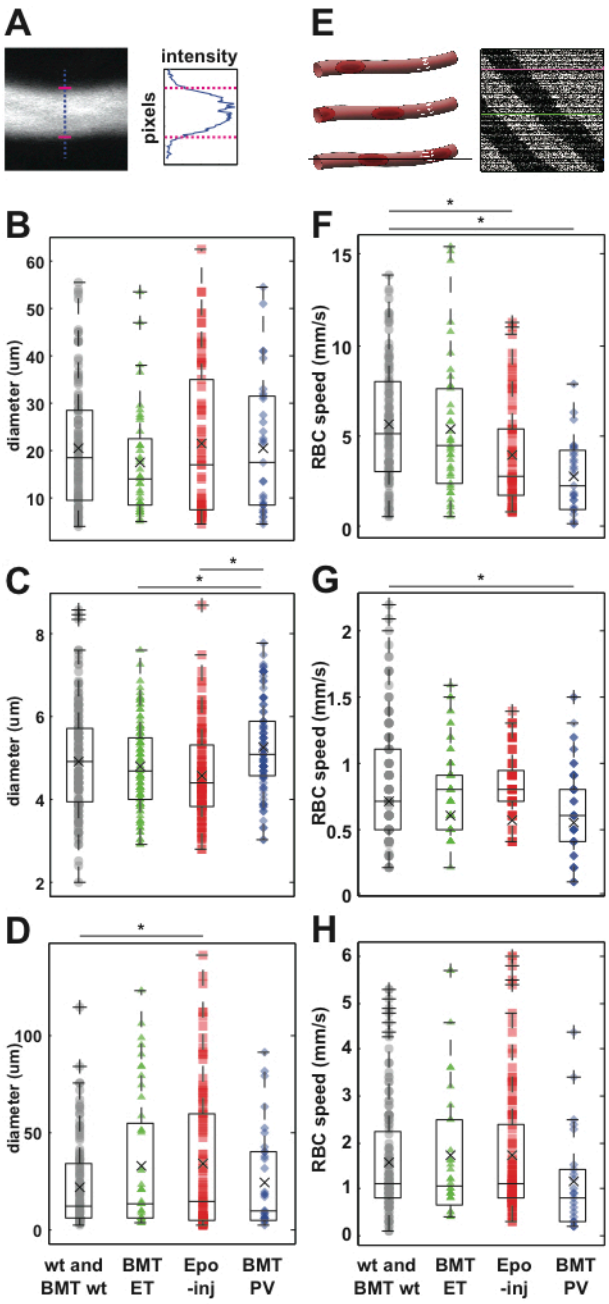

Figure 5.5. Diameter and speed of microvessels in MPNs
(A) Axially projected images of a single microvessel and its intensity profile along the drawn line. Diameter was taken to be the distance over which the intensity exceeds 20% of maximum intensity value. Diameter of surface arterioles (B), capillaries (C), and venules (D). (E) Schematic drawing of linescan acquisition to track RBC positions over time and obtain blood flow velocity in individual blood vessels. Speed of surface arterioles (F), cortical capillaries (G), and surface venules (H).

Quantification of capillary density

Capillary density in wt and BMT wt (mean ± standard deviation, 8,937±1,492 vessels/mm^3), BMT ET (8,030±727 vessels/mm^3), Epo-inj (9,897±3,073 vessels/mm^3), and BMT PV (8,890±1,615 vessels/mm^3) were not statistically different from one another (one-way ANOVA with multiple comparisons using Tukey-Kramer method, $p = 0.48$).

DISCUSSION

We quantified the proportion of stalled capillaries in the brain of MPN mouse models and found an elevation in microvessels with no flow (**Figure 5.2**). In brain surface vessels, all larger than ~7 μm, no flow blockage was observed, although large thrombosis (e.g. deep vein thrombosis(*19*), heart attack(*20*), and stroke(*21*)) is a known complication in humans with MPNs. Our study showed the first direct observation of cerebral microvessel thrombosis in live animal models of MPNs. The chronic micro-occlusions of cortical vascular network are a potential cause of small strokes. They can disturb efficient transport of nutrition, waste, and oxygen, which is detrimental to neural health. Studies have also shown that small strokes are associated with neurological degeneration and cognitive decline(*8*). This may explain neurological symptoms such as depression(*9*), mixed movement disorder(*10*), amnesia, headache, and dysphagia(*11*) displayed in ET and PV patients. Stroke and cerebral embolism are also prevalent in both ET(*12*) and PV(*7*)—observations that are also consistent with ours.

Further, we identified leukocyte and platelets to be associated with a large proportion of overall stalled blood vessels. In PV, this overactivation is related to high hematocrit(*22*) (**Figure 5.2**), which leads to enhanced cellular interactions due to red cell mass expansion(*23, 24*). High hematocrit also results in high viscosity and shear rate on the vessel wall, leading to endothelial dysfunction(*24, 25*). Our finding demonstrated leukocyte activation and tight adherence to damaged endothelium that plugged capillary blood flow.

On the other hand, the factors that influence thrombotic risks in ET are less clear in previous studies as well as in ours (**Figure 5.2C and S Figure 5.3**). The degree of thrombocytosis did not correlate with thrombosis in our study, and was found to be an inconsistent variable associated with thrombosis in others(*25, 26*). Leukocytosis, however, was shown by many clinical studies to increase thrombotic risk and is an independent predictor of leukemic transformation in ET(*27, 28*). Nevertheless, because platelet cytoreduction therapy seems to reduce thrombotic frequency in high-risk ET patients, there is a belief among physicians that normal platelet count is preferable. Regardless of the explanation, leukocytes and platelets activation in both ET and PV have been observed *in vitro* and *in vivo*(*29*). CD11b, an antigen that mediates adhesion during inflammation, is overexpress, thus leading to greater capacity for phagocytosis as well as increased production of reactive oxygen species(*30*). In ET, the percentage of platelets expressing P-selectin is increased in patients with a history of thrombosis compared to those without. ET patients are also more likely to have an increase in E-selectin and circulating microparticles, produced by platelets, which amplify thrombogenesis(*31, 32*). Furthermore, prothrombin fragment, thrombomodulin, and von Willebrand factor were found to be elevated in both PV and ET. Platelet and leukocyte activation results in an increase in circulating platelet-leukocyte complexes, which is reported to correlate with neutrophil degranulation, stabilization of fibrinogen, and higher extracellular tissue factor content(*33, 34*). Thus, prothrombotic flow environment is constituted and greatly affected microcirculation(*32, 35, 36*).

For blood vessels with flowing RBCs, there is an overall trend for slower flow speed in the animal models of MPNs, with severity most pronounced in high hematocrit Epo-inj and BMT PV animals (**Figure 5.5**). On average, diameter of arterioles, capillaries, and venules were not largely different. Vascular density also did not change significantly when compared to wt and BMT wt. In combination with the proportion of stalled capillaries and the decrease in flow speed in the still-flowing vessels, we approximate the decrease in capillary bed perfusion to be 30, 17, and 34% in BMT ET, Epo-inj, and BMT PV, respectively compared to controls. While this flow reduction is not likely to cause an explicit stroke, such chronic hypoperfusion due to, for example carotid artery stenosis, has been linked to accelerated cognitive decline(*38-40*). Thus, microthrombotic events in MPNs may have detrimental impact to neural function in the long term.

We have demonstrated impaired cerebral blood flow in the brain of MPN mouse models using 2PEF microscopy. In PV models, elevated capillary stalls strongly correlated with increased hematocrit. Therefore, hematocrit level must be carefully controlled to minimize small strokes. In ET, however, further studies are required to identify the critical factors that lead to thrombotic complications in the microvessels. In both disorders, leukocytes, platelets, and endothelium were activated and played a major role in disturbance to normal brain blood flow. Careful assessment

of cognitive functions and novel targeted therapy to decrease stalls would be beneficial to decrease neurological problems in MPN patients.

SUPPLEMENTARY FIGURES

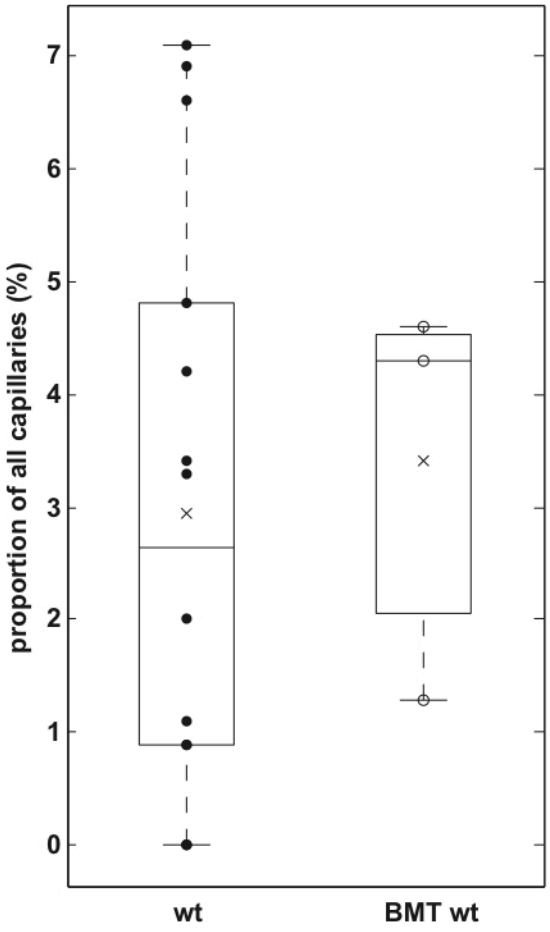

Supplementary Figure 5.1. Capillary stalls in wt and BMT wt animals are comparable
There was no statistically significant difference between the proportion of stalled capillaries in wt and BMT wt groups.

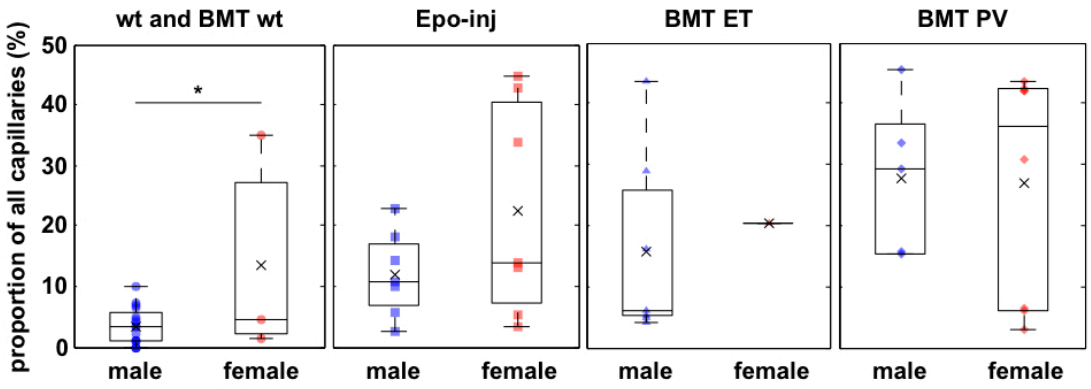

Supplementary Figure 5.2. Capillary stalls comparisons between male and females

The rates of capillary stalls are not statistically significant except in the case of wt and BMT wt males and females

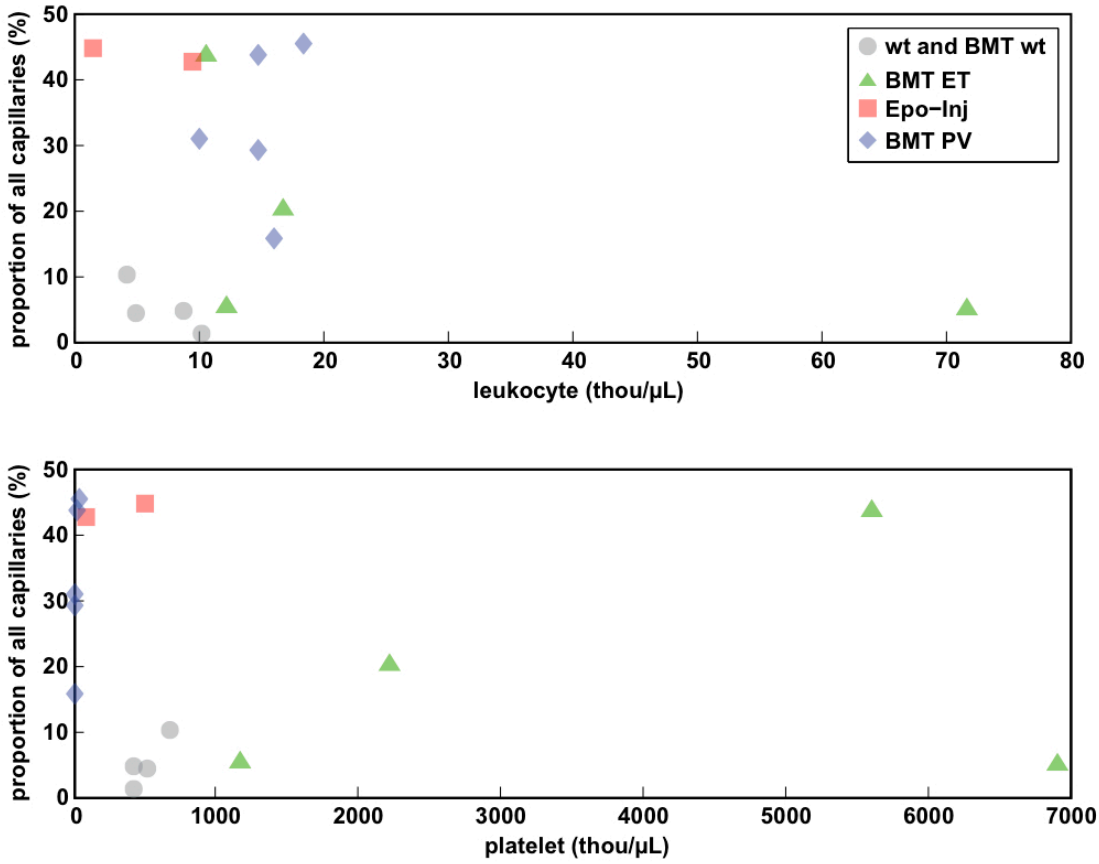

Supplementary Figure 5.3. Proportion of stalled capillaries as a function of leukocyte and platelet counts

Leukocytes and platelet counts did not correlate to the stall rate of wt and BMT wt, BMT ET, Epo-inj, nor BMT PV

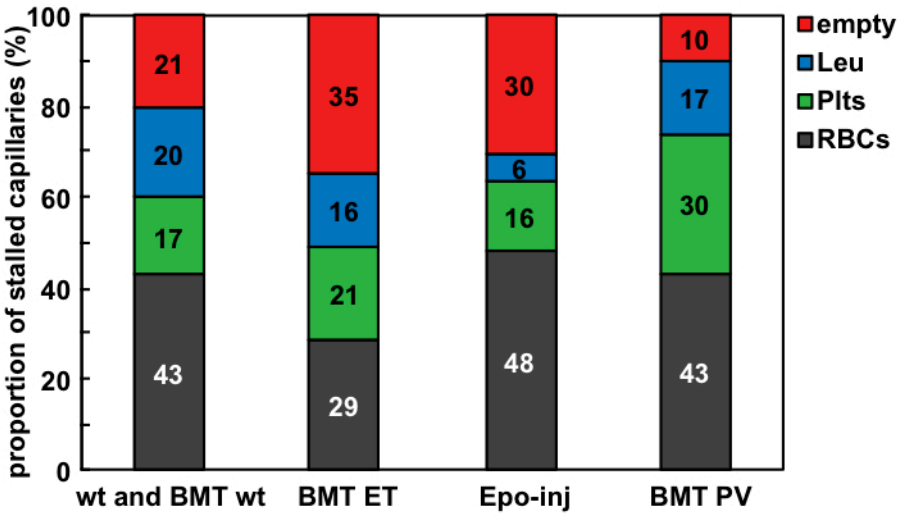

Supplementary Figure 5.4. Stall compositions by causes
Stall compositions were shown by stall types: empty, leukocyte, platelet, or RBC plugs.

REFERENCES

1. A. Tefferi, The history of myeloproliferative disorders: before and after Dameshek. *Leukemia*, (Sep 20, 2007).
2. K. Morgan, D. Gilliland, A Role for JAK2 Mutations in Myeloproliferative Diseases. *Annu Rev Med*, (Oct 5, 2007).
3. R. Tiedt *et al.*, Ratio of mutant JAK2-V617F to wild-type Jak2 determines the MPD phenotypes in transgenic mice. *Blood* **111**, 3931 (Apr 15, 2008).
4. J. L. Spivak *et al.*, Chronic myeloproliferative disorders. *Hematology Am Soc Hematol Educ Program*, 200 (Jan 1, 2003).
5. J. Wood, K. DBJr, Hemorheology of the cerebral circulation in stroke. **16**, 765 (Sep 1, 1985).
6. H. Kurabayashi, A. Hishinuma, R. Uchida, S. Makita, M. Majima, Delayed manifestation and slow progression of cerebral infarction caused by polycythemia rubra vera. *Am J Med Sci* **333**, 317 (May 1, 2007).
7. T. Segura, J. Serena, J. Teruel, A. Davalos, Cerebral embolism in a patient with polycythemia rubra vera. *Eur J Neurol* **7**, 87 (Jan 1, 2000).
8. J. O'Brien, Vascular cognitive impairment. *Am J Geriatr Psychiatry* **14**, 724 (Sep 1, 2006).
9. C. Fones, W. F. Tsoi, Polycythaemia rubra vera presenting with depression: recognising the syndrome abulia. *Br J Clin Pract* **49**, 97 (Jan 1, 1995).

10. M. Bauer, Absolutely therapy-resistant depression and mixed movement disorder in an unusual case of polycythemia vera. *Pharmacopsychiatry* **28**, 66 (Mar 1, 1995).

11. J. Kondlapudi, R. J. O'Connor, S. Mawer, Cerebral haemorrhage as the presenting feature of myeloproliferative disorder. *BMJ Case Rep* **2009**, (Jan 1, 2009).

12. S. Richard, J. Perrin, P.-A. Baillot, J.-C. Lacour, X. Ducrocq, Ischaemic stroke and essential thrombocythemia: a series of 14 cases. *Eur J Neurol* **18**, 995 (Jul 1, 2011).

13. T. P. Santisakultarm *et al.*, In Vivo Two-photon Excited Fluorescence Microscopy Reveals Cardiac- and Respiration-Dependent Pulsatile Blood Flow in Cortical Blood Vessels in Mice. *Am J Physiol Heart Circ Physiol*, (Jan 20, 2012).

14. H. Baatz, M. Steinbauer, A. Harris, F. Krombach, Kinetics of white blood cell staining by intravascular administration of rhodamine 6G. *Int J Microcirc Clin Exp* **15**, 85 (Mar 1, 1995).

15. Q. Nguyen, P. Tsai, D. Kleinfeld, MPScope: a versatile software suite for multiphoton microscopy. *J Neurosci Methods* **156**, 351 (Sep 30, 2006).

16. T. A. Pologruto, B. L. Sabatini, K. Svoboda, ScanImage: flexible software for operating laser scanning microscopes. *Biomed Eng Online* **2**, 13 (May 17, 2003).

17. C. B. Schaffer *et al.*, Two-photon imaging of cortical surface microvessels reveals a robust redistribution in blood flow after vascular occlusion. *PLoS Biol* **4**, e22 (Feb 1, 2006).

18. D. Kleinfeld, P. Mitra, F. Helmchen, W. Denk, Fluctuations and stimulus-induced changes in blood flow observed in individual capillaries in layers 2 through 4 of rat neocortex. *Proc Natl Acad Sci U S A* **95**, 15741 (Dec 22, 1998).

19. H. Reikvam, R. V. Tiu, Venous thromboembolism in patients with essential thrombocythemia and polycythemia vera. *Leukemia* **26**, 563 (Apr 1, 2012).

20. A. Cucuianu *et al.*, Arterial stenosis and atherothrombotic events in polycythemia vera and essential thrombocythemia. *Rom J Intern Med* **44**, 397 (Jan 1, 2006).

21. I. L. H. Knottnerus, H. Ten Cate, J. Lodder, F. Kessels, R. J. van Oostenbrugge, Endothelial dysfunction in lacunar stroke: a systematic review. *Cerebrovasc Dis* **27**, 519 (Jan 1, 2009).

22. H. Kwaan, J. Wang, Hyperviscosity in polycythemia vera and other red cell abnormalities. *Semin Thromb Hemost* **29**, 451 (Oct 1, 2003).

23. S. Austin, J. Lambert, The JAK2 V617F mutation and thrombosis. *Br J Haematol* **143**, 307 (Nov 1, 2008).

24. J. Spivak, Daily aspirin--only half the answer. *N Engl J Med* **350**, 99 (Jan 8, 2004).

25. A. Carobbio *et al.*, Risk factors for arterial and venous thrombosis in WHO-defined essential thrombocythemia: an international study of 891 patients. *Blood* **117**, 5857 (Jun 2, 2011).

26. A. Tefferi, Platelet count in essential thrombocythemia: the more the better? *Blood* **112**, 3526 (Oct 15, 2008).

27. T. Barbui, A. Carobbio, A. Rambaldi, G. Finazzi, Perspectives on thrombosis in essential thrombocythemia and polycythemia vera: is leukocytosis a causative factor? *Blood*, 1 (Apr 16, 2009).

28. N. Gangat *et al.*, Leucocytosis in polycythaemia vera predicts both inferior survival and leukaemic transformation. *Br J Haematol* **138**, 354 (Aug 1, 2007).

29. M. Karakantza *et al.*, Markers of endothelial and in vivo platelet activation in patients with essential thrombocythemia and polycythemia vera. *Int J Hematol* **79**, 253 (Apr 1, 2004).

30. C. Burgaleta, N. González, J. César, Increased CD11/CD18 expression and altered metabolic activity on polymorphonuclear leukocytes from patients with polycythemia vera and essential thrombocythemia. *Acta Haematol* **108**, 23 (Jan 1, 2002).

31. A. Belotti *et al.*, Circulating endothelial cells and endothelial activation in essential thrombocythemia: results from CD146+ immunomagnetic enrichment--flow cytometry and soluble E-selectin detection. *Am J Hematol* **87**, 319 (Mar 1, 2012).

32. J. Duchemin *et al.*, Increased circulating procoagulant activity and thrombin generation in patients with myeloproliferative neoplasms. *Thromb Res* **126**, 238 (Sep 1, 2010).

33. E. Arellano-Rodrigo *et al.*, Increased platelet and leukocyte activation as contributing mechanisms for thrombosis in essential thrombocythemia and correlation with the JAK2 mutational status. *Haematologica* **91**, 169 (Feb 1, 2006).

34. A. Falanga, M. Marchetti, A. Vignoli, D. Balducci, T. Barbui, Leukocyte-platelet interaction in patients with essential thrombocythemia and polycythemia vera. *Exp Hematol* **33**, 523 (May 1, 2005).

35. A. Falanga *et al.*, Polymorphonuclear leukocyte activation and hemostasis in patients with essential thrombocythemia and polycythemia vera. *Blood* **96**, 4261 (Dec 15, 2000).

36. E. Shantsila, P. W. Kamphuisen, G. Y. H. Lip, Circulating microparticles in cardiovascular disease: implications for atherogenesis and atherothrombosis. *J Thromb Haemost* **8**, 2358 (Nov 1, 2010).

37. T. Saigusa *et al.*, A case of essential thrombocytosis developing nephrotic syndrome and severe endothelial damage. *J Nephrol* **19**, 656 (Jan 1, 2006).

38. R. S. Marshall, R. M. Lazar, Pumps, Aqueducts, and Drought Management: Vascular Physiology in Vascular Cognitive Impairment. *Stroke* **42**, 221 (Jan 1, 2011).

39. M. Chmayssani, J. R. Festa, R. S. Marshall, Chronic ischemia and neurocognition. *Neuroimaging Clin N Am* **17**, 313 (Aug 1, 2007).

40. K.-A. Hossmann, Pathophysiology and therapy of experimental stroke. *Cell Mol Neurobiol* **26**, 1057 (Jan 1, 2006).

41. A. Tefferi, W. Vainchenker, Myeloproliferative neoplasms: molecular pathophysiology, essential clinical understanding, and treatment strategies. *J Clin Oncol* **29**, 573 (Feb 10, 2011).

42. R. Landolfi *et al.*, Efficacy and safety of low-dose aspirin in polycythemia vera. *N Engl J Med* **350**, 114 (Jan 8, 2004).

CHAPTER 6

CEREBRAL BLOOD FLOW ABNORMALITIES IN ANIMAL MODELS OF SICKLE CELL DISEASE

PATHOPHYSIOLOGY OF SICKLE CELL DISEASE

Sickle cell disease (SCD) is a group of heritable hemoglobinopathies resulting most often in sickle hemoglobin (HbS) (**Table 6.1**). About 50,000 Americans are affected by SCD, and it is estimated that 2 million more are carriers for the trait. SCD affects primarily those of African descent, with 8-10% of the African American population being carriers (*1*). Even higher frequencies are found in African populations, particularly in equatorial regions. The high frequency of carriers is thought to be due to the heterozygous advantage the gene confers to malaria infection.

In HbS, a single point mutation of the 17^{th} nucleotide leads to the substitution of valine for glutamine in the β-globin chain. This substitution causes the β1 and β2 chains of two hemoglobin molecules to crystallize when the HbS tetramer is deoxygenated, so that deoxygenated HbS polymerizes into fibers which disturb the normal morphology of red blood cells (RBCs) causes them to "sickle" into a characteristic crescent-shape (**Fig. 6.1**). As RBCs enter the microvasculature, they gradually become deoxygenated and increasingly rigid and sickled. This increases blood viscosity, increases shear rate, hence reducing flow speed through individual microvessels. The increased transit time leads to further deoxygenation that reduces deformability of the cells, resulting in blockages of microcirculation (**Fig. 6.2**). The most common variant of SCD is sickle cell anemia (SCA), in which patients are homozygous for the β-globin mutation (genotype $\beta^S\beta^S$). SCA is characterized by chronic hemolytic anemia and vaso-occlusive crisis leading to progressive tissue damage in highly vascularized organs including the liver, kidney, brain, and lungs (*1*).

	Characteristics
Severe sickle-cell disease	
HbS/S (β6Glu>Val/β6Glu>Val); sickle-cell anaemia	The most common form of sickle-cell disease
HbS/β^0 thalassaemia	Most prevalent in the eastern Mediterranean region and India[14]
Severe HbS/β^+ thalassaemia	Most prevalent in the eastern Mediterranean region and India; 1–5% HbA present[14]
HbS/OArab (β6Glu>Val/β121Glu>Lys)	Reported in north Africa, the Middle East, and the Balkans; relatively rare[14]
HbS/D Punjab (β6Glu>Val/β121Glu>Gln)	Predominant in northern India but occurs worldwide[14]
HbS/C Harlem (β6Glu>Val/β6Glu>Val/β, β73Asp>Asn)	Electrophoretically resembles HbSC, but clinically severe; double mutation in β-globin gene; very rare[15]
HbC/S Antilles (β6Glu>Lys/β6Glu>Val, β23Val–Ile)	Double mutation in β-globin gene results in severe sickle-cell disease when co-inherited with HbC; very rare[16]
HbS/Quebec-CHORI (β6Glu>Val/β87Thr>Ile)	Two cases described; resembles sickle-cell trait with standard analytical techniques[17]
Moderate sickle-cell disease	
HbS/C (β6Glu>Val/β6Glu>Lys)	25–30% cases of sickle-cell disease in populations of African origin[13]
Moderate HbS/β^+ thalassaemia	Most cases in the eastern Mediterranean region; 6–15% HbA present[14]
HbA/S Oman (β^A/β6Glu>Val, β121Glu>Lys)	Dominant form of sickle-cell disease caused by double mutation in β-globin gene; very rare[18]
Mild sickle-cell disease	
Mild HbS/β^{++} thalassaemia	Mostly in populations of African origin; 16–30% HbA present[14]
HbS/E (β6Glu>Val/β26Glu>Lys)	HbE predominates in southeast Asia and so HbSE uncommon, although frequency is increasing with population migration[19]
HbA/Jamaica Plain (β^A/β6Glu>Val, β68Leu/Phe)	Dominant form of sickle-cell disease; double mutation results in Hb with low oxygen affinity; one case described[20]
Very mild sickle-cell disease	
HbS/HPFH	Group of disorders caused by large deletions of the β-globin gene complex; typically 30% fetal haemoglobin[14]
HbS/other Hb variants	HbS is co-inherited with many other Hb variants, and symptoms develop only in extreme hypoxia

Genotypes that have been reported to cause sickle-cell disease are listed. All include at least one copy of the β^S allele, in combination with one or more mutations in the β-globin gene. HbS=sickle haemoglobin. HbA=haemoglobin variant A. HbE=haemoglobin variant E. Hb=haemoglobin.

Table 2: **Different types of sickle-cell disease**

Table 6.1: Different types of SCD (*1*)

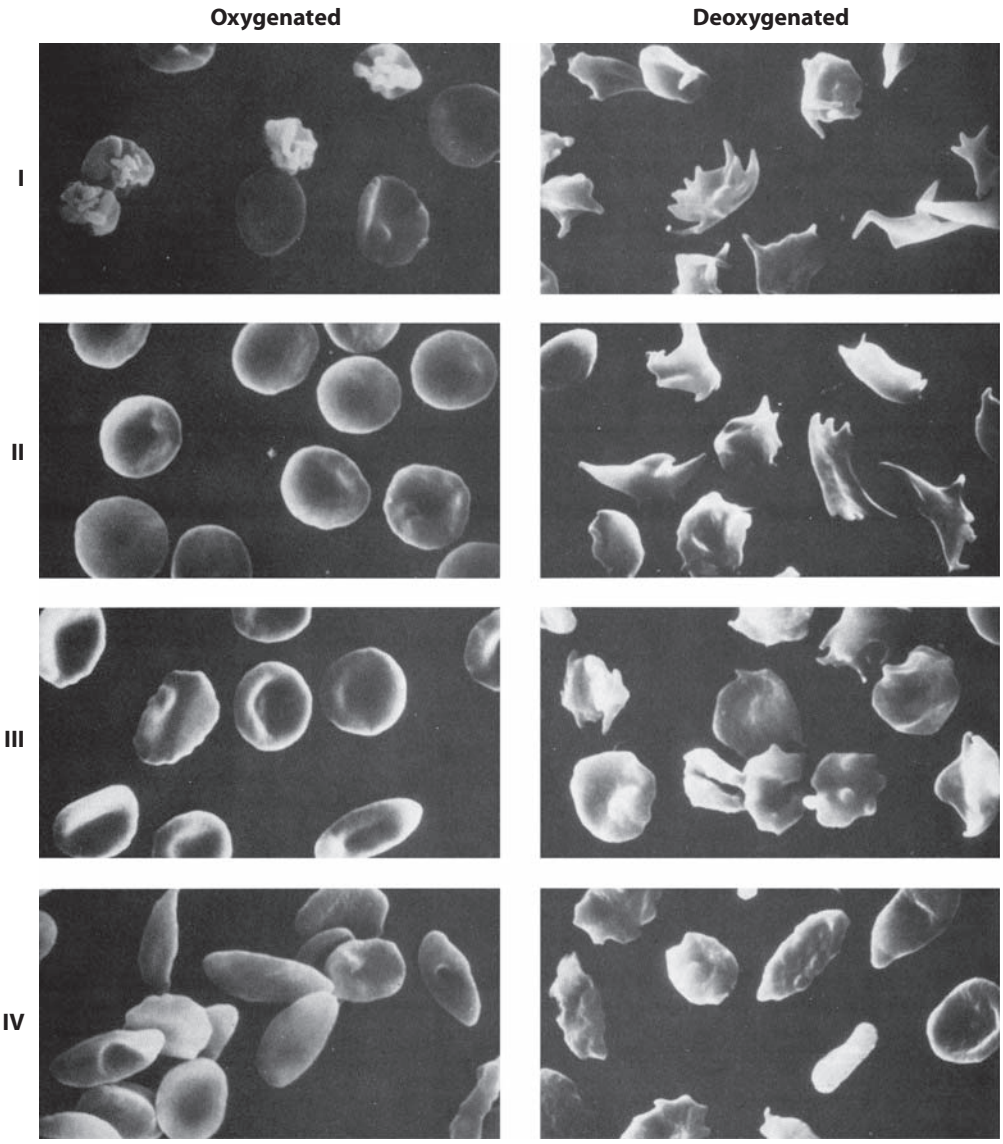

Figure 6.1: Sickle RBCs
Four subpopulations of sickle RBCs: (I) reticulocytes, (II) discocytes, (III) dense discocytes, and (IV) irreversibly sickled cells under oxygenated and deoxygenated conditions (*2*).

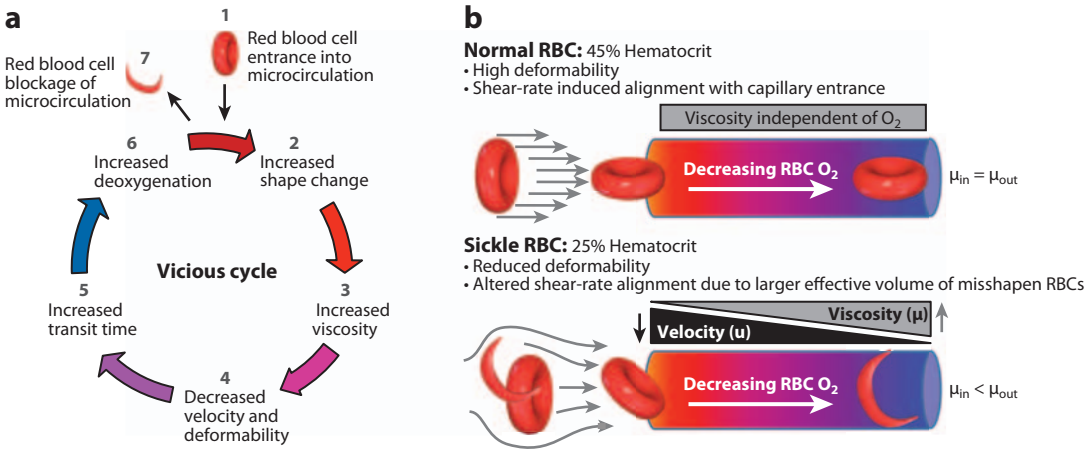

Figure 6.2: Vicious Cycle Exacerbates Damage of RBCs in Microvasculature
(a) Schematic of the cycle. (b) Normal RBCs traverse capillaries with high deformity and see no changes in viscosity. Sickle RBCs, however, increase their viscosity as they deoxygenate, which changes their shape and enter them into vicious cycle (*3*).

COMPLICATIONS

Stroke is the leading cause of death in SCA. Stroke has mainly been documented in patients with SCA, rather than in other variants of SCD, with a frequency of 6% in patients of all ages. There is a 67% incidence of reoccurrence of stroke, with 60% of these occurring within 36 months following the initial stroke (*1, 4*). The chance for the first stroke occurring by 20 years of age was reported to be 11%, rising to 24% by 45 years of age (*5*). In patients under 20 years of age, as well as for those over 30 years of age, the majority of strokes are infarcts and do not result in death. On the other hand, in patients 20-29 years of age the majority of strokes are hemorrhagic. The mechanisms driving these changing risk profiles remain unclear. Most deaths caused by stroke are identified as hemorrhagic (*5*). The high risk for stroke, combined with high rate of reoccurrence and mortality, makes risk factors and treatment of stroke obvious areas of study in SCA. Multiple factors may play into risk for stroke, as while infants less than 2 years of age seem to be protected from stroke, exhibiting the lowest incidence of all age groups, children ages 1 through 9 years of age have a higher risk of stroke than those ages 10 through 19 (*1*). Some risk factors that have been suggested to result in cerebrovascular damage are high white blood cell count, increased cerebral blood flow, and high flow velocity due to chronic anemia. In agreement, our preliminary experiments in SCD mice that were quite anemic found an increase in cerebral blood flow speed (**Fig. 6.3**). The severity of SCA is often determined by the severity of anemia, but the correlation between level of anemia and risk for serious complications is not well understood (*1*). The role of leukocytes in vaso-occlusive events is also still an active area of investigation.

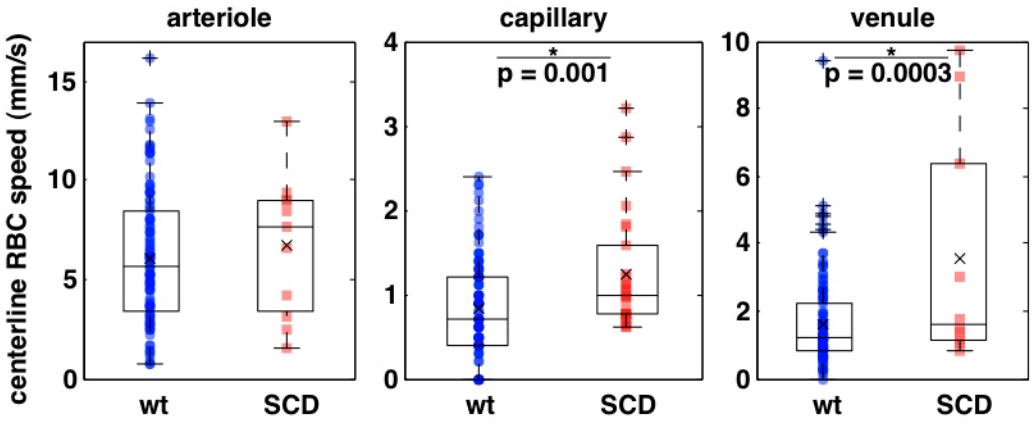

Figure 6.3: Centerline RBC Flow Speed in the Brain of SCD Mouse Model
Centerline RBC flow speed of cortical capillaries and venules increased significantly compared to wildtype control.

Hemolysis in SCA may also contribute to development of progressive vasculopathy characterized by systemic and pulmonary hypertension, endothelial dysfunction, and changes in the intima and smooth muscle of blood vessels (*1*). Previous epidemiological studies suggest that several complications are associated with increased rates of hemolysis. These conditions include cholelithiasis (or gallstones), cutaneous leg ulceration, priapism, and pulmonary hypertension. They were also found to be associated with low steady-state hemoglobin concentrations and tissue oxygenation (*6, 7*). An association between the development of pulmonary hypertension and the intensity of hemolytic anemia was noted in three prospective screening studies of adults with SCD (*6, 8, 9*) and in pediatric studies (*10, 11*). Pulmonary hypertension has also been reported in other forms of chronic hereditary and acquired hemolytic anemia.

VASO-OCCLUSIVE CRISIS

It is thought that RBCs and leukocytes become trapped in microcirculation through physical entrapment or adhesive interactions and obstruct blood flow, leading to painful ischemic injury (*12*). Rigidity of the sickle RBCs and inflammatory response may lead to a cycle of temporary occlusions and ischemia, followed by reperfusion coupled with increased oxidative and inflammatory stress (**Fig. 6.2**). This may lead to increased expression of endothelial adhesion markers, increased synthesis of inflammatory cytokines, and leukocytosis (*1*)—a mechanism similar to our hypothesis in the study of myeloproliferative neoplasms (Chapter 5). Increase in dissolved hemoglobin due to hemolysis, and the corresponding inactivation of nitric

oxide (NO), also contributes to heightened oxidative stress and excessive vasoconstriction (**Fig. 6.4**) (*12*). As sickle RBCs have been observed to aggregate with platelets, leukocytes, as well as other RBCs, it is unclear to what extent leukocytes are responsible for vaso-occlusion, but there is evidence that adherent leukocytes may capture circulating RBCs and produce vascular occlusion (*13*). For example, intravenous immunoglobulin administration that suppresses inflammation decreased reduced adherent leukocyte numbers, and dramatically inhibited interactions between RBCs and leukocytes, resulting in improved microcirculatory blood flow and survival of SCD transgenic mice.

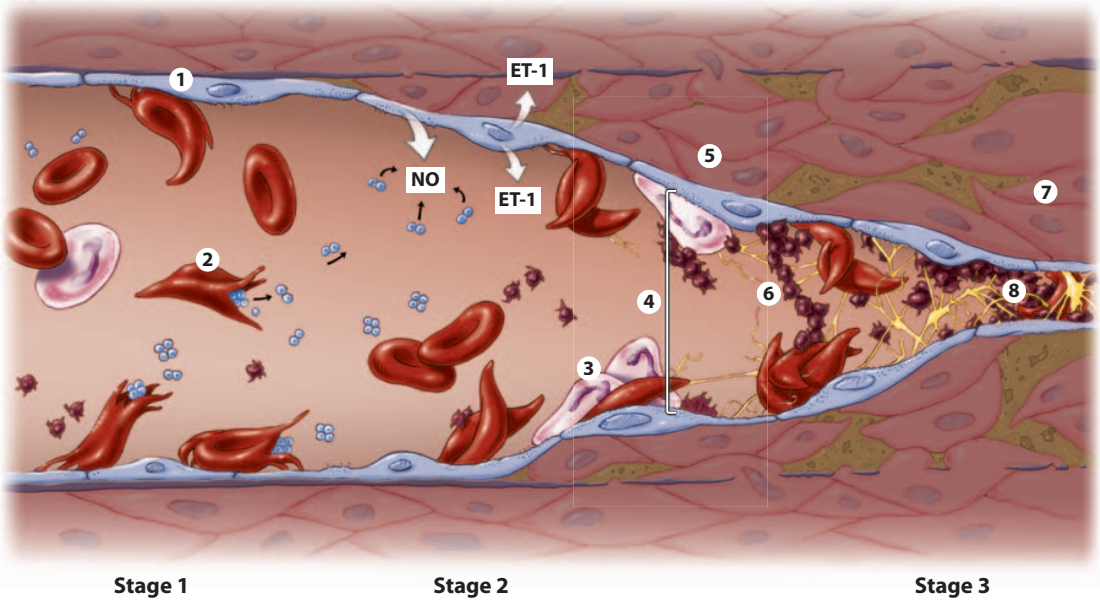

Figure 6.4: Steps in Vaso-occlusion in Larger Arteries
(1) Sickle RBCs adhere to endothelium. (2) Hemolysis. (3) White blood cell adhesion. (4) Increased vascular tone. (5) Neointimal proliferation. (6) Platelet aggregation. (7) Vasculopathy. (8) Vaso-occlusion.
ET-1, endothelin-1; NO, Nitric Oxide (*14*).

Previous SCA research has mainly focused on organ damage in the spleen, kidney, lungs, and liver. The cognitive effects of SCD, on the other hand, have been studied mostly in clinical cases. Normal cerebral blood flow is key to robust cognitive function in humans. Adequate oxygenation, nutrients delivery, and waste removal are necessary for robust tissue function. Regions of tissue death due to low oxygenation in the brain have been found in patients suffering from SCA (*1, 15*). Following stroke, many patients show improvement in neurologic function in the year following the event, but none recover to their original level of neurologic function. The level of cognitive and functional decline following stroke also increased in severity with increasing number of reoccurrences of stroke (*4*). In addition, children with regions of cerebral tissue death display impaired cognitive function in tests including language ability and spatial memory (*15*). A deeper understanding of cognitive decline in SCA, however, could extend to a more fundamental understanding of the mechanisms that link cognitive impairment with cerebrovascular diseases.

PRELIMINARY EXPERIMENTS AND RESULTS

In our preliminary experiments, we utilized Berkeley sickle cell mice which contains human α, β^S, $^A\gamma$, $^G\gamma$, β globin transgene and lack murine α and β globins ($\alpha^{-/-}$, $\beta^{-/-}$) as bone marrow cell donors(*16*). Using bone marrow transplantation procedures as described in Chapter 5, the resulting recipient mice exhibit human sickle cells. We examined cerebral microcirculation of the SCD mouse models using *in vivo* two-photon excited fluorescence (2PEF) imaging approaches from Chapter 4 and 5. So far, we have revealed increased RBC flow speed in the cerebral vessels (**Fig. 6.3**), which

correlates to high risk of stroke. In addition, the increase in flow speed modulation with heart beat (**Fig. 6.5**) coupled with a decrease in delay between heart beat and peak flow speed (**Fig. 6.6**) suggests a reduction in vascular distensibility and flexibility, especially in capillaries deep in the cortex where vasodilation was also found (**Fig. 6.7**). This chronic vasodilation leads to overall increase in the fraction of the brain volume taken up by the vasculature (**Fig. 6.8A-F**). We did the following calculation using the measured vascular volume (**Fig. 6.8G**) to rule out possible angiogenesis.

V = proportion of vascular volume
r = capillary radius
L = total vascular length

$$V \propto r^2 L$$

$$\frac{V_{wt}}{V_{SCD}} = \frac{r_{wt}^2 L_{wt}}{r_{SCD}^2 L_{SCD}}$$

$$= \frac{r_{wt}^2}{r_{SCD}^2} \text{ if } L_{wt} = L_{SCD}$$

$$\text{calculated}: \quad \frac{V_{wt}}{V_{SCD}} = \frac{r_{wt}^2}{r_{SCD}^2} = \frac{2.60^2}{3.37^2} = 0.60$$

$$\text{experimental}: \quad \frac{V_{wt}}{V_{SCD}} = \frac{0.021}{0.033} = 0.64$$

Since the experimental ratio of $\frac{V_{wt}}{V_{SCD}}$ is similar to the calculated value, we concluded that the increase in vascular volume in SCD mice is mainly due to chronic vasodilation. Lastly, we witnessed some vaso-occlusive events in cortical capillaries, although this increase in stalled microvessels is not statistically significant. Overall,

our preliminary data show promising work for detailed examination of the impact of SCD on cerebral microcirculation and vascular structure that may reveal the mechanisms of disturbed blood flow in microcircular networks.

.

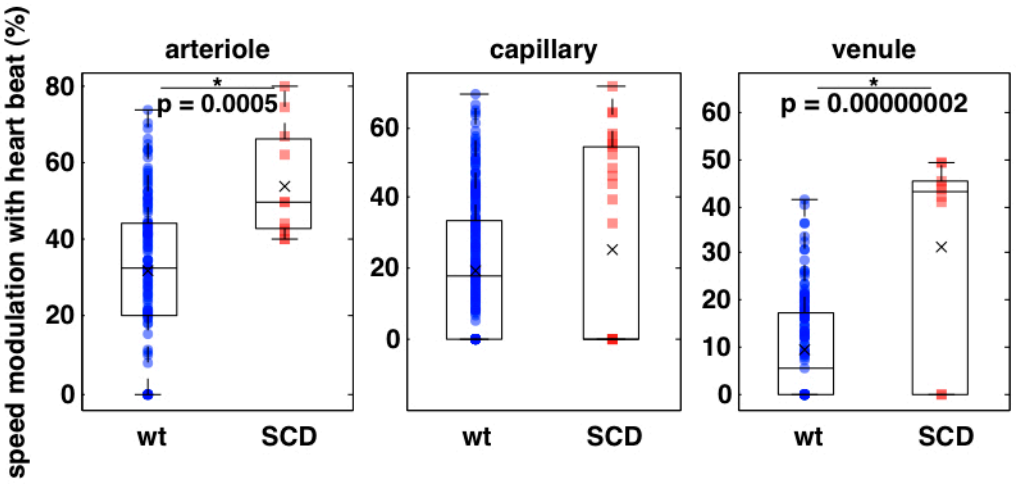

Figure 6.5: Speed modulation with heart beat in the brain of SCD Mouse Model
Speed modulation with heart beat in cortical arterioles and venules significantly increased compared to wildtype

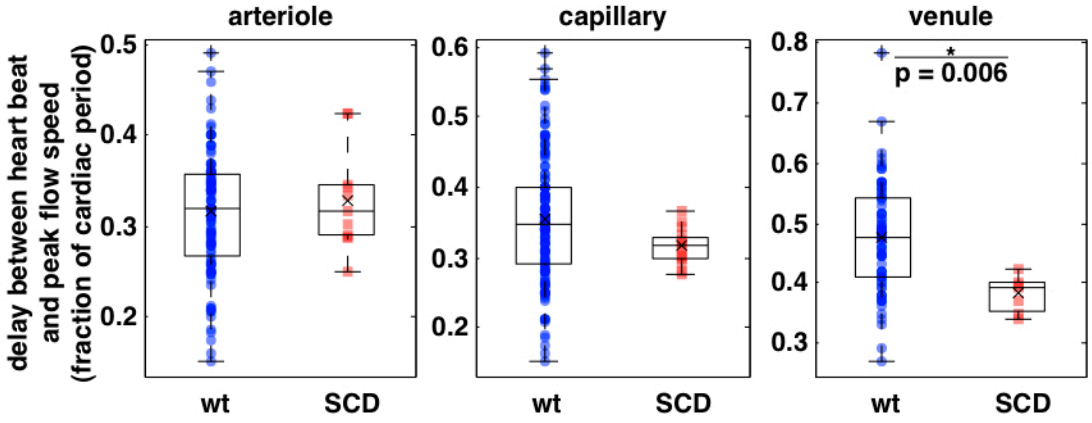

Figure 6.6: Delay between heart beat and peak flow speed in the brain of SCD mouse model

Delay between heart beat and peak flow speed decreased significantly in surface venule

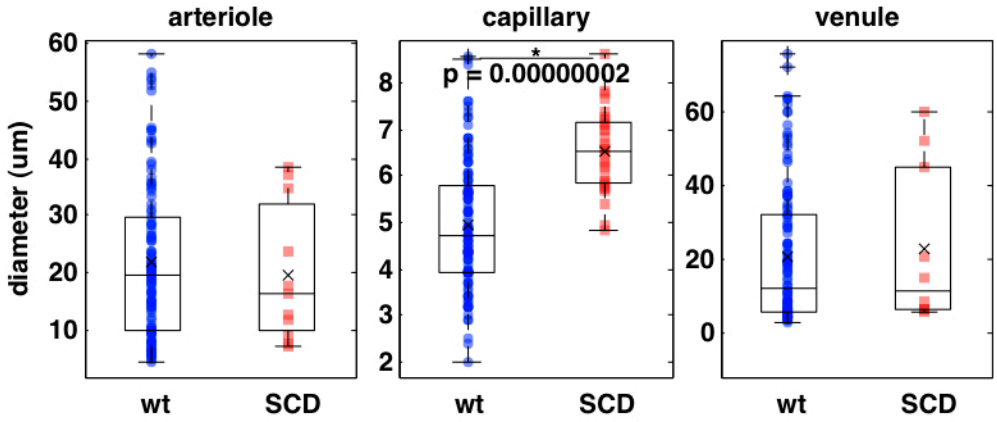

Figure 6.7: Cerebral microvascular diameter of SCD mouse model
Cortical capillaries of SCD mice were significantly dilated.

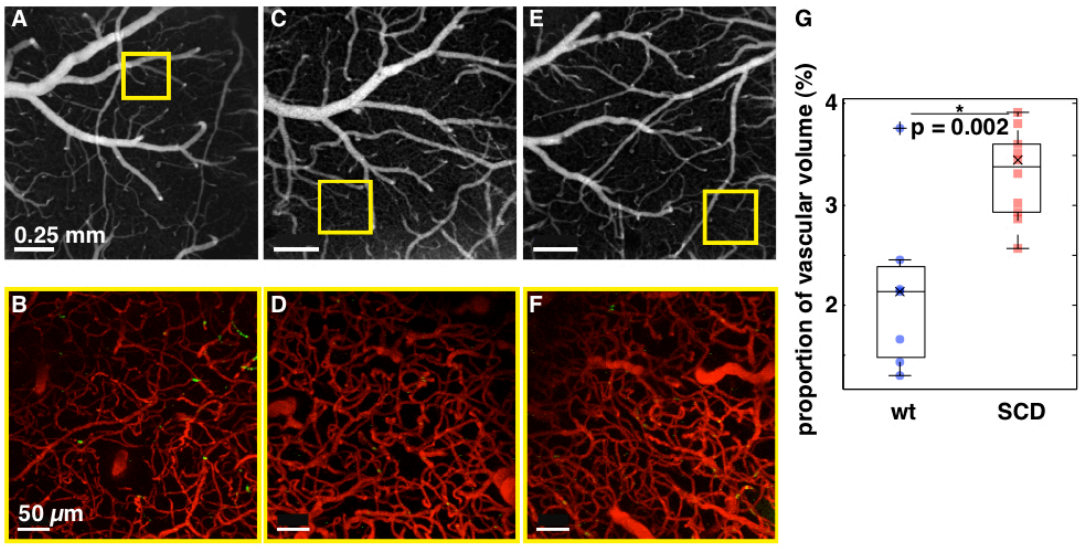

Figure 6.8: Vascular volume in the brain of SCD mouse model
Low magnification z-projection of cortical vasculature images of wildtype (A), and SCD mice (C and E) with their corresponding high magnification images (B, D, and F, respectively). The proportion of vascular volume in the brain of SCD mice was significantly higher than in wildtype mice (G).

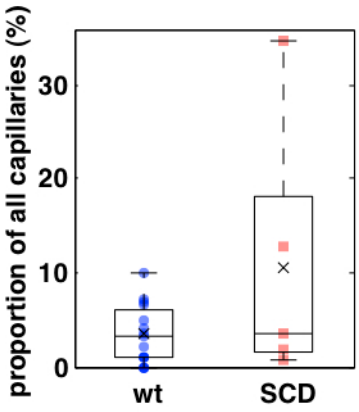

Figure 6.9: Cortical capillary occlusions in SCD mouse model
A trend of elevated capillary stall in SCD mice was observed, although not statistically significant.

REFERENCE

1. D. C. Rees, T. N. Williams, M. T. Gladwin, Sickle-cell disease. *Lancet* **376**, 2018 (Dec 11, 2010).
2. D. K. Kaul, M. E. Fabry, P. Windisch, S. Baez, R. L. Nagel, Erythrocytes in sickle cell anemia are heterogeneous in their rheological and hemodynamic characteristics. *J Clin Invest* **72**, 22 (Jul 1, 1983).
3. G. A. Barabino, M. O. Platt, D. K. Kaul, Sickle Cell Biomechanics. *Annual review of biomedical engineering*, (May 10, 2010).
4. D. Powars, B. Wilson, C. Imbus, C. Pegelow, J. Allen, The natural history of stroke in sickle cell disease. *Am J Med* **65**, 461 (Sep 1, 1978).
5. K. Ohene-Frempong *et al.*, Cerebrovascular accidents in sickle cell disease: rates and risk factors. *Blood* **91**, 288 (Jan 1, 1998).
6. M. T. Gladwin *et al.*, Pulmonary hypertension as a risk factor for death in patients with sickle cell disease. *N Engl J Med* **350**, 886 (Feb 26, 2004).
7. G. J. Kato, M. T. Gladwin, M. H. Steinberg, Deconstructing sickle cell disease: reappraisal of the role of hemolysis in the development of clinical subphenotypes. *Blood Rev* **21**, 37 (Jan 1, 2007).
8. L. M. De Castro, J. C. Jonassaint, F. L. Graham, A. Ashley-Koch, M. J. Telen, Pulmonary hypertension associated with sickle cell disease: clinical and laboratory endpoints and disease outcomes. *Am J Hematol* **83**, 19 (Jan 1, 2008).

9. K. I. Ataga *et al.*, Pulmonary hypertension in patients with sickle cell disease: a longitudinal study. *Br J Haematol* **134**, 109 (Jul 1, 2006).

10. N. Dham *et al.*, Prospective echocardiography assessment of pulmonary hypertension and its potential etiologies in children with sickle cell disease. *Am J Cardiol* **104**, 713 (Sep 1, 2009).

11. C. P. Minniti *et al.*, Elevated tricuspid regurgitant jet velocity in children and adolescents with sickle cell disease: association with hemolysis and hemoglobin oxygen desaturation. *Haematologica* **94**, 340 (Mar 1, 2009).

12. R. L. Nagel, M. E. Fabry, M. H. Steinberg, The paradox of hemoglobin SC disease. *Blood Rev* **17**, 167 (Sep 1, 2003).

13. J. Chang, P. A. Shi, E. Y. Chiang, P. S. Frenette, Intravenous immunoglobulins reverse acute vaso-occlusive crises in sickle cell mice through rapid inhibition of neutrophil adhesion. *Blood* **111**, 915 (Jan 15, 2008).

14. J. A. Switzer, D. C. Hess, F. T. Nichols, R. J. Adams, Pathophysiology and treatment of stroke in sickle-cell disease: present and future. *Lancet Neurol* **5**, 501 (Jun 1, 2006).

15. M. Prengler, S. Pavlakis, I. Prohovnik, R. Adams, Sickle cell disease: the neurological complications. *Ann Neurol* **51**, 543 (May 1, 2002).

16. E. A. Manci, Pathology of Berkeley sickle cell mice: similarities and differences with human sickle cell disease. *Blood* **107**, 1651 (Feb 15, 2006).

17. N. Sabaa *et al.*, Endothelin receptor antagonism prevents hypoxia-induced mortality and morbidity in a mouse model of sickle-cell disease. *J Clin Invest* **118**, 1924 (May 1, 2008).

CHAPTER 7

CYCLIC STRAIN ANISOTROPY REGULATES VALVULAR INTERSTITIAL CELL PHENOTYPE AND TISSUE REMODELING IN THREE-DIMENSIONAL CULTURE

Russell A. Gould, Karen Chin, Thom P. Santisakultarm, Amanda Dropkin, Jennifer M. Richards, Chris B. Schaffer, Jonathan T. Butcher

Department of Biomedical Engineering, Cornell University, Ithaca, NY 14853

This research is my work from a collaboration, which was originally published in the Acta Biomaterialia. This paper was reprinted with permission from Elsevier Ltd. R. A. Gould *et al.*, Cyclic strain anisotropy regulates valvular interstitial cell phenotype and tissue remodeling in three-dimensional culture. *Acta biomaterialia*, (Jan 11, 2012).
My specific contribution was second harmonic generation imaging of collagen fibers.

ABSTRACT

Many planar connective tissues exhibit complex anisotropic matrix fiber arrangements that are critical to their biomechanical function. This organized structure is created and modified by resident fibroblasts in response to mechanical forces in their environment. The directionality of applied strain fields changes dramatically during development, aging, and disease, but the specific effect of strain direction on matrix remodeling is less clear. Current mechanobiological inquiry of planar tissues is limited to equibiaxial or uniaxial stretch, which inadequately simulates many in vivo environments. In this study, we implement a novel bioreactor system to demonstrate the unique effect of controlled anisotropic strain on fibroblast behavior in three-dimensional (3-D) engineered tissue environments, using aortic valve interstitial fibroblast cells as a model system. Cell seeded 3-D collagen hydrogels were subjected to cyclic anisotropic strain profiles maintained at constant areal strain magnitude for up to 96 h at 1 Hz. Increasing anisotropy of biaxial strain resulted in increased cellular orientation and collagen fiber alignment along the principal directions of strain and cell orientation was found to precede fiber reorganization. Cellular proliferation and apoptosis were both significantly enhanced under increasing biaxial strain anisotropy ($P < 0.05$). While cyclic strain reduced both vimentin and alpha-smooth muscle actin compared to unstrained controls, vimentin and alpha-smooth muscle actin expression increased with strain anisotropy and correlated with direction ($P < 0.05$). Collectively, these results suggest that strain field anisotropy is an independent regulator of fibroblast cell phenotype, turnover, and matrix reorganization, which may inform normal and pathological remodeling in soft tissues.

GRAPHICAL ABSTRACT

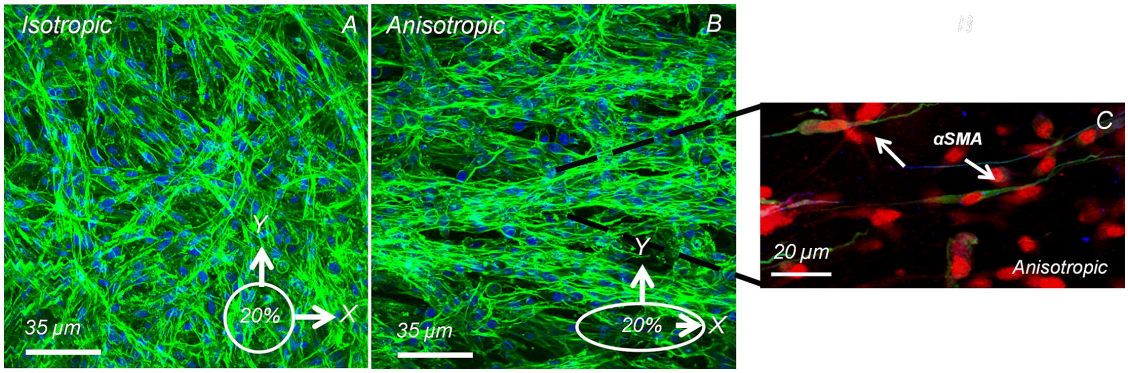

Valvular interstitial cells rapidly reorient orthogonally with biaxial anisotropic strain, while modulating directional levels of ACTA2. (A) During isotropic strain, orientation of valvular interstitial cells (f-actin, green) align without a preferred direction (DNA, blue). (B) During anisotropic strain, cellular orientation aligns with respect to the principal directions of strain. (C) A larger degree of ACTA2 expression (green) occurs perpendicular to the first principal strain direction (DNA, red).

INTRODUCTION

Planar connective tissues such as the diaphragm, pericardium, and valve leaflets perform critical biomechanical functions under cyclic mechanical loading (*1*) and (*2*). These tissues have evolved complex multidirectional collagenous fiber orientations that result in anisotropic mechanical properties ideally suited to their local microenvironment. Resident tissue fibroblasts continuously repair and remodel their tissue microenvironment in response to these mechanical cues, including secreting and/or degrading extracellular matrix proteins, releasing soluble growth factors, and reorganizing cell–cell/cell–matrix adhesive interactions (*3*) and (*4*). Fibroblasts transition between a quiescent synthetic phenotype, characterized by homeostatic matrix turnover, to activated contractile myofibroblasts that change the underlying matrix mechanics and/or composition depending on the remodeling state of the tissue (*5*). For example, during wound closure and fibrosis/scar formation, myofibroblasts elevate expression of contractile proteins and generate traction forces that create mechanical tension to pull matrix fibers together (*6*). Heart valve leaflets are exposed to arguably the most demanding mechanical environment in the body, yet interstitial fibroblasts thrive and mediate significant matrix turnover (*7*) and (*8*). Mechanical microenvironmental cues therefore provide strong inductive signals regulating tissue homeostasis and remodeling, but how they mediate healthy instead of pathological tissue remodeling remains poorly understood.

Mechanistic understanding of fibroblast-mediated tissue remodeling has advanced considerably with the aid of engineered tissue models that enable testing of molecular, cellular, and tissue scale mechanisms within a well-defined, repeatable, and physiologically relevant microenvironment (*9*). Fibroblasts in anchored three-dimensional (3-D) hydrogels develop mechanical tension leading to increased expression of contractile proteins, enhanced matrix synthesis, and release of growth factors such as transforming growth factor-beta (TGFβ), while fibroblasts in free-floating unstressed gels remain quiescent (*10*). More recently, bioreactors have been developed to apply specific mechanical strain parameters uniformly to specimens so as to isolate the underlying signaling mechanisms (*11*). For example, cyclic stretching of fibroblasts in vitro induces cytoskeleton rearrangement (*12*), focal adhesion clustering (*13*), and downstream intracellular signaling cascades leading to cell and matrix fiber reorganization (*14*). While the effects of strain magnitude and frequency have been studied for some time, the unique signaling from strain directionality is much less known. Cyclic uniaxial (one direction) stretch-induced TGFβ1, collagen III and fibronectin gene expression in cardiac fibroblasts. Equiaxial (isotropic) strain, however, induced divergent responses in extracellular matrix (ECM) mRNA levels (*15*). Fibroblasts have also been shown to align perpendicular to the direction of principal strain, while no-preferred direction occurs during equiaxial strain (*16*). Given that planar tissues experience multi-axial strain patterns in vivo and exhibit anisotropic biomechanical properties rather than either of the above extremes (*17*), it is therefore critically important to understand how biaxial strain anisotropy independently affects molecular signaling, fibroblast phenotype, and matrix remodeling behavior.

While biaxial and even triaxial stretches have been applied to tissues in cylindrical configurations, such as blood vessels (*18*), a similar device for planar 3-D engineered tissues has not been developed. Well-defined anisotropic biaxial strain fields have to date only been applied to planar cultures on two-dimensional (2-D) substrates (*19*). Biaxial (radial and circumferential) tensile strains can be applied in two dimensions using a vacuum-pressure (Flexcell) system, but strain magnitude varies in homogeneously with distance from the center of the membrane (*20*). Tan et al. also generated static heterogeneous anisotropic biaxial micro-strain patterns through multi spoke and microgroove array patterned 2-D substrates (*21*). We previously showed that smooth muscle cells exposed to homogeneous equiaxial stretch in 3-D culture dedifferentiate to synthetic myofibroblasts (*22*). Studies with valve fibroblasts in 3-D culture have shown heterogeneous changes in cell phenotype and matrix synthesis, but these could not be directly related to specific strain profiles (*23*).

The objective of this study, therefore, was to test how biaxial strain anisotropy independently controls fibroblast cell phenotype and matrix remodeling in 3-D environments. We developed and implemented a novel cyclic biaxial strain bioreactor with controllable homogeneous strain field anisotropy for engineered tissue hydrogels. We hypothesized that valvular interstitial cells (VICs) would align with respect to the principal directions of strain and rapidly remodel the underlying matrix to mirror this alignment pattern. We first determined the temporal changes in cell and matrix fiber

reorganization with strain anisotropy, followed by quantification of cell proliferation, apoptosis, and fibroblast phenotype.

MATERIALS AND METHODS

Bioreactor design and optimization

Our challenge was to create a bioreactor test system that enabled fabrication and stable anchoring of 3-D hydrogels, while applying a controlled multiaxial mechanical stimulation without having to disturb the tissue. We hypothesized that if elliptically shaped 3-D hydrogels were stretched uniformly along their outer perimeters, then the internal strain field would be homogeneous but biaxial. To evaluate this, finite element simulations (FEA, ANSYS Inc.) were first conducted to optimize geometric parameters for the bioreactor system. 20,000 prismatic rectangular elements were used with large strain hyperelastic (Mooney-Rivlin, modulus = 1 MPa) material properties performed on quarter-symmetric circular sections of silicone slab and platen. Both elliptical and circular slabs and/or platens were tested, with radii between 0.5 and 2 in. Platen/cassette hole diameter ratios were varied between 0.5 and 0.9. Slab thickness was varied from 2 to 6 mm, with well depth ratios ranging from 0.5 to 0.9. Finally, well centroid within the slab was translated radially from concentric to 75% of the platen radius. Design optimization criteria were to (1) maximize the number of samples testable within one cassette well, (2) maximize the size of samples testable, (3) maximize the depth of the PDMS wells, (4) maximize the possible applied strain magnitude, and (5) minimize the stress developed in the PDMS.

To fabricate these different hydrogel 3-D geometries, we developed thick elastomeric slabs instead of commonly used thin membranes (described below), which were secured between two circular aluminum flanges of a cassette (**Fig. 7.1A**). Each

cassette contained four cylindrical holes (where the slabs were exposed) positioned concentrically over Teflon lined platens. Negative molds were machined from polycarbonate such that small wells would be present within the silicone slab spanning the cassette holes above the platens (**Fig. 7.1B**). Molds were designed with ellipsoidal wells of major/minor axis ratios (hereafter *X* and *Y* respectively) of 1:1, 2:1, and 4:1. Beveled edges were machined within the ellipse to ensure uniform vertical strain fields through the well edges and to secure a compression spring (Lee spring) for anchoring hydrogels. Polydimethylsiloxane (PDMS Sylgard 184, Dow Corning) was formed at a concentration of 20:1, degassed, poured into the negative molds, and solidified at 70 °C for 12 h. Slabs were then released from the molds, mounted within the aluminum cassettes, and autoclaved before use (**Fig. 7.1C**). The stage was constrained to vertical motion using shafts with linear bearings. A rotary stepper motor (34Y, Anaheim Automation) drove vertical translation through a screw-pinion gear assembly (**Fig. 7.1D**). Limit switches were mounted on either side of the translation stage to prevent overstrain and semi-automate calibration. A cold plate (CP12, Lytron) was placed underneath the stepper motor for heat transfer. Strain magnitude and frequency waveforms were applied to the motor via a controller module and custom software (DPN10601, Anaheim Automation).

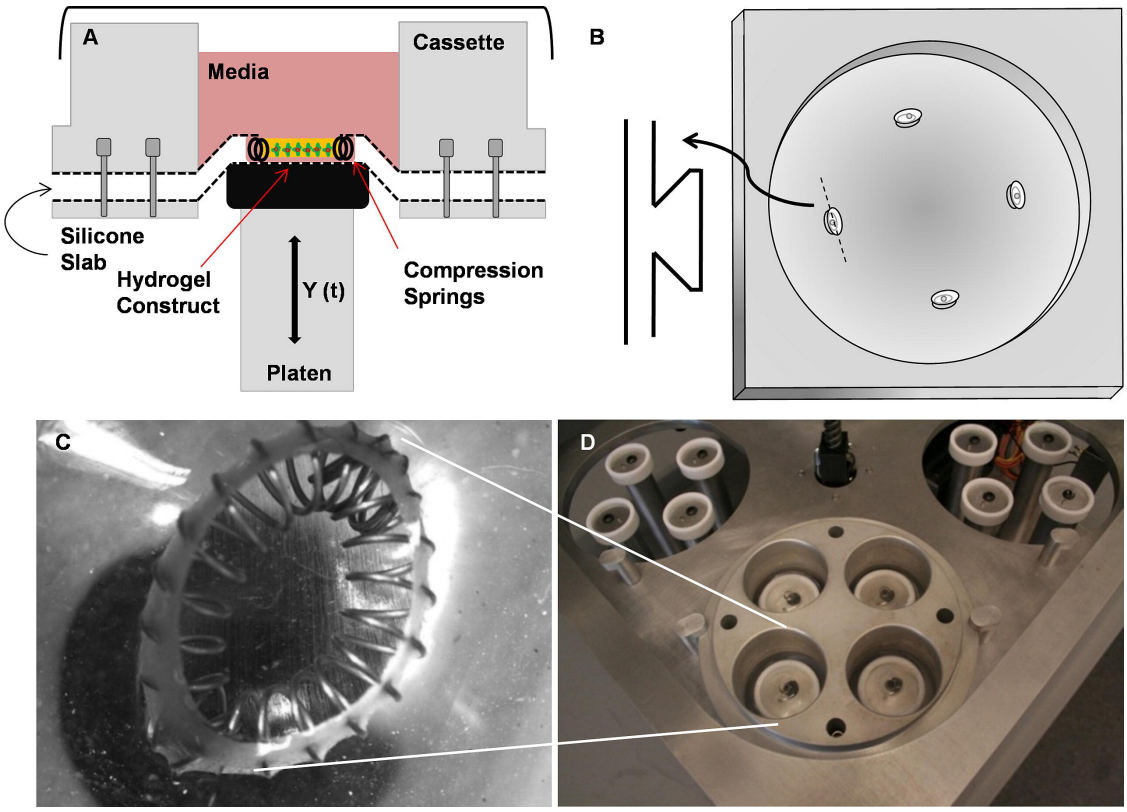

Fig. 7.1. Design of the anisotropic biaxial strain (ABS) bioreactor.
(A) Conceptual schematic showing a cross-sectional view of a constrained collagen construct embedded in a silicone slab and loaded within an aluminum cassette. (B) An inverted polycarbonate negative mold with machined circular and elliptical wells used for constructing the silicone slab. (C) An expanded view of the elliptical well containing elliptical compression springs. (D) Macroscopic view of the bioreactor containing four cassettes and 16 independent wells.

3-D hydrogel formation

Collagen hydrogel 3-D tissue constructs were created using a procedure from one previously described (*24*). Briefly, porcine aortic leaflets were harvested from a local abattoir and valvular interstitial cells were isolated immediately (*25*). For these experiments, 400,000 cells/ml at P4-P6 were suspended in 3× DMEM with 10% FBS (Gibco), 2 mg/ml type I collagen (BD), and 0.1 M NaOH added to neutralize the solution. Depending on the geometry (ratio of major to minor axis) of the well, different volumes of gel were added. For the 1:1, 2:1, 4:1, and control wells, 100 µl, 125 µl, 150 µl, and 125 µl respectively of gel was inoculated into the wells containing the compression springs. Gels solidified after 60 min, after which additional culture medium was added to the reservoir. The experimental controls consisted of a mechanically stressed but non-strained gel (anchored isotropic static) and a free-floating gel (unanchored isotropic state). As in other studies(*26*) and (*27*), hydrogels were cultured for 24 h prior to experiments, allowing the VICs to spread and compact the matrix around the springs to create a flat 3-D tissue.

Strain field calibration

Marker fields (40 µm glass beads) were placed along the well bottom, gel surface, and at the compression spring attachment points (**Fig. S7.1**). The stage was translated to different depths, and marker positions within multiple wells were imaged and digitally recorded using ImageJ. Assuming uniform deformation within small groups of three points, the local normal and shear strain field could be described by a system of equations as previously described (*22*) (see Supplementary material for

more details). Comparing multiple marker groups determined strain field homogeneity. At least three independent point groups were compared per well and experimental condition for calibration. For frequency response mapping, linear acceleration/deceleration-time commands of increasing magnitude and shorter time intervals were sent to the stepper motor, creating sinusoidal stage motion patterns. Peak sustainable frequencies were recorded for each applied strain magnitude (equiaxial configuration).

Biaxial strain experiments

We equalized all applied strain fields according to the apparent area strain experienced by the cells by the following formula:

$$A/A_o = \lambda X \lambda Y = (2EXX+1)^{0.5}(2EYY+1)^{0.5} \quad (1)$$

where A is the current area, A_o is the initial area, λ_X is the stretch ratio in the X direction, λ_Y is the stretch ratio in the Y direction, and E_{XX}/E_{YY} represent the principal strains in the XX and YY directions, respectively. We designed all biaxial strain profiles such to maintain a 20% area strain, thus only the effects of strain field anisotropy were tested. 3-D cultures with 1:1, 2:1, and 4:1 aspect ratios were stretched at 20% area strain, 1 Hz frequency for up to 96 h. Upon completion of the experiments, gels were removed from the springs and subjected to quantitative endpoint assays.

Quantification of cell and matrix architecture

We quantified changes in cell orientation and matrix fiber reorganization at 48 and 96 h via multiphoton microscopy. Image stacks of the collagen hydrogels were taken from the central region of each well at 5 μm vertical steps. Z-stacks encompassed at least 80% of the gel thickness in each sample, but were limited by the penetration depth of laser microscopy and slight differences in hydrogel compaction. Cell orientation angle distributions within each gels (0° representing the *X* direction) were determined using f-actin staining (Sigma) and quantified from maximum intensity projections images using ImageJ as previously described (*28*). We manually traced the shape of hundreds of cells across multiple sections for each sample, and organized them within a histogram to enable comparison with the fiber alignment data. Alignment angle distributions from each gel were normalized to the most common alignment angle, which was assigned a value of 1. Simultaneously, collagen fibril alignment angle distributions were captured using second harmonic generation (SHG) imaging using a custom-built nonlinear laser scanning microscope employing 1040 nm, 1 MHz, 300 fs pulses from a Yb-fiber chirped pulse amplifier (FCPA μJewel D-400, IMRA America Inc.) as previously described (*29*). Similar to the cellular orientation quantification, fiber angle distributions within gels (0° representing the *X*-direction) were determined using central region Z-stacks and the maximum intensity projections images processed using ImageJ. ECM fibers were analyzed in total using an alignment algorithm (adapted from Ref. (*30*)) that assessed second harmonic generation autofluorescence (*30*). We observed no variation in histogram

profiles with relative *z*-axis position, and therefore pooled all the data into single histograms for each construct.

Proliferation and apoptosis assays

5-Bromo-2′-deoxyuridine (BrdU) incorporation was used to detect proliferating cells. BrdU labeling reagent (Invitrogen) was added to the culture media 12 h prior to experiment termination (48 h). Hydrogel constructs were fixed and targeted with a monoclonal Anti-BrdU Alexa Fluor 488 conjugate (PRB-1, Invitrogen). Total DNA was counterstained using a DRAQ-5 (Biostatus) far red nuclear dye. TUNEL (Apo-Brdu TUNEL assay kit, Invitrogen) was used to detect apoptotic cells. 48 h stretch and control hydrogels were fixed and stained for disrupted DNA targeted by incorporation of terminal deoxynucleotidyl transferase (Tdts) and 5-bromo-2′-deoxyuridine 5′-triphosphate (BrdUTPs). Monoclonal Ani-BrdU Alexa Fluor 488 conjugate was used to target the fragmented DNA and a propidium iodide counter stain was used to determine total cellular DNA. Positive fluorescent areas for each cell were measured using ImageJ and normalized by cell nuclei.

VIC phenotype

Alpha smooth muscle actin (gene name ACTA2, marker of myofibroblastic phenotype) and vimentin protein expression (VIM, indicative of quiescent fibroblast phenotype) were compared across strain conditions at 48 h using quantitative real-time PCR (RT-PCR, see supplemental methods) and immunohistochemistry. Antibody staining was performed as previously described (*22*). Image Z-stacks (10 μm intervals)

were taken with laser confocal microscopy (TCS or Leica LSM510) at fixed gain, offset, and averaging settings. Each label occupied a different fluorescence channel, and excitation lasers were sequentially activated to negate signal bleed. Z-stacks were taken at 5–10 μm sections and converted into maximum projections. Positive fluorescent areas for each color were measured using ImageJ and normalized by cell nuclei. Data was related as percentage of cells with cytoskeletal signal and compared across conditions.

Statistics

At least six samples per time point and treatment condition were used in each endpoint assay for statistical analysis. One-way ANOVA with Tukey's modified post hoc tests were used to compare differences between means and data were transformed when necessary to obtain equal sample variances. For proliferation/apoptosis studies, statistical tests were implemented across treatment conditions and results are expressed as mean ± standard error. For gene/protein expression studies, statistical tests compared individual genes across treatment conditions and results are expressed as mean ± standard deviation.$P < 0.05$ denoted statistical significance.

RESULTS

Design and optimization of the anisotropic biaxial strain (ABS) bioreactor

3-D collagen gels could be anchored within cyclically deforming wells through compression springs whose lengths were adjusted to press fit inside the outer edge of the well and were secured with a 60° beveled edge (**Fig. 7.1**). Preliminary finite element simulations determined that the major and minor axis lengths of an ellipsoidal well shape could independently control *XX* and *YY* strain magnitudes (**Fig. S7.2A**). Thus, by varying the eccentricity of the elliptical well, the biaxial strain profiles scaled with the major to minor axis ratio (**Fig. 7.2**). Further simulations were done to characterize well placement within the PDMS slab and dependence upon equiaxial well diameter. Using a 1:1 geometric ratio, we found that deviations in the placement of the well, up to 60% (25 mm) along the platen radius, did not significantly affect strain magnitude (**Fig. S7.2B**). It was also determined that the strain magnitude inversely correlated with well diameter, such that a reduction of 20–10% radial strain occurred when increasing well diameter from 2 to 8 mm (**Fig. S7.2C**). Finally, parametric optimization through finite element simulations predicted that for 50 cm diameter cassette holes and 6 mm wells, a silicone slab of 3/8″ thickness with 3 mm deep wells achieved a uniform 50% strain during 1 cm of stage translation. In this configuration, four holes could be fabricated in each cassette, and four cassettes could be secured on the translating stage. For these experiments, however, one well was created at the center of each cassette hole.

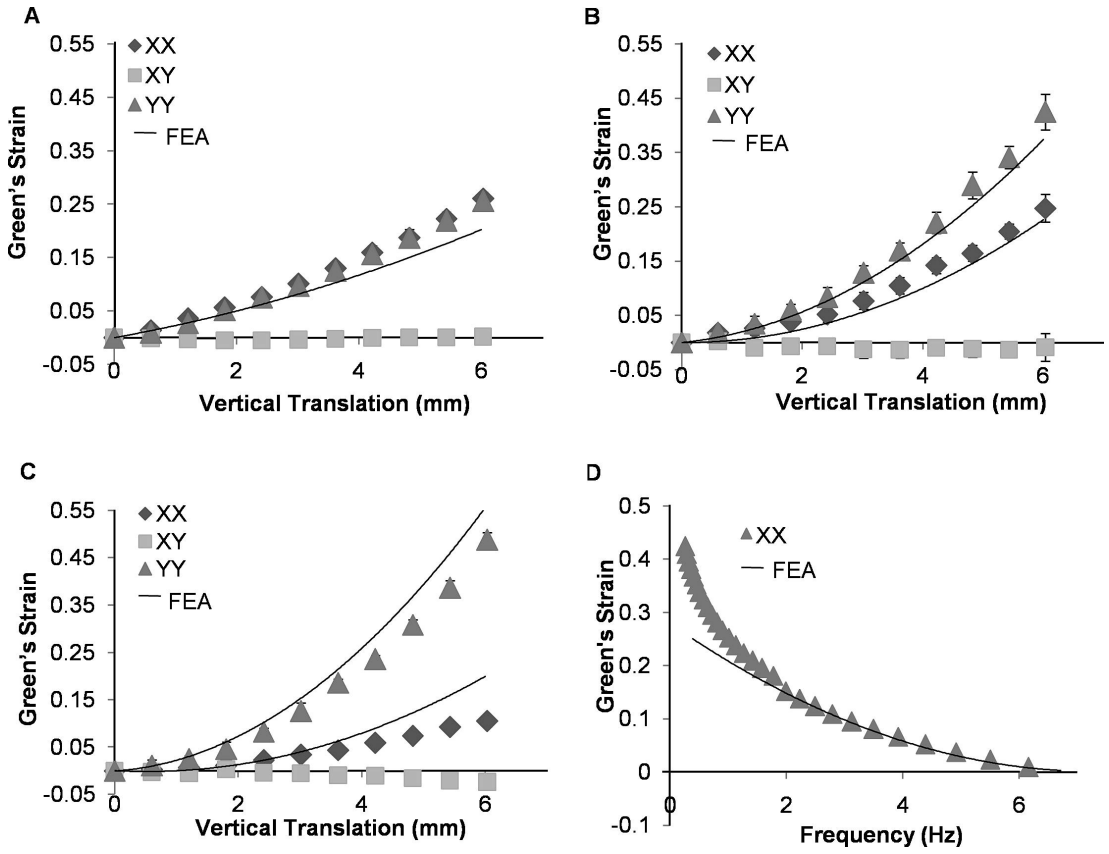

Fig. 7.2. Calibrated strain fields overlaid with FEA simulations.
(A) 1:1 circular well introduced an equiaxial strain field with minimal shear captured by FEA simulations. (B) 2:1 ellipsoidal well introduced a biaxial strain field captured by the FEA simulations. (C) 4:1 ellipsoidal well introduced a biaxial strain field that was slightly overestimated by the FEA simulations. (D) Strain vs. frequency curves for the 1:1 geometry indicates the ability to generate large deformations at high frequencies. Error bars show $\pm$SD. $N \geqslant 6$ samples for each geometry and strain magnitude condition.

We next compared our FEA simulations against measured strains of 3-D tissues within different elliptical well geometries. Stretching a 1:1 geometry introduced strains exceeding $25\% \pm 0.6\%$ resulted in no significant differences between E_{XX} and E_{YY} (**Fig. 7.2A**). Conversely, a 2:1 geometry created homogeneous biaxial strain fields of at least $20\% \pm 1.8\%$ in the E_{XX} and $42\% \pm 2.1\%$ in the E_{YY} directions, with negligible shear strain. The applied E_{XX}/E_{YY} strain ratio was consistently 2:1 regardless of applied strain magnitude or loading cycle (**Fig. 7.2B**). Stretching 4:1 geometries introduced strains exceeding $9.1\% \pm 1.1\%$ in the E_{XX} and $39\% \pm 1.2\%$ in the E_{YY}, with a nearly consistent 4:1 magnitude ratio (**Fig. 7.2C**). Experimental results confirmed FEA predicted nonlinear increases in applied biaxial strain magnitudes with stage translation. For all gel ratios, shear strain E_{XY} varied between $0 \pm 1.5\%$ at the maximum loaded conditions and can be considered not statistically different from zero strain. We next determined the maximum stable strain magnitude as a function of frequency (**Fig. 7.2D**). For equiaxial profiles, a maximum strain of 27%, 18%, 12%, 8% and 5% was achieved at 1, 2, 3, 4 and 5 Hz, respectively. Peak biaxial strain magnitudes in the *YY* direction were higher at each frequency, but proportional to the area strain during equiaxial loading. Collectively, these results establish and validate a unique and versatile high-throughput anisotropic biaxial strain bioreactor system for planar 3-D tissue cultures.

Biaxial strain anisotropy regulates cellular apoptosis and proliferation

VICs seeded 3-D collagen hydrogel constructs were strained at 20% area strain, with varying biaxial anisotropies at 1 Hz, and static cultures served as controls.

To verify that our bioreactor was able to maintain viable cells for at least 96 h, we performed a live/dead (green/red) assay on the hydrogel constructs. The percentage of live cells in the 1:1 (89% ± 1.3%) and 4:1 (86% ± 0.9%) geometries decreased with anisotropy compared to the percentage in anchored controls (91% ± 0.9%), but were consistently above 85% viability (**Fig. 7.3A–E**). At 48 h, the number of apoptotic cells (yellow) in the 2:1 (8.5% ± 0.3%) and 4:1 (9.6% ± 0.5%) geometries increased relative to anchored controls (5% ± 0.2%) (**Fig. 7.3F–J**). This result suggests that cell death is largely driven by strain-induced apoptosis rather than bioreactor cytotoxicity. An increase in cell proliferation was also visually apparent for the mechanically stimulated conditions at 48 h. Using BrdU labeling, we found that with increasing biaxial anisotropy, the number of proliferative cells (green) in the 1:1 (26% ± 1.9%), 2:1 (34% ± 1.4%), and 4:1 (37% ± 1.1%) geometries statistically increased relative to anchored controls (16%, ± 1%) (**Fig. 7.3K–O**). These findings suggest biaxial strain anisotropy enhances both cell proliferation and apoptosis, suggestive of an actively remodeling microenvironment.

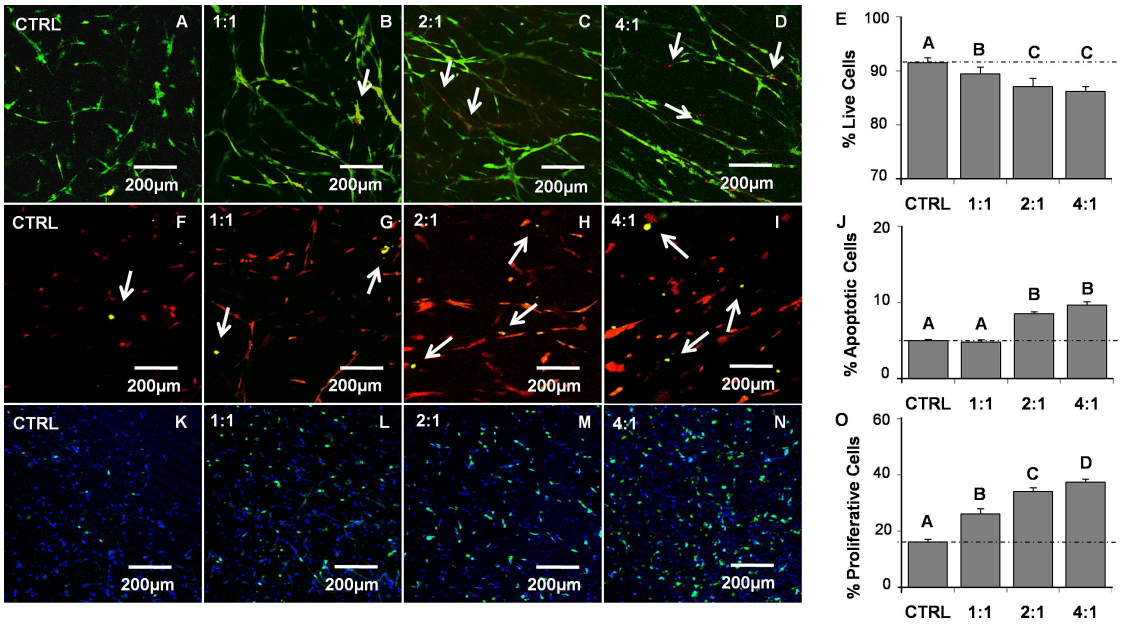

Fig. 7.3. Apoptosis and proliferation correlate with increasing biaxial anisotropy at 48 h.

(A–D) Live/dead assay reveals an increasing amount of dead cells with increasing biaxial anisotropy (live – green, dead – red). (E) Quantification of dead cells as a percentage of total cells. (F–I) Apo-BrdU assay reveals an increasing amount of apoptotic cells with increasing biaxial anisotropy (apoptotic–yellow, DNA – red). (J) Quantification of apoptotic cells as a percentage of total cells. (K–N) BrdU labeling assay reveals an increasing amount of proliferative cells with increasing biaxial anisotropy (proliferative – green, DNA–blue). (O) Quantification of proliferative cells as a percentage of total cells. Error bars show ± SE, $N \geqslant 6$ samples per test condition. ANOVA with Tukey's post hoc testing determined statistical significance at $p \leqslant 0.05$ thresholds. Bars that do not share letters are significantly different from each other.

Cell and matrix fibers rapidly reorient orthogonally with cyclic strain anisotropy

At 48 h, significantly more f-actin labeled cells were found in cyclically stretched compared to the statically anchored controls, which partly reflects both increased matrix compaction and proliferation (**Fig. S7.3A–D**). Static controls and 1:1 equiaxial strain revealed random orientations of cells denoted by the cytoskeletal (f-actin) filaments (**Fig. S7.3E and F**). Normalized cell and matrix alignment index distribution curves indicate that orientation along the major X (0°) and minor Y (90°) axes was maintained throughout a 0.3–0.8 range (**Fig. S7.3M and N**). In contrast, the 2:1 and 4:1 geometries revealed a cross-hatched network of cells aligning along the major and minor axes with greater cross-alignment in the 4:1 geometry (**Fig. S7.3G and H**). Normalized alignment curves indicate that alignment along the major and minor axes ranged from 0.90 to 0.95 and 0.50 to 0.40, respectively, while the 45° orientation dropped to a lower fraction of 0.1–0.2 (**Fig. S7.3O and P**). Second harmonic generation imaging of collagen fibrils showed a lack of fibril alignment regardless of strained condition (**Fig. S7.3I–L, M–P**). At 96 h, static controls and 1:1 cyclic equiaxial strain revealed random orientations of cells denoted by the cytoskeletal (f-actin) filaments (**Fig. 7.4A–B, E–F**). Normalized cell and matrix alignment index distribution curves indicate that orientation along the major X (0°) and minor Y (90°) axes was maintained throughout a 0.4–0.8 range (**Fig. 7.4M and N**). In contrast, the 2:1 and 4:1 geometries revealed a cross hatched network of cells aligning along the major and minor axes with greater cross-alignment in the 4:1 geometry (**Fig. 7.4C–D, G–H**). Normalized alignment curves indicate that alignment along the major and minor axes ranged from 0.85 to 0.95 and 0.55 to 0.35,

respectively, while the 45° orientation dropped to a lower fraction of 0.1–0.2 (**Fig. 7.4O and P**). Likewise, second harmonic generation imaging of collagen fibrils showed a similar trend such that increasing degrees of fibril alignment occurred with increasing anisotropic strain (**Fig. 7.4I–L, M–P**). Taken together, VICs rapidly reoriented within 48 h of cyclic strain and maintained orientation through 96 h. Extracellular matrix architecture, on the other hand, was poorly aligned at 48 h regardless of the applied strain field as determined by SHG, suggesting that cell orientation precedes fiber alignment. Collectively, these results demonstrate that applied cyclic biaxial strain anisotropy drives rapid VIC cell orientation and matrix fiber alignment in a temporally regulated manner, with cell reorientation leading extracellular matrix remodeling.

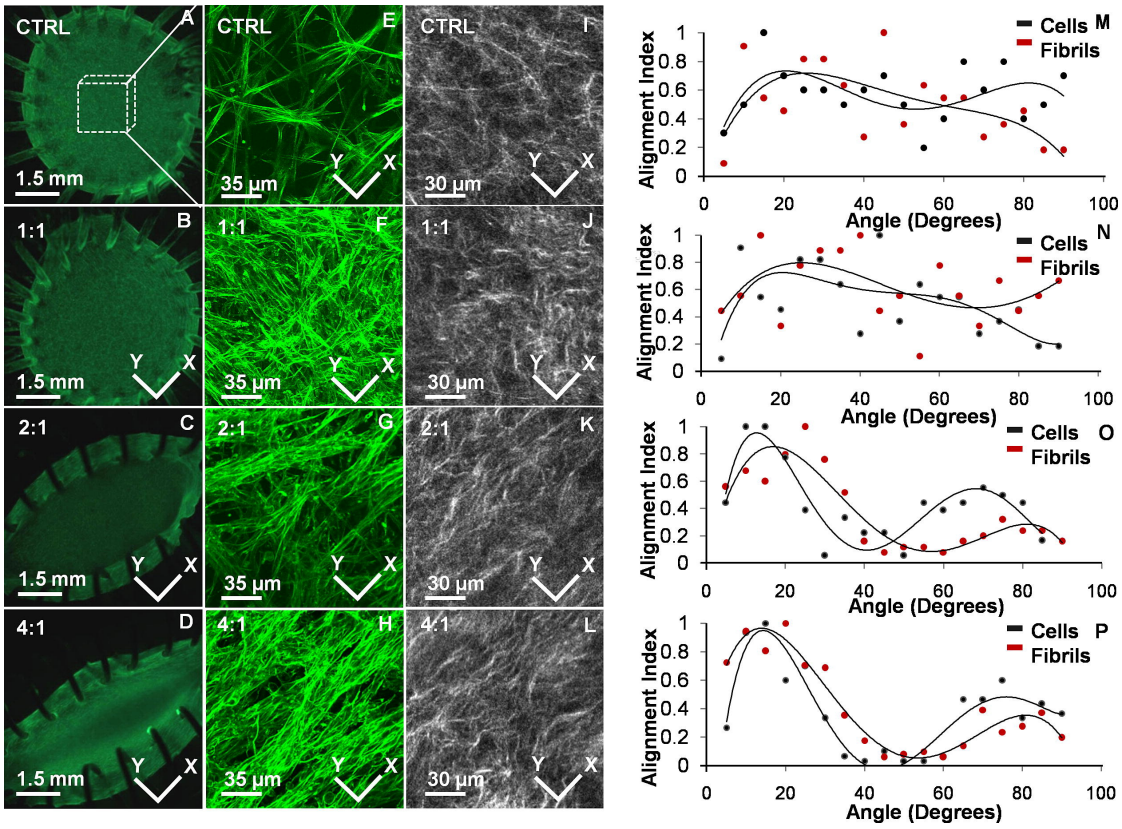

Fig. 7.4. Cell and matrix fibers rapidly reorient orthogonally with cyclic strain anisotropy at 96 h.

(A–D) Macroscopic view of collagen gels compacted within elliptical compression springs. (E–H) Orientation of VICs associated with the anisotropic strain profiles (f-actin-green). (I–L) Orientation of collagen fibrils associated with anisotropic strain profiles (SHG imaging). (M–P) Representative alignment curves indicate orientation of both VIC and collagen fibrils coincide and align with respect to the principal directions of strain. However, a larger degree cellular orientation and fiber alignment occurs perpendicular to the first principal strain direction (*Y*).

Valve interstitial cell phenotype is modulated by biaxial strain anisotropy

Alpha-smooth muscle actin (ACTA2) is a key cytoskeletal filament involved in many myofibroblastic phenotype behaviors. Within unanchored 3-D hydrogel cultures (free floating), VICs express low amounts of ACTA2. However, when cultured under anchored conditions (mechanically constrained), ACTA2 gene expression increased (2.87 ± 0.13 of control), indicating that tissue stress enhances myofibroblastic differentiation (**Fig. S7.4**). After 48 h of stretch at either the 1:1 or 2:1 geometries, ACTA2 gene expression was significantly downregulated with respect to anchored unstrained controls (expression $0.27\text{-}0.32 \pm 0.05$ fold of anchored control, no difference between). Stretch at the 4:1 geometry nearly doubled the amount of ACTA2 expression compared to equiaxial strain, but still less than half of the static anchored condition (0.47 ± 0.04 of control) (**Fig. 7.5A**). Vimentin (VIM) expression was insensitive to unanchored vs. anchored conditions (**Fig. S7.4**), but was significantly downregulated within the 1:1 or 2:1 geometries (0.62 ± 0.07 and 0.59 ± 0.13 respectively, no difference between). Stretch at the 4:1 geometry significantly increased VIM expression (1.13 ± 0.18 fold), recovering to control expression levels (**Fig. 7.5A**). These same trends were confirmed at the protein level via immunofluorescence (**Fig. 7.5B–F**). ACTA2 protein was downregulated significantly under equiaxial strain (0.61 ± 0.07) and slightly increased with the 4:1 geometry (0.76 ± 0.05). VIM was downregulated with equiaxial strain (0.76 ± 0.08) and then returned toward unstrained control levels with the 4:1 geometry (0.87 ± 0.06) (**Fig. 7.5G**). Interestingly, a preponderance of cells oriented parallel to the gel major axis

(thus perpendicular to the greater strain direction) expressed ACTA2 protein in the 4:1 geometry (**Fig. 7.5F**). Together, this suggests that cyclic strain anisotropy independently contributes to VIC fibroblast–myofibroblast differentiation tendencies. Equibiaxial to mildly anisotropic stretch decreases ACTA2 and VIM gene and protein expression, while more dramatic strain anisotropy increases both ACTA2 and VIM expression.

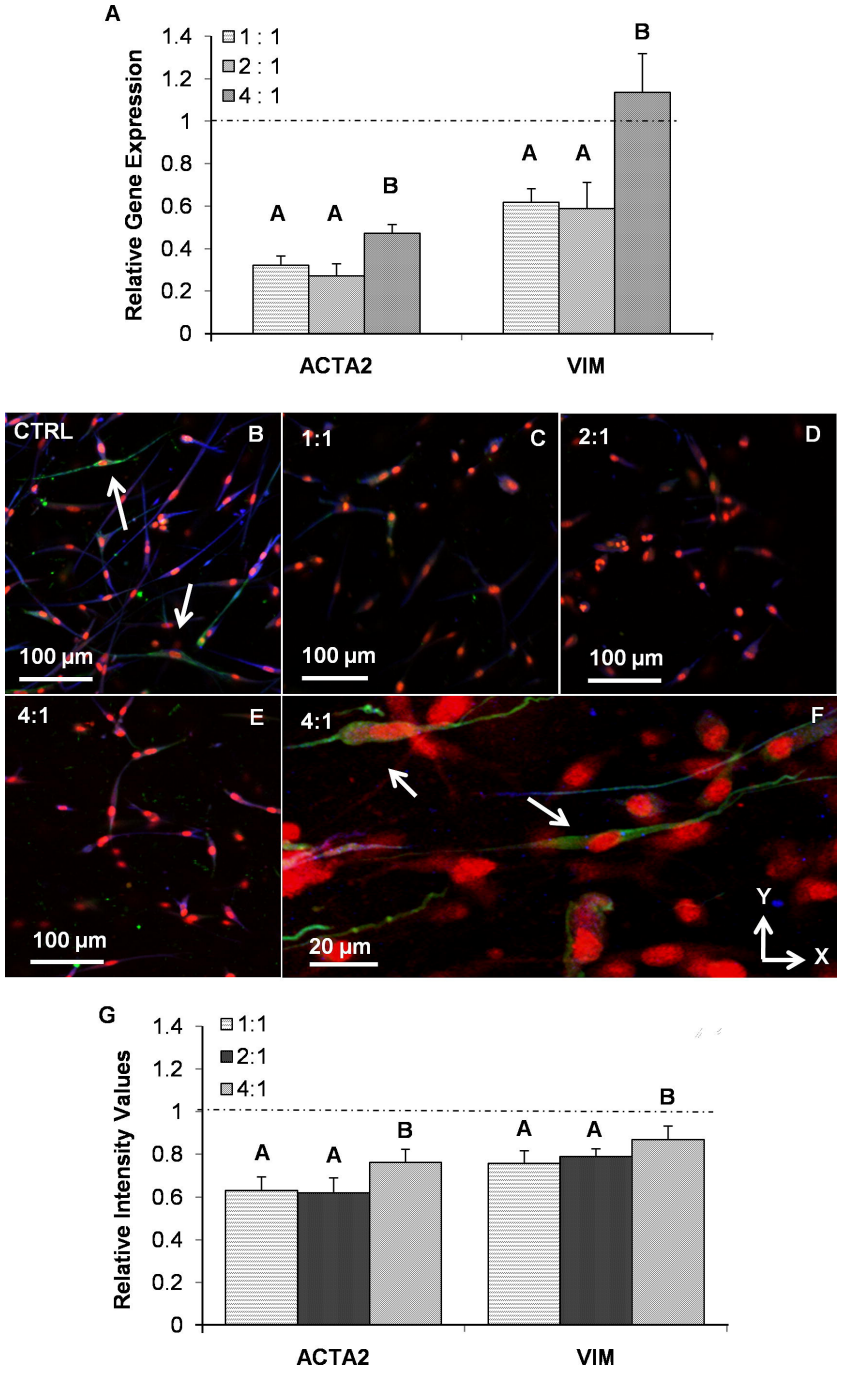
A
Relative Gene Expression
1.4
1.2
1
0.8
0.6
0.4
0.2
0
1 : 1
2 : 1
4 : 1
A
A
B
A
A
B
ACTA2
VIM
CTRL
B
100 µm
1:1
C
100 µm
2:1
D
100 µm
4:1
E
100 µm
4:1
F
20 µm
Y
X
G
Relative Intensity Values
1.4
1.2
1
0.8
0.6
0.4
0.2
0
1:1
2:1
4:1
A
A
B
A
A
B
ACTA2
VIM

Fig. 7.5. Biaxial strain anisotropy modulates fibroblast cell phenotype at 48 h.
(A) Gene expression was measured via real-time PCR, normalized to 18S, and expressed relative to unstretched anchored gel controls. ACTA2 gene expression decreased in all strain conditions, while VIM gene expression returned to control levels with 4:1 biaxial directionality. (B–F) ACTA2 (green) and VIM (blue) protein expression were measured via immunofluorescence with DNA (red) counterstain. (G) Quantification of total fluorescence was normalized to cell number and compared relative to unstretched control gels. (F) Although ACTA2 expression reduces with cyclic stretch, cells orienting perpendicular to the major axis of stretch expressed increased ACTA2 in the 4:1 geometry. Error bars show $\pm$ SD, $N \geqslant 6$ samples per strain geometry and protein. Bars that do not share letters are significantly different from each other as determined by one-way ANOVA with Tukey's post hoc ($p \leqslant 0.05$).

DISCUSSION

Anisotropic strain in vivo and in vitro

Many planar connective tissues exhibit heterogeneous matrix fiber orientations that dictate anisotropic biomechanical properties which are critical for proper function. As an example, aortic heart valve cusps are very compliant in the radial direction but stiff in the circumferential direction, which greatly assists in efficient Coaptation and rapid opening during the cardiac cycle. Simultaneous mechanical testing and collagen fiber distribution profiling demonstrates that anisotropic fiber splay and reorientation is a key contributor to physiological valve function (*31*) and (*32*). In altered loading environments, such as in hypertension or congenital malformation (e.g. bicuspid aortic valve), local cell and matrix architecture is modified with an increased risk of tissue degeneration (*33*), (*34*), (*35*) and (*36*). Greater understanding of how strain field anisotropy controls fibroblast cell phenotype and matrix remodeling has been challenging to study in vivo due to the confounding complexity of multiple interrelated biological signals and inherent tissue variability. Applying anisotropic strains within well-controlled 3-D culture systems has been limited by (1) an inability to prescribe strain magnitudes in orthogonal directions independently, and (2) difficulties in anchoring 3-D engineered tissues within bioreactors without compromising the homogeneity and consistency (over time) of the applied strain. Pneumatic actuator based elastomeric substrate deformation is commonly applied but rate-limited by the compressibility of air, rarely exceeding 1.5 Hz for physiological soft tissue strains. Alternatively, mechanical cams require constant adjustment and repeat calibration (*20*) and (*37*). Biaxial stretching of hydrogels was recently

performed by molding hydrogel constructs in a cross pattern within a rotating cam (*38*). However, the applied strain field was inhomogeneous and difficult to monitor over time. Furthermore, hydrogels can be adhered to elastomeric substrates via adhesive proteins, but the magnitudes of strain applicable are limited (*22*). The design presented in this study overcomes these limitations by (1) prescribing strain anisotropy through eccentricity of the culture well geometry, and (2) providing uniform and stable construct attachment via compression springs. We were able to apply homogeneous large deformation strain profiles (>30%) at high frequencies (3 Hz) to engineered 3-D tissues for at least 96 h, significantly broadening the scope of 3-D in vitro mechanobiological inquiry available.

Anisotropic mechanoregulation of VIC phenotype

Fibroblasts transition between quiescent and activated myofibroblasts, which is controlled in part by the local mechanical environment. In the case of aortic valves, interstitial cells are largely quiescent fibroblasts in healthy tissue, but can become activated myofibroblasts and even osteoblasts in disease states (*39*), (*40*) and (*41*). Taylor et al. defines the quiescent valve fibroblast phenotype as one that maintains ECM composition and collagen maturity (*42*). When VICs become activated myofibroblasts, they significantly upregulate contractile filaments including ACTA2, exhibit increased traction forces and migratory behavior, and secrete matrix proteins as well as their proteases and inhibitors. These factors all lead to dramatic changes in matrix composition and structural organization (*39*) and (*42*). Grinnell et al. and colleagues have used free floating (stress-free) and anchored (stressed) collagen

hydrogels to show that matrix tension induces a myofibroblastic differentiation of fibroblasts from a variety of sources (*6*), (*43*) and (*44*). We previously found that VICs cultured in 2-D flasks expressed nearly double the amount of ACTA2 when compared to seeded within floating3-D collagen gels, supporting this concept (*45*). Similarly, we here find that mechanically anchored VICs in 3-D culture expressed ACTA2 nearly three times higher than unstressed controls (**Fig. S7.4**). Taken together, these results suggest that VICs in anchored 3-D collagen gels provide a simple positive-control model of myofibroblast-like differentiation.

Fibroblast–myofibroblast transitions of VICs in the context of cyclic stretch, however, are more complex. Merryman et al. showed that cyclic uniaxial stretch of porcine aortic valve leaflets for 7–14 d produced a slight increase in ACTA2 gene expression, but a marked increase with exogenous TGFβ1 administration (*46*). Thayer et al. found that increased ACTA2 expression due to cyclic stretch could be relieved with combined loading with cyclic pressure (*47*). Our findings here, using VICs in 3-D hydrogel culture, show that ACTA2 expression is also independently regulated by the anisotropy of applied cyclic strain. Cyclic equiaxial strain decreases ACTA2 expression, suggesting fibroblast-like tendencies, but strong directional biaxial strain re-elevates ACTA2 toward the stressed myofibroblastic control condition. We further found that ACTA2 expression was directly related to the degree of cell alignment, which occurred perpendicular to the first principal axis of stretch. Vimentin, commonly employed as a marker for fibroblasts, is an intermediate filament expressed by mesenchymal cells and responsible for cytoskeletal integrity, but not expressed

exclusively by fibroblasts (*48*). We found vimentin expression changed similarly with ACTA2 under cyclic stretch, but there was no change between anchored and free-floating 3-D gels, nor we did not notice a directionally dependent expression tendency like we did with ACTA2. Therefore, we are confident that vimentin was a reasonable choice as a fibroblast marker for this system, and focus our interpretations on ACTA2 and other behaviors.

Our results here demonstrate that the complete picture of fibroblast "quiescence" and "activation" should also include cell phenotype and turnover characteristics. Schnieder and Deck et al. used autoradiographic labeling in rats to demonstrate that normal cell and matrix turnovers in a variety of fibroblast-populated tissues are not identical. In fact, valve leaflets exhibited naturally elevated proliferation, matrix synthesis, and degradation rates indicative of a continuous but homeostatic remodeling environment (*7*). Considering that the native healthy valve contains relatively few myofibroblasts, this suggests that phenotype "quiescence" may still present dynamic matrix remodeling behavior. Our studies here suggest that one factor that can potentiate this is mechanical forces, specifically anisotropic cyclic stretch. Cyclic biaxial strain induced both VIC proliferation and apoptosis, suggesting a high degree of turnover, while equiaxial strain exhibited significantly less. Furthermore, equiaxial strain had very little effect on matrix fiber reorganization, while cyclic anisotropic strain resulted in significantly aligned matrix fibers. Following this trend, equibiaxial stretch reduced ACTA2 expression, while anisotropic strain elevates it. Taken together, these results suggest that cyclic equiaxial strain

promotes a tendency towards a quiescent fibroblastic phenotype, and increasing strain anisotropy supports a tendency towards an active myofibroblastic differentiation. We note that all these studies were performed at the same overall magnitude of area strain and frequency. While not the focus of this study, we believe that these responses are likely further altered by strain magnitude and frequency (*49*). It appears that matrix remodeling lags changes in cell response to anisotropic strain, but the underlying cause is not yet known. Without live cells, however, no matrix fiber alignment occurs in any strain pattern (data not shown), suggesting that this remodeling is an active cell-mediated response to the applied strain field. Future studies considering altered matrix synthesis, degradation, or matrix fibril diameter, may help reveal the time-dependent remodeling tendencies and clarify the extent of differentiation.

Accelerated tissue engineering via strain anisotropy

Modern tissue engineering approaches for load-bearing tissues have sought to mimic or restore the native biological and biomechanical characteristics of replaced tissue, among them biomimetic material anisotropy (*50*). Fiber-reinforced scaffolds, whether electrospun, nonwoven, or woven mesh designs with biodegradable materials have been employed to create directionally dependent material behaviors (*51*). Alternatively, biological polymers such as collagen and fibrin can be mechanically stimulated to evolve material heterogeneity (*52*) and (*53*). Whether this anisotropy needs to be included at the outset or evolved over time is still debated. Many bioreactors designed for whole tissues expose local regions to anisotropic strain fields, but these are difficult to quantify and challenging to relate directly to local cell

differentiation and matrix remodeling (*54*). Alternatively, anisotropic mechanical conditioning of 3-D engineered tissue sheets could accelerate the formation of desired structural architecture and tissue biomechanics prior to forming more complex tissue shapes (*55*). Furthermore, our results suggest it may be possible to direct stem/progenitor cells towards multiple distinct phenotypes through strain anisotropy, which has a potential advantage in that these cells will also be self-organized in their environmental context. It is not yet known how cells in defined 3-D matrix architectures interpret both time and directionally varying anisotropic strain fields, but our findings suggest that each component may contribute to accelerated matrix remodeling and cell differentiation.

CONCLUSIONS

We developed and implemented a novel bioreactor to investigate the relationship between anisotropic strain, cell differentiation, and matrix remodeling in 3-D culture. Our findings demonstrate that applied cyclic biaxial strain anisotropy induces time-dependent VIC orientation and collagen fiber alignment, which occurs at 48 h and 96 h, respectively. During this process, ACTA2 expression was directly related to the degree of cell alignment and occurred perpendicular to the principal axes of loading. These findings suggest that biaxial strain anisotropy, independent of magnitude or frequency, is a potent regulator of rapid matrix reorganization and VIC phenotype. Controlling strain anisotropy in vivo or in vitro may be a potent means of directing adaptive tissue remodeling.

.

SUPPLEMENTARY DATA

SUPPLEMENTAL METHODS

Cell Isolation

Adult PAVIC were isolated by a collagenase digestion method as previously described. Briefly, aortic valve leaflets were obtained from a local abattoir and placed on cold Dulbecco's phosphate buffered saline (Invitrogen) for transport. The surface of the leaflets was partially digested in (600U/ml, Worthington) collagenase solution with Dulbecco's Modified Eagle's Medium (DMEM) (Gibco) for 5-10 minutes after which the endothelial layer was sheared off with a cotton swab. The remaining leaflet was then incubated for 12-18 hours in collagenase solution and homogenized with a serological pipette. Cells were then plated on tissue culture plastic, and maintained with DMEM (Gibco) supplemented with 10% fetal bovine serum (Gibco) and 1% penicillin/streptomycin (Gibco). Cultures were fed every two days and split at confluency. Cultures used for experiments were between passages 4 and 6.

Strain Calibration Equations

These patterns related the undeformed (unstrained) configuration and the deformed (strained) configuration by position , namely:

$$x_i = FX_i + B_i \qquad \text{Equation (1)}$$

where x is the deformed coordinates, and X is the undeformed coordinates. F is a deformation gradient tensor for the plane of interest, either membrane or construct surface:

$$F_{ij} = \frac{dx_i}{dx_j} \qquad \text{Equation (2)}$$

By solving the system of equations in Eq. (1) relating the observed deformed and undeformed configurations of triangular bead/mark positions, the coefficients of F were obtained. These were then was used to obtain finite (Green's) strain components:

$$E = 0.5(F^T F - I) \qquad \text{Equation (3)}$$

where I is the identity tensor. Finite strain was then transformed into area strain by the following formula:

$$\frac{A}{A_0} = \lambda_1 \lambda_2 = (2E_{11} + 1)^{0.5}(2E_{22} + 1)^{0.5} \qquad \text{Equation (4)}$$

Anisotropic Strain of 3D Tissue Constructs

The device used to impose anisotropic strain is a modified version of the system described in detail by Butcher et al. The system consists of four aluminium cassettes which are placed on a movable stage, and clamped concentrically over a rigid aluminium cylindrical mandrel lined with Teflon. A stepper motor (34Y,

Anaheim Automation) was used to drive the movable stage down over the rigid mandrel deforming the silicon membrane at a specific magnitude and frequency. Limit switches were mounted on either side of the movable stage so that any unwanted movement would be controlled. These modifications only require one calibration of the wells and re-zeroing is recognized by the limit switches. A cooling system was also implemented to control the temperature from the stepper motor to the surrounding metal. A cold plate (CP12, Lytron) was mounted below the stepper motor connected to a stand up freezer contained cold water. The cold water from the freezer was pumped to the cold plate and returned the heated water from the stepper motor. The magnitude and frequency of the stepper motor was controlled through a controller (DPN10601, Anaheim Automation) and various waveforms could be applied depending on the duration of current applied.

Construction of Cassettes

To create the silicon membranes used for straining the hydrogels, a negative mold within 3/8" piece of polycarbonate was constructed **(Fig. 1B)**. The polycarbonate was machined to form wells at a depth of 3mm, at various biaxial eccentricities. In terms of major to minor axis (x vs. y), ellipsoidal wells were generated at 1:1, 2:1, and 4:1 geometries. A bevel was also machined within the ellipse for securing the compression springs. Polydimethylsiloxane (Sylgard 184, Dow Corning, Midland, MI) was combined at a concentration of 20:1 respectively, and degassed prior to use. The silicon was poured into the negative molds and let solidify at 70°C for 12 hours. The silicon molds were then released from the

polycarbonate, mounted within the cassettes, and autoclaved. The sterilized compression springs were then placed in the wells and covered with a petri dish lid (150mm).

FEA Analysis

Throughout the design of the bioreactor, a finite element model was used to optimize shapes and ensure homogeneous anisotropic strain patterns. Various well diameters, aspect ratios, silicon membrane depths, cassette sizes, magnitudes of strain, and frequency were all considered. The silicon membranes were modeled as a hyperelastic material using a Mooney-Rivlin two-parameter model with invariant coefficients of 0.55 and 0.14 MPa. The membranes were first generated within the plane function as 2D triangular elements. The geometry of membrane measured 25mm in radius and the platen was 20mm in radius with a filet radius of 1mm. Contact analysis using a sliding boundary condition was used for the intersection between the membrane and platen, assuming a coefficient of friction of 0.06 (Castrol, Braycote 803). For all simulations, the displacement was applied to the edge of the membrane. All finite element simulations were completed through ANSYS.

Hydrogel Seeding

Three-dimensional (3D) hydrogel constructs were created using a modified procedure from that previously described. Porcine aortic valve interstitial cells (PAVIC) were used as a representative planar tissue fibroblast source. A suspension of 400,000 cells/ml porcine aortic valvular interstitial cells (PAVIC) were used in 3x

DMEM with 10% FBS (Gibco), 2 mg/ml type I collagen (BD), and 0.1 M NaOH to neutralize the solution. 3D cultures with 1:1, 2:1, and 4:1 aspect ratio were pre-loaded 300 steps below center of platen. This was done to shift the calibration curve to the linear portion of the graph and increase the size of the well. Once pre-loaded, wells were filled with different volumes of gels depending on the geometry (ratio of major to minor axis). For the 1:1, 2:1, 4:1, and control wells, 100µl, 125µl, 150µl, and 125µl respectively of gel was inoculated into the wells containing the compression springs, which solidified after 60 minutes. After 60 min, 18 ml of media was added to the reservoir. The hydrogels were allowed to compact around the springs over a 24 hr period after which a 20% area strain (250 step size, 2mm) was applied to all the constructs at 1Hz. This seeded compaction process is similar to Garvin et al. such that fibroblasts suspended in collagen gels will compact around an anchor and form a stable construct . Static cultures served as controls and both mechanically anchored and unanchored hydrogels were used. The unanchored controls were lifted from the well after 24 hr to allow free compaction of the gels. All materials were sterilized via autoclaving before use. The system was housed in a standard tissue culture incubator, maintained at 37°C and 5% CO_2 throughout the culture period.

Second Harmonic Generation

Galvanometric mirrors were use to scan laser pulses in a raster pattern. The laser scanning and data acquisition were controlled by MPSCOPE software . SHG signal was detected using a bandpass filter centered at 517 nm with 65-nm bandwidth.

Images were acquired using a 0.95-numerical aperture, 20x water immersion objective (Carl Zeiss Inc., Thornwood, NY) at 10 μm section spacing.

RT-PCR

To determine gene expression changes, the hydrogel construct was isolated from the center of each well. Using a Qiagen total RNA purification kit (Qiagen, Valencia, CA), RNA was reverse transcribed to cDNA using the SuperScript III RT-PCR kit with oligo(dT) primer (Invitrogen). Sufficient quality RNA was determined by an absorbance ratio A_{260}/A_{280} of 1.8 – 2.1, while the quantity of RNA was determined by measuring the absorbance at 260nm (A_{260}). Primers were designed to detect 18S, alpha-smooth muscle actin, and vimentin in cDNA clones: 18S (R–AATGGGGTTCAACGGGTTAC, F-TAGAGGGACAAGTGGCGTTC, Amplicon 92bp, Accession DQ437859.1), VIM (F–GTACCGGAGACAGGTGCAGT, R–TTCCACGGCAAAGTTCTCTT, Amplicon 69bp, Accession XM_00213072.1), ACTA2 (F–CAGCCAGGATGTGTGAAGAA, R-TCACCCCCTGATGTCTAGGA, Amplicon 104bp, Accession NM_001164650.1). Real time PCR was performed on all samples using SYBR Green PCR master mix (Applied Biosystems, Carlsbad, CA) and a MiniOpticon Real-Time PCR Detection System (Biorad, Hercules, CA). Amplification cycle thresholds were normalized to those from 18S and melt curves compared across samples. Stable expression of 18S was observed across all mechanically stimulated conditions and GAPDH was used as a secondary housekeeping gene to verify expression level.

Collagen Gel Immunofluorescence

Fixed samples on collagen gels were washed for 15 minutes on a rocker 3 times with PBS, permeabilized with 0.2% Triton-X 100 (VWR International, Radnor, PA) for 10 minutes, and washed another 3 times with PBS. For the phenotype studies, samples were incubated overnight at 4^{o}C in a 1% BSA (Rockland Immunochemicals, Inc., Gilbertsville, PA) blocking solution followed by another 4^{o}C overnight incubation with mouse anti-human vimentin (VIM) 1:100 (Invitrogen) and rabbit anti-human α-SMA 1:100 (Spring Bioscience). For the orientation studies, samples were incubated with phalloidin (Invitrogen). After 3 washes for 15 minutes with PBS, samples were exposed to Alexa Fluor® 488 or 568 conjugated (Invitrogen), species specific secondary antibodies at 1:100 in 1% BSA for 2 hours at room temperature. Three more washes with PBS for 15 minutes were followed by incubation with either DRAQ5 far red nuclear stain (Enzo Life Sciences, Plymouth Meeting, PA) at 1:1000 or Hoechst (Invitrogen) at 1:10000. Samples were washed once more with 18Mohm water and stored in 18mohm water at 4^{0}C. Images were taken with a Leica TCS SP2 laser scanning spectral confocal microscope (Leica-Microsystems, Bannockburn, IL). ACTA2 and VIM was measured by creating a region of interest across the entire image. Total intensity of F-actin (green) and VIM (blue) was quantified. These values were then normalized by total nuclei within the image. All image and processing settings were consistent throughout.

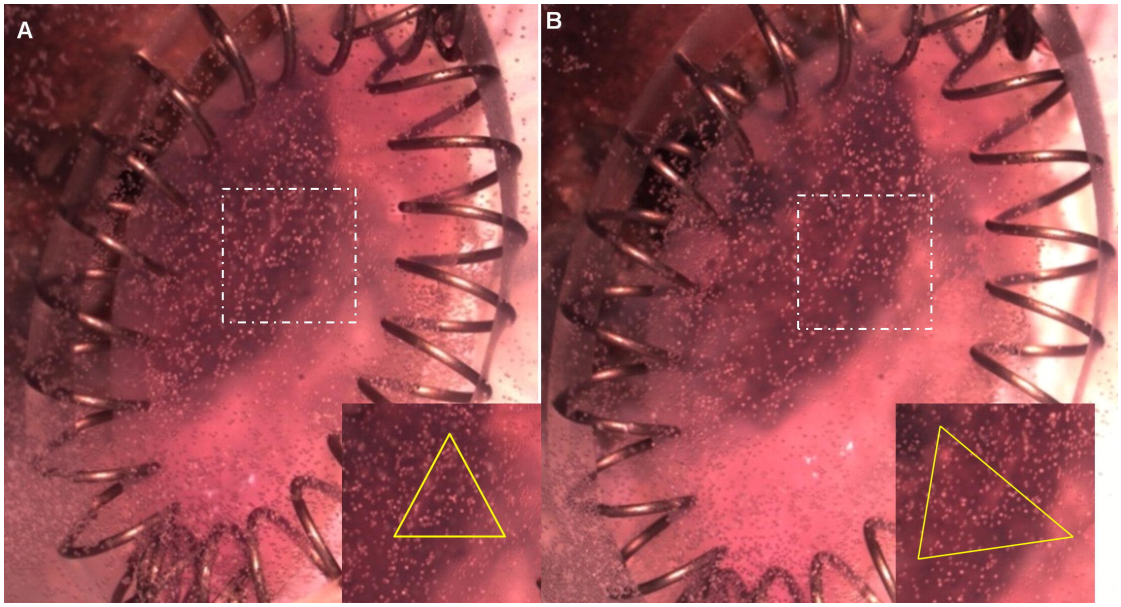

Supplement Figure 7.1 – Calibration of anisotropic strain fields.
(A) 40 μm glass beads were placed within the collagen hydrogel and tracked from the undeformed to the (B) deformed configuration. Virtual triangles created with bead centroids as vertexes were used to quantitatively monitor tissue deformation and to assess the uniformity of the strain field (inset).

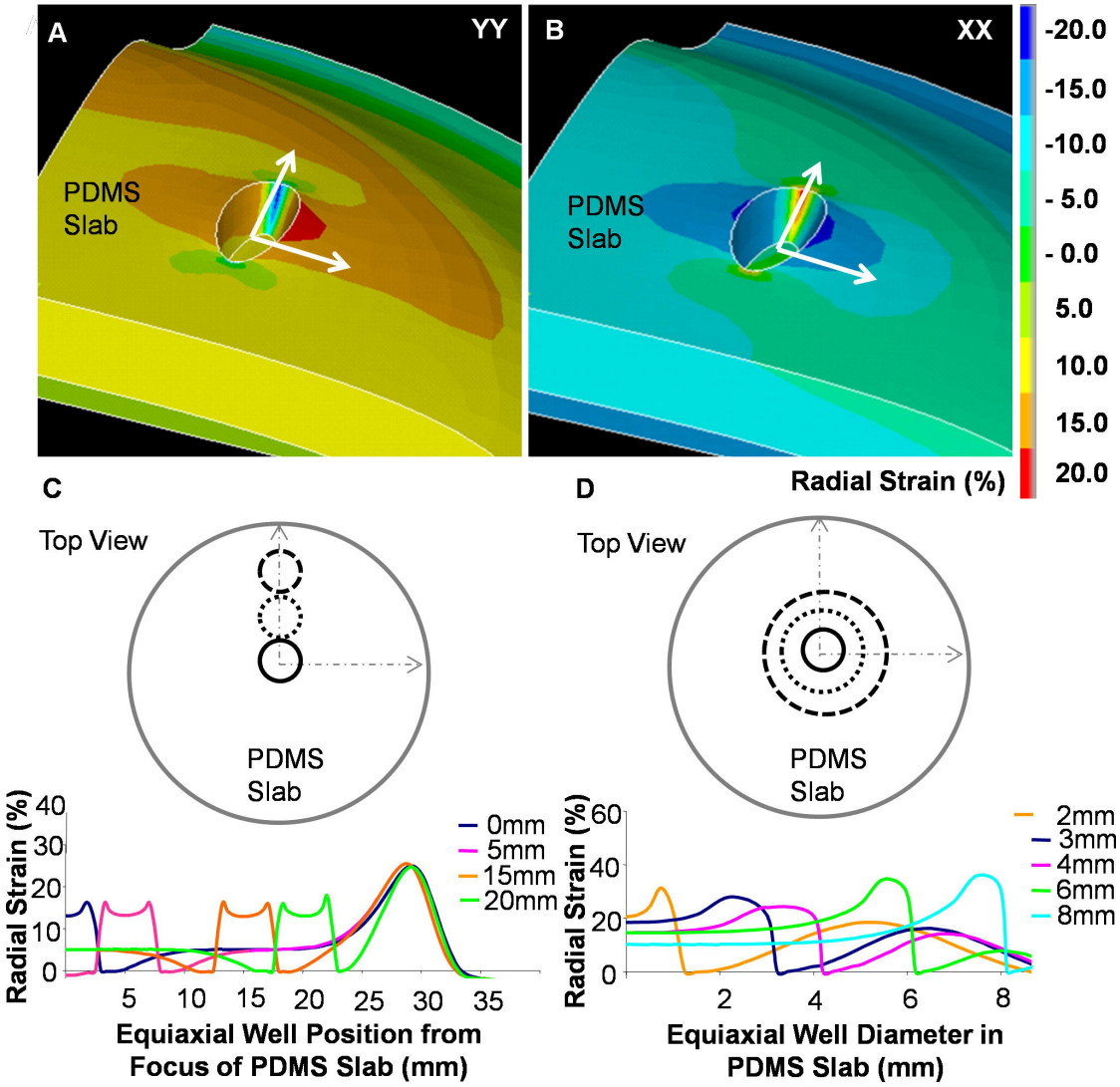

Supplement Figure 7.2 – FEA simulations for predicted strain fields and geometry variations.
(A-B) Representative 3D strain field simulations (isotropic view) for elliptical well configurations, plotted against both the E_{XX} and E_{YY} direction of radial force (red denotes high levels of strain where regions of blue indicate low levels). (B) Varying equiaxial well position within the PDMS slab does not alter magnitudes and distribution of strain field such that a 20% radial strain is maintained through a 25mm deviation from the PDMS slab focus. (C) Changes in equiaxial well size leads to a significant reduction in achievable strain magnitudes such that a reduction of 20% to 10% radial strain occurred when increasing well diameter from 2mm to 8mm.

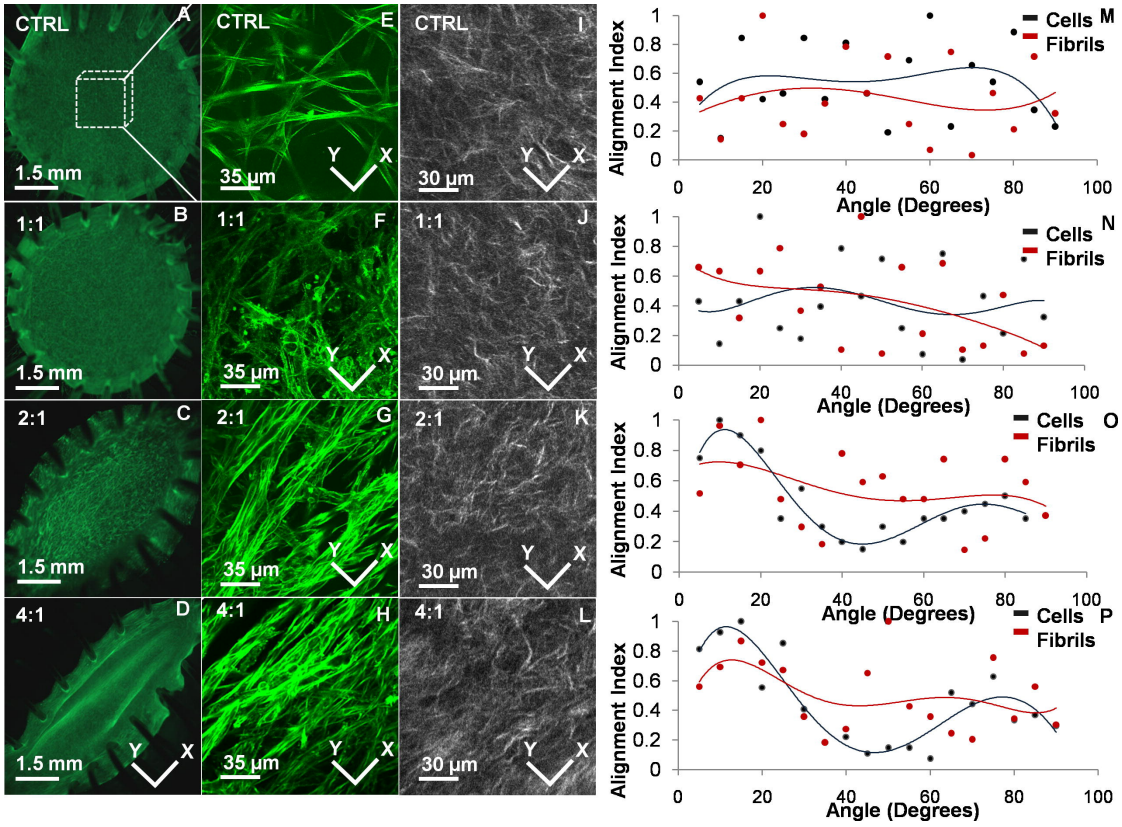

Supplement Figure 7.3 – Cell and matrix fibers rapidly reorient orthogonally with cyclic strain anisotropy at 48 hours.
(A-D) Macroscopic view of collagen gels compacted within elliptical compression springs. (E-H) Orientation of AVIC associated with the anisotropic strain profiles (f-actin-green). (I-L) Orientation of collagen fibrils associated with anisotropic strain profiles (SHG imaging). (M-P) Representative alignment curves indicate orientation of VIC and coincide with respect to the principal directions of strain while minimal collagen fibril alignment has occurred.

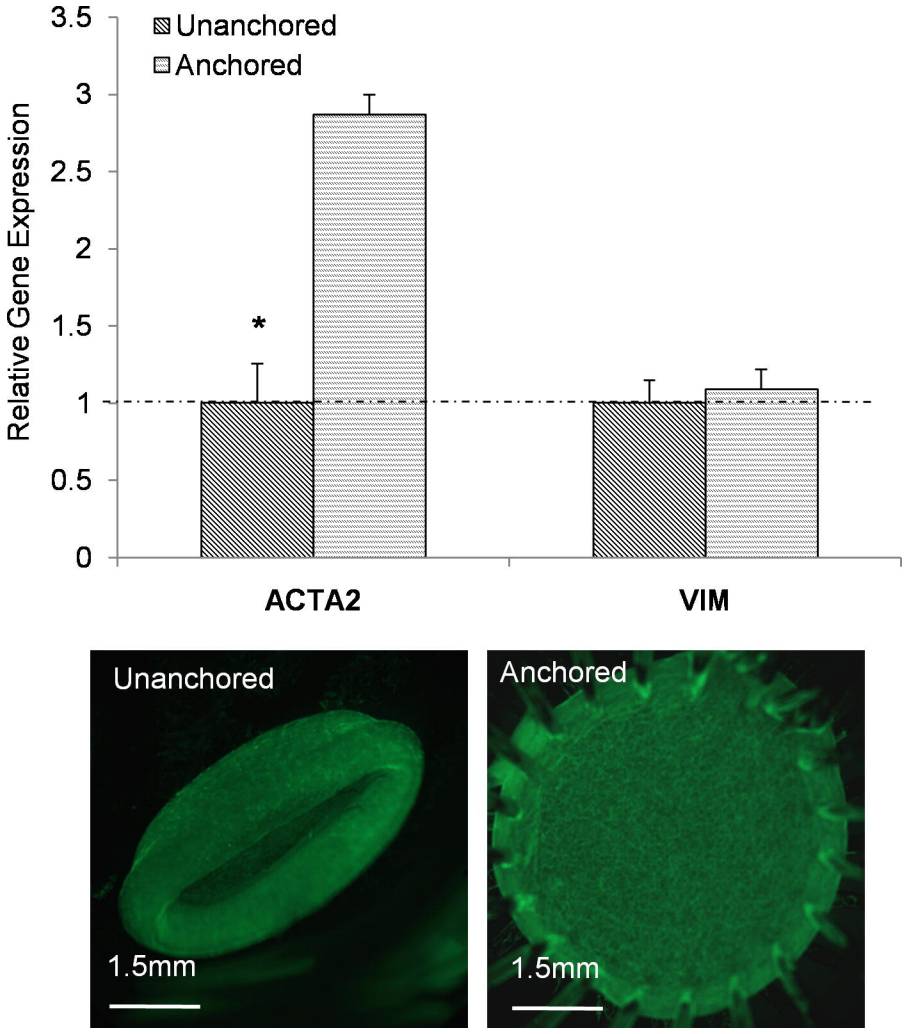

Supplement Figure 7.4 - Mechanically anchored and unanchored hydrogels regulate ACTA2 expression levels at 48 hours.
Mechanically anchored hydrogels elevate ACTA2 and expression levels (2.87 fold ± 0.13) compared to unanchored hydrogels, while VIM expression is unchanged. Gene expression was measured via real-time PCR and normalized to 18S. Error bars show ±SD, $n \geq 6$. Asterisks signify statistical differences according to a Student's t-test ($p \leq 0.05$).

REFERENCES

1. M. S. Sacks, W. Sun, Multiaxial mechanical behavior of biological materials. *Annu Rev Biomed Eng* **5**, 251 (Jan 1, 2003).
2. M. S. Sacks, F. J. Schoen, J. E. Mayer, Bioengineering challenges for heart valve tissue engineering. *Annu Rev Biomed Eng* **11**, 289 (Jan 1, 2009).
3. R. Sodian *et al.*, Early in vivo experience with tissue-engineered trileaflet heart valves. *Circulation* **102**, III22 (Nov 7, 2000).
4. E. Rabkin-Aikawa *et al.*, Clinical pulmonary autograft valves: pathologic evidence of adaptive remodeling in the aortic site. *J Thorac Cardiovasc Surg* **128**, 552 (Oct 1, 2004).
5. G. Gabbiani, The myofibroblast in wound healing and fibrocontractive diseases. *J Pathol* **200**, 500 (Jul 1, 2003).
6. F. Grinnell, Fibroblasts, myofibroblasts, and wound contraction. *J Cell Biol* **124**, 401 (Feb 1, 1994).
7. P. J. Schneider, J. D. Deck, Tissue and cell renewal in the natural aortic valve of rats: an autoradiographic study. *Cardiovasc Res* **15**, 181 (Apr 1, 1981).
8. J. T. Butcher, G. J. Mahler, L. A. Hockaday, Aortic valve disease and treatment: the need for naturally engineered solutions. *Adv Drug Deliv Rev* **63**, 242 (Apr 30, 2011).
9. E. Bell, B. Ivarsson, C. Merrill, Production of a tissue-like structure by contraction of collagen lattices by human fibroblasts of different proliferative potential in vitro. *Proc Natl Acad Sci USA* **76**, 1274 (Mar 1, 1979).

10. F. Grinnell, C.-H. Ho, Transforming growth factor beta stimulates fibroblast-collagen matrix contraction by different mechanisms in mechanically loaded and unloaded matrices. *Exp Cell Res* **273**, 248 (Feb 15, 2002).

11. T. D. Brown, Techniques for mechanical stimulation of cells in vitro: a review. *J Biomech* **33**, 3 (Jan 1, 2000).

12. P. G. Smith, L. Deng, J. J. Fredberg, G. N. Maksym, Mechanical strain increases cell stiffness through cytoskeletal filament reorganization. *Am J Physiol Lung Cell Mol Physiol* **285**, L456 (Aug 1, 2003).

13. J. Y. Shyy, S. Chien, Role of integrins in cellular responses to mechanical stress and adhesion. *Curr Opin Cell Biol* **9**, 707 (Oct 1, 1997).

14. J. H.-C. Wang, B. P. Thampatty, J.-S. Lin, H.-J. Im, Mechanoregulation of gene expression in fibroblasts. *Gene* **391**, 1 (Apr 15, 2007).

15. A. A. Lee, T. Delhaas, A. D. McCulloch, F. J. Villarreal, Differential responses of adult cardiac fibroblasts to in vitro biaxial strain patterns. *J Mol Cell Cardiol* **31**, 1833 (Oct 1, 1999).

16. E. J. Culbertson, L. Xing, Y. Wen, M. G. Franz, Loss of mechanical strain impairs abdominal wall fibroblast proliferation, orientation, and collagen contraction function. *Surgery* **150**, 410 (Sep 1, 2011).

17. R. W. Ogden, Nonlinear elasticity, anisotropy, material stability, and residual stresses in soft tissue. *CISM Courses and Lectures* **441**, 65 (Jul 26, 2003).

18. M. T. Zaucha *et al.*, A novel cylindrical biaxial computer-controlled bioreactor and biomechanical testing device for vascular tissue engineering. *Tissue Eng Part A* **15**, 3331 (Nov 1, 2009).

19. T. A. Hornberger, D. D. Armstrong, T. J. Koh, T. J. Burkholder, K. A. Esser, Intracellular signaling specificity in response to uniaxial vs. multiaxial stretch: implications for mechanotransduction. *Am J Physiol, Cell Physiol* **288**, C185 (Jan 1, 2005).

20. C.-H. Ku *et al.*, Collagen synthesis by mesenchymal stem cells and aortic valve interstitial cells in response to mechanical stretch. *Cardiovasc Res* **71**, 548 (Aug 1, 2006).

21. W. Tan, D. Scott, D. Belchenko, H. J. Qi, L. Xiao, Development and evaluation of microdevices for studying anisotropic biaxial cyclic stretch on cells. *Biomed Microdevices* **10**, 869 (Dec 1, 2008).

22. J. T. Butcher, B. C. Barrett, R. M. Nerem, Equibiaxial strain stimulates fibroblastic phenotype shift in smooth muscle cells in an engineered tissue model of the aortic wall. *Biomaterials* **27**, 5252 (Oct 1, 2006).

23. V. Gupta, K. J. Grande-Allen, Effects of static and cyclic loading in regulating extracellular matrix synthesis by cardiovascular cells. *Cardiovasc Res* **72**, 375 (Dec 1, 2006).

24. G. Mahler, R. Gould, J. Butcher, Isolation and culture of avian embryonic valvular progenitor cells. *J Vis Exp*, (Jan 1, 2010).

25. R. A. Gould, J. T. Butcher, Isolation of valvular endothelial cells. *J Vis Exp*, (Jan 1, 2010).

26. J. Garvin, J. Qi, M. Maloney, A. J. Banes, Novel system for engineering bioartificial tendons and application of mechanical load. *Tissue Eng* **9**, 967 (Oct 1, 2003).

27. D. Seliktar, R. M. Nerem, Z. S. Galis, The role of matrix metalloproteinase-2 in the remodeling of cell-seeded vascular constructs subjected to cyclic strain. *Ann Biomed Eng* **29**, 923 (Nov 1, 2001).

28. J. T. Butcher, A. M. Penrod, A. J. García, R. M. Nerem, Unique morphology and focal adhesion development of valvular endothelial cells in static and fluid flow environments. *Arterioscler Thromb Vasc Biol* **24**, 1429 (Aug 1, 2004).

29. W. R. Zipfel, R. M. Williams, W. W. Webb, Nonlinear magic: multiphoton microscopy in the biosciences. *Nat Biotechnol* **21**, 1369 (Nov 1, 2003).

30. R. D. Bowles, R. M. Williams, W. R. Zipfel, L. J. Bonassar, Self-assembly of aligned tissue-engineered annulus fibrosus and intervertebral disc composite via collagen gel contraction. *Tissue Eng Part A* **16**, 1339 (Apr 1, 2010).

31. T. T. Tower, M. R. Neidert, R. T. Tranquillo, Fiber alignment imaging during mechanical testing of soft tissues. *Ann Biomed Eng* **30**, 1221 (Jan 1, 2002).

32. M. S. Sacks, D. B. Smith, E. D. Hiester, A small angle light scattering device for planar connective tissue microstructural analysis. *Ann Biomed Eng* **25**, 678 (Jan 1, 1997).

33. C. H. Yap *et al.*, Dynamic deformation characteristics of porcine aortic valve leaflet under normal and hypertensive conditions. *Am J Physiol Heart Circ Physiol* **298**, H395 (Feb 1, 2010).

34. M. S. Sacks, W. David Merryman, D. E. Schmidt, On the biomechanics of heart valve function. *J Biomech* **42**, 1804 (Aug 25, 2009).

35. E. J. Weinberg, M. R. Kaazempur Mofrad, A multiscale computational comparison of the bicuspid and tricuspid aortic valves in relation to calcific aortic stenosis. *J Biomech* **41**, 3482 (Dec 5, 2008).

36. F. Robicsek, M. J. Thubrikar, J. W. Cook, B. Fowler, The congenitally bicuspid aortic valve: how does it function? Why does it fail? *Ann Thorac Surg* **77**, 177 (Jan 1, 2004).

37. A. J. Banes, G. W. Link, J. W. Gilbert, R. Tran Son Tay, O. Monbureau, Culturing cells in a mechanically active environment. *Am Biotechnol Lab* **8**, 12 (May 1, 1990).

38. V. Gupta, J. A. Werdenberg, T. L. Blevins, K. J. Grande-Allen, Synthesis of glycosaminoglycans in differently loaded regions of collagen gels seeded with valvular interstitial cells. *Tissue Eng* **13**, 41 (Jan 1, 2007).

39. E. Rabkin-Aikawa, M. Farber, M. Aikawa, F. J. Schoen, Dynamic and reversible changes of interstitial cell phenotype during remodeling of cardiac valves. *J Heart Valve Dis* **13**, 841 (Sep 1, 2004).

40. J.-H. Chen, C. Y. Y. Yip, E. D. Sone, C. A. Simmons, Identification and characterization of aortic valve mesenchymal progenitor cells with robust osteogenic calcification potential. *Am J Pathol* **174**, 1109 (Mar 1, 2009).

41. A. C. Liu, V. R. Joag, A. I. Gotlieb, The emerging role of valve interstitial cell phenotypes in regulating heart valve pathobiology. *Am J Pathol* **171**, 1407 (Nov 1, 2007).

42. P. M. Taylor, P. Batten, N. J. Brand, P. S. Thomas, M. H. Yacoub, The cardiac valve interstitial cell. *Int J Biochem Cell Biol* **35**, 113 (Feb 1, 2003).

43. F. Grinnell, Fibroblast-collagen-matrix contraction: growth-factor signalling and mechanical loading. *Trends Cell Biol* **10**, 362 (Sep 1, 2000).

44. F. Grinnell, Fibroblast biology in three-dimensional collagen matrices. *Trends Cell Biol* **13**, 264 (May 1, 2003).

45. J. T. Butcher, R. M. Nerem, Porcine aortic valve interstitial cells in three-dimensional culture: comparison of phenotype with aortic smooth muscle cells. *J Heart Valve Dis* **13**, 478 (May 1, 2004).

46. W. D. Merryman *et al.*, Synergistic effects of cyclic tension and transforming growth factor-beta1 on the aortic valve myofibroblast. *Cardiovasc Pathol* **16**, 268 (Jan 1, 2007).

47. P. Thayer *et al.*, The effects of combined cyclic stretch and pressure on the aortic valve interstitial cell phenotype. *Ann Biomed Eng* **39**, 1654 (Jun 1, 2011).

48. R. D. Goldman, S. Khuon, Y. H. Chou, P. Opal, P. M. Steinert, The function of intermediate filaments in cell shape and cytoskeletal integrity. *J Cell Biol* **134**, 971 (Aug 1, 1996).

49. S. P. Arnoczky *et al.*, Activation of stress-activated protein kinases (SAPK) in tendon cells following cyclic strain: the effects of strain frequency, strain magnitude, and cytosolic calcium. *J Orthop Res* **20**, 947 (Sep 1, 2002).

50. K. Mendelson, F. J. Schoen, Heart valve tissue engineering: concepts, approaches, progress, and challenges. *Ann Biomed Eng* **34**, 1799 (Dec 1, 2006).

51. T. Courtney, M. S. Sacks, J. Stankus, J. Guan, W. R. Wagner, Design and analysis of tissue engineering scaffolds that mimic soft tissue mechanical anisotropy. *Biomaterials* **27**, 3631 (Jul 1, 2006).

52. A. Mol *et al.*, Fibrin as a cell carrier in cardiovascular tissue engineering applications. *Biomaterials* **26**, 3113 (Jun 1, 2005).

53. M. R. Neidert, R. T. Tranquillo, Tissue-engineered valves with commissural alignment. *Tissue Eng* **12**, 891 (Apr 1, 2006).

54. I. Vesely, Heart valve tissue engineering. *Circ Res* **97**, 743 (Oct 14, 2005).

55. N. L'Heureux, S. Pâquet, R. Labbé, L. Germain, F. A. Auger, A completely biological tissue-engineered human blood vessel. *FASEB J* **12**, 47 (Jan 1, 1998).

CHAPTER 8

CONCLUSIONS AND FUTURE DIRECTIONS

CONCLUSIONS AND FUTURE DIRECTIONS

In vivo cerebral microcirculation of hematological disease states has not been previously investigated in detail due to a lack of suitable animal models and advanced imaging techniques for this research. The work in this dissertation pioneers precise, quantitative methods to study how alterations in blood rheology can impact cortical microvascular flow by taking advantage of non-linear optical microscopy techniques. In this final chapter, we will review the major conclusions as well as present future directions of our studies.

The first step in our studies dealt with enhancing the temporal resolution and efficiency of an automated algorithm to resolve blood flow speed from images acquired with two-photon excited fluorescence microscopy. We developed the algorithm to achieve fine hemodynamics details and were able to elucidate the dependency of cortical blood flow in single vessels, including capillaries and venules, on cardiac rhythms. We also discovered decreased blood flow speed just prior to each inhalation—a finding that some previous studies were in agreement with, but not others. The measurements of cerebral hemodynamics were the first with such sensitivity reported thus far and will enable further in-depth, high quality studies of cortical circulation, a process that is critical to maintaining neuronal health and function.

Next, we applied our technique to investigate the brains of myeloproliferative neoplasm mouse models. Cortical capillaries were chronically occluded in

polycythemic and essential thrombocythemic subjects due to the elevation of red blood cells, leukocytes, and platelets. Subjects with only red blood cell elevation also display marked stalled capillaries although not as severe as those with polycythemia. Activated leukocytes and platelets were found to obstruct cerebral blood flow by adhering to endothelium, which is injured and stimulated in a hyperviscosity flow regime. For blood vessels still showing flow, there is a general trend of slower blood flow. We investigated the effects of aspirin, a drug commonly used in essential thrombocythemia and polycythemia vera patients; and found minimal impacts that aid in reducing the disturbance of microvascular flow. Our study unearthed thrombosis in the microvascular network of myeloproliferative neoplasm brains, as well as identified leukocytes and platelets as the mechanism by which microvessels were plugged. These findings suggest that impediments to normal microcirculation can lead to cognitive degeneration in myeloproliferative neoplasms, and furthermore they point to the need for careful neurological evaluation.

Finally, we made use of second harmonic generation using femtosecond laser pulses in order to visualize collagen tissue rearrangement. Collagen is known to rearrange according to mechanical forces in their environment (for example, heart tissue demonstrates this phenomenon), but current techniques have been limited to equibiaxial or uniaxial stretch. Our novel bioreactor system applied anisotropic strain in a three-dimensional hydrogel and found increased cellular orientation and collagen fiber alignment along the principal directions of the strain field. Increasing biaxial strain anisotropy also stimulated both cellular proliferation and apoptosis during the

rearrangement. When cyclic strain field was applied, vimentin and smooth muscle actin expression rose with strain anisotropy and alignment was correlated in the same direction. These findings are fundamental to the design considerations and use of tissue engineering tools and techniques for remodeling soft tissues such as the cardiac muscles.

This work has used novel techniques to elucidate the impacts on cerebral microcirculation of hematological conditions where cellular components of the blood are in excess. In future work, we are interested in sickled-cell disease where anemia and abnormal red blood cells physiology dominate rheology. This study will fulfill the span of blood cell concentrations—from insufficient to excessive—to gain a further understanding of the significant thrombotic complications that evolve as cell numbers diverge from a healthy state.